Quantification of active pharmaceutical ingredients and polymorphs in tablets by spectroscopic means

Michelle Celine Hennigan

Thesis presented for the degree of Ph.D.

to the National University of Ireland

Submitted November 2013

School of Chemistry

National University of Ireland Galway

Supervisor: Dr. Alan G. Ryder

Head of School: Prof. Paul V. Murphy

Abstract

Active pharmaceutical ingredients (APIs) can exist in various solid state forms including polymorphs, solvates, and hydrates. In the case of polymorphs each form can possess its own unique physical properties and chemical stability which in turn can directly affect the efficacy of the API. It is clear that accurate characterisation and quantification of the precise solid state form present within a formulation is of vital concern for safety and regulatory affairs. It is therefore important to study and compare which analytical technologies are most appropriate to address these issues. Powder X-ray diffraction (PXRD) is considered to be the golden standard in the differentiation of polymorphs as a difference in crystal structure signifies the presence of an alternate form. However this technique is not amenable to quick on–line analysis. Vibrational spectroscopies provide useful tools as they are rapid, non–destructive and non–contact where they can be employed in, on and at–line.

In this body of work the abilities of near infra-red (NIR) and Raman spectroscopies in combination with chemometric methods for the identification and quantification of low levels of API and polymorph contaminants present in model tablet formulations were investigated. For active quantification a simple model tablet system comprised of a model API, 5–methyl–2–[(2–nitrophenyl)amino]–3– thiophenecarbonitrile, ROY, in a matrix of excipients was utilised. The tablets were then analysed using PXRD, NIR, backscattering Raman (BRS) and transmission Raman (TRS) spectroscopies. The data was pre-processed using a variety of methods. The data was then used to develop a range of calibration models for predicting ROY concentration with the best accuracy of ~0.3% RMSEP (root mean square error of prediction) being achieved with NIR and Transmission Raman spectroscopies.

Polymorph and polymorph contaminant within formulations studies were concerned with the polymorphs of piracetam. A simple binary polymorphic system consisting of mixtures of varying proportions of Form II and III of piracetam were prepared and analysed by PXRD, NIR and Raman. Univariate and multivariate analyses were performed on the PXRD data and although multivariate chemometric analysis provided better error values of prediction for the level of polymorphs within the

mixtures, it did not perform as well as the NIR based multivariate model which was found to demonstrate the best accuracy overall. BRS models were poor due to the inherent sub–sampling associated with this technique.

For the polymorph contaminant work, low levels of polymorphic contaminant of Form II piracetam were incorporated into tablets containing 10% API loading of Form III piracetam in the range of 0.1 to 10% of the total tablet. Transmission Raman and NIR were comparable with limits of detection ~ 0.6% FII in tablets. Transmission Raman spectroscopy overcomes the limitation of sub–sampling and fluorescence that is often associated with the conventional backscattering Raman and is a technology ripe for utilisation in a process analytical technology context within the pharmaceutical industry.

Acknowledgements

I would like to thank my supervisor Dr. Alan Ryder for his support, technical expertise and solid counsel throughout this work and beyond. I thank all members past and present of the Nanoscale Biophotonics Laboratory and members of the Solid State Pharmaceutical Cluster particularly Dr. Andrea Erxleben and Prof. Pat McArdle. I would like to thank Dr. Yun Hu and Dr. Denise Croker for their collaborative work in this thesis. Thanks also to Prof. Pavel Matousek, Matthew Bloomfield and Andrew Owens of Cobalt Light Systems Ltd. for their involvement with the TRS100 work. To the staff of the School of Chemistry, NUI Galway, thank you for all your help.

Thanks to my parents, Martin and Therese Hennigan, and my siblings Christina, Carolyn, Kevin, Angela and Siobhán for their love, support and encouragement through all my studies and for making life interesting. You never let me forget that there are more important things in life than studying; though you let me get on with everything that I ever wanted to do with plenty of good advice and understanding. Thanks to all my extended family and all the Gallaghers for their support over the years.

Galway has been a wonderful place to study and I have many great friends that have made this place all the better by being here. Bridget, Cheryl and Amandine you always make me laugh and we've had many good moments over the years, from taking care of me as a new member of the group to all our laughs over the latest going ons in our lives. Thanks for all the great times in the past and all those to come. Jolanta and Nicole we have had brilliant times and thanks for your friendship through the years – from all our road–trips to cluster meetings to our marathon life conversations thanks for everything. To my fellow 2008 postgraduate class thanks for all the fun and entertainment over our years here.

To my wider circle of friends in Galway thanks for going along with my crazy plans through the years including but not limited to Tag rugby, Kitchen Chemistry and my vision of Mayo football, thanks for all your help and hours of listening. To all my Swinford friends, thanks for your friendship and support all through the years. Thanks to my colleagues in MSD also for their support and encouragement during the write–up period.

Most of all I would like to thank Martin for all your love, support and patience with everything I do, including this piece of work. I could not have done this without you. Thanks for all your belief in me and for being brilliant.

List of Abbreviations

ANDA	Abbreviated new drug application
ANN	Artificial neural networks
API	Active pharmaceutical ingredient
ATR-IR	Attenuated total reflectance infra-red spectroscopy
BRS	Backscatter Raman spectroscopy
CSD	Cambridge structural database
DSC	Differential scanning calorimetry
DR	Diffuse reflectance
DRIFT	Diffuse reflectance infra-red fourier transform spectroscopy
ED-XRD	Electron dispersive X-ray diffraction
F	Denotes polymorph
FDA	Food and drug administration
GMP	Good manufacturing practice
HPLC	High performance liquid chromatography
ICH	International conference on harmonisation
IR	Infra-red spectroscopy
LOD	Limit of detection
LOQ	Limit of quantification
LV	Latent variable
MCC	Microcrystalline cellulose
MgSt	Magnesium stearate
MIR	Mid infra-red spectroscopy
MSC	Multiplicative scatter correction
MSD	Mean square of differences
NDA	New drug application
NIR	Near infra-red spectroscopy
PAT	Process analytical technology
PC	Principal component
PCA	Principal component analysis
PIT	Process induced transformation
PLS	Partial least squares regression

PXRD	Powder X-ray diffraction
QbD	Quality by design
R^2	Correlation coefficient
RMSE	Root mean square error
RMSEC	Root mean square error of calibration
RMSECV	Root mean square error of cross validation
RMSEP	Root mean square error of prediction
ROI	Region of interest
ROY	5-methyl-2-[(2-nitrophenyl) amino] 3-thiphenecarbonitrile
SEP	Standard error of prediction
SG	Savitzky–Golay derivative
S/N	Signal to noise ratio
SNV	Standard normal variate
SORS	Spatially offset Raman spectroscopy
ssNMR	Solid-state nuclear magnetic resonance spectroscopy
STD	Standard deviation
TRS	Transmission Raman spectroscopy
UV	Ultraviolet–visible spectroscopy

Contents

1 Introduction

1.1 Overview of Pharmaceutical Solids

Crystallisation is commonly used for the separation and purification of active pharmaceutical ingredients (APIs) in the pharmaceutical industry. High purity crystalline compounds can be produced by this method with well–defined particle characteristics and incorporated into solid dosage forms. Organic molecules can crystallise into various solid state forms including polymorphs, solvates and co–crystals (Fig. 1). Each form can possess its own unique physical and chemical properties which in turn can directly affect performance characteristics such as bioavailability and solubility of the API under physiological conditions.(1-3) Bioavailability is an important parameter for pharmaceuticals and is a measurement of the rate and extent of the active drug that reaches systematic circulation in the body.(4)

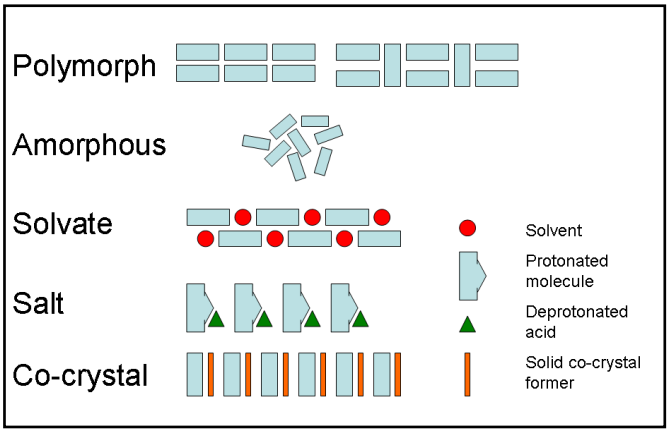

Figure 1 Schematic depicting different solid state forms.

There are no certain means of knowing whether or not a substance can exist in a number of solid state forms and if so, what is the form's propensity to convert to alternate forms. This is a significant risk to assess and indeed required by regulatory agencies as there are typically small energy differences between forms which can result in the unintentional formation of an undesired form – a famous case of which is Ritonavir which is discussed further in this chapter. To garner as much understanding of the API and potential alternate forms possible, rigorous solid state screening assays are typically carried out during the early stages of drug

development to identify alternate solid state forms. Presently it cannot be predicted what effect these new solid state forms could have on the API's solid state properties nor in–vivo dissolution profile and performance. Thus the importance of knowing which precise form of the API is present at all stages of product development, from initial studies through to manufacture of the final marketed product, is paramount to ensuring product performance and patient welfare. Extensive reviews on the subject of polymorphism and alternate solid state forms in pharmaceuticals have appeared in the literature in the past 15 years, signifying the high occurrence and importance of polymorphism in the field of pharmaceuticals.(3, 5-23)

1.2 Polymorphism

The most widely used definition of a polymorph is that of Walter McCrone; *"A polymorph is a solid crystalline phase of a given compound resulting from the possibility of at least two different arrangements of the molecules of that compound in the solid state."(24)* Polymorphs result from different spatial arrangements of the same molecule giving different crystal lattice structures. This can occur in two ways, by packing or conformational arrangements. Packing polymorphism results from different packing of conformationally rigid molecules by differing inter and intra molecular interactions. Conformational flexibility of a molecule can also allow the molecule to pack differently in the crystal lattice according to its molecular conformation creating further polymorphs.(25)

As polymorphs have unique crystal lattices, physical and chemical properties including density, melting point, solubility and stability can differ. All can have an effect on how the drug is processed, manufactured and its efficacy within the body. Such differences in properties can have significant consequences when polymorphism arises in pharmaceuticals, where the formation of a previously unknown, more thermodynamically stable polymorph with an undesired dissolution profile can cause the drug to be ineffective for its original purpose. This is exemplified by Abbotts' anti–retroviral drug Ritonavir.(26, 27) A more thermodynamically stable form with poorer solubility and bioavailability was discovered to be precipitating out in liquid filled capsules. This required

reformulation of the product to ensure that drug performance in vivo was not compromised. A recent study detailing the impact of polymorphism on solubility noted that in general the ratio of polymorph solubility of one form compared to another is typically less than two although occasionally a higher solubility ratios can be observed; for the case of Ritonavir the solubility ratio was four for the FII:FI polymorphs.(28)

1.3 Enantiotropy and monotropy

Polymorphs can be described in two ways from a thermodynamic viewpoint. Monotropic polymorphs are defined by free energy curve plots where one polymorph is the stable form at all temperatures below the melting point. For example in Fig. 2 left, FII is the most stable form. The free energy curves of the polymorphs do not come into contact with one another and no reversible polymorph transformation can occur at temperatures lower than the melting point.

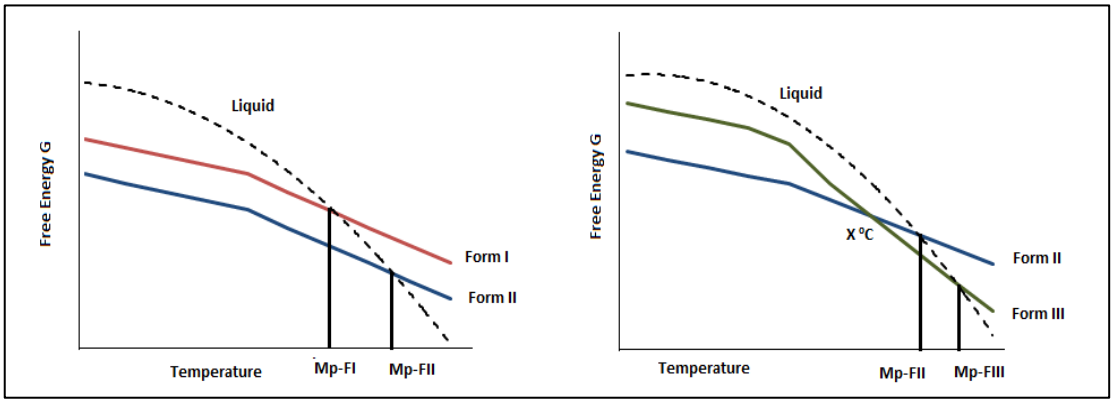

Figure 2 Free energy diagrams of monotropic and enantiotropic polymorphic systems.

In enantiotropic systems, the free energy curves of the polymorphs intersect at a defined transition temperature which occurs before the melting point of the solid. This transition is reversible meaning that conversion of one form to another can occur. In the example above, Fig. 2 right, FII and FIII share an enantiotropic relationship where at a given temperature X^{o}C they can interconvert from one form to another. At temperatures above X^{o}C FIII is the most stable polymorph and at temperatures below X^{o}C FII is the most stable form.

1.4 Ostwald's rule

Predominantly, the most thermodynamically stable polymorph is usually selected for development for inclusion in a pharmaceutical product; however where a metastable form is easier to manufacture, process or enhances bioavailability, it can be selected for development if it will not undergo undesired transformations to an alternate solid state form on processing or storage.(29) Ostwald's rule states that *"When leaving a given state and in transforming to another state, the state which is sought out is not the thermodynamically stable one, but the state nearest in stability to the original state"*.(30) In general, a metastable form will crystallise first before the most thermodynamically stable crystal form crystallises.(31) Although this is not a universal rule it is important to consider the stability of each polymorph and perform rigorous testing to determine the stability order of each polymorph. This is a non–trivial matter as many variables can impact polymorph crystallisation and will be discussed in the next section.

1.5 Polymorph generation

A variety of factors can influence which polymorph is generated including temperature and solubility. Solvent selection can impart selectivity on which form is obtained and their crystal morphology.(32) For example all five polymorphs of sulfathiazole can be crystallised using varying solvents with alcohol functionality and the morphology of FI could be modified from acicular to columnar morphology by addition of small amounts of methanol to 1–propanol. These habits are depicted in Fig. 3, with additional habits for comparison, and as one can see the two morphologies are different. If such a change were to occur in a manufacturing environment this could impact how one could go about processing the material. In this hypothetical example greater mechanical energy through use of a rotary mill may be required to break up the stronger columnar particles in comparison to that required for grinding the acicular particles to achieve a desired particle size for further downstream processes such as granulation, compression or sachet filling.

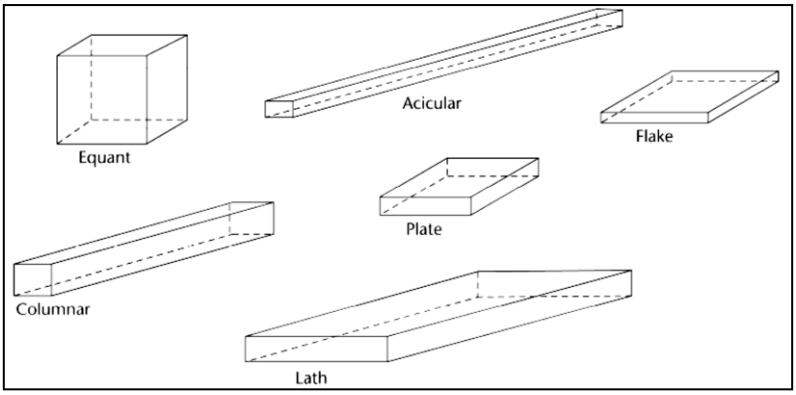

Figure 3 Schematic of crystal habits reproduced from USP monograph <776> Optical Microscopy.(33)

Further factors which can influence which polymorph is generated are humidity and temperature changes. In the case of mefenamic acid a conversion from the FII polymorph to the FI polymorph occurred over time when exposed to high relative humidities.(34) Increases in pressure can be exploited to generate further forms, examples include two forms of piracetam which are unstable at ambient pressure (35, 36) and metastable forms of paracetamol.(37) These metastable forms could then be used to seed crystallisation experiments at ambient conditions to generate the metastable form at room temperature. Additives can be used for selective crystallisation of polymorphs as in the case of L–glutamic acid where differing amino acid derivatives were used to suppress growth of the beta form in favour of the alpha form.(38) Similarly, impurities can play a similar role in mediating form generation. This is believed to have been the case in Ritonavir where a structurally similar compound, formed by a base catalysed degradation of the API, acted as a template for the formation of FII.(26) Self–assembled monolayers (SAMs) were used to generate polymorphs of 5–methyl–2–[(2–nitro phenyl) amino] 3–thiophenecarbonitrile (ROY).(39)

Pharmaceutical processing can impact the polymorphic forms produced and include roller compaction, milling, tableting and wet granulation. Transformations that occur via processing are referred to as process induced transformations (PITs). Transformations can additionally occur due to handling and storage of the API as well as interactions with excipients. An extensive review by Zhang *et al.* highlights the majority of phase transformation considerations that should be noted during process development and the manufacture of solid oral dosage forms.(40) Recent

literature includes a case where wet milling resulted in solid state transformations of an anti–cancer compound as a function of pressure where FII transformed to FI at pressures of 500–1500 bar and hydrate formation was noted at pressures greater than 1500 bar.(41) An additional example details form conversions on tablet surfaces of a caffeine formulation on compaction where PXRD was used to monitor form changes.(42)

1.6 Polymorphism of 5–methyl–2–[(2–nitro phenyl) amino] 3–thiophenecarbonitrile

5–methyl–2–[(2–nitrophenyl) amino] 3–thiophenecarbonitrile is highly polymorphic, more commonly known as ROY due to its polymorphs being red, orange and yellow in colour, Fig. 4.(43, 44) ROY is a precursor in the synthesis of Olanzapine, an atypical antipsychotic drug produced by Eli Lilly.(45) ROY exhibits concomitant polymorphism where two or more polymorphs can crystallise from the same solution concurrently.(46) To date, ten polymorphs of ROY have been discovered and it is the most polymorphic system to be found in the Cambridge Structural Database (CSD), seven of which were successfully characterised by single X-ray diffraction and the remaining three by Raman spectroscopy alone.(44)

Figure 4 Polymorphs of ROY, reproduced from Yu, 2011. (43)

*Polymorph nomenclature for ROY; O = orange form, ON = orange needles, OP= orange plates, ORP= orange red plates, R = red form, Y = yellow form, and YN = yellow needles.

ROY features conformational polymorphism which is due to the changing π–conjugation between the phenyl and thiophene rings as the torsional angle between the two rings, θ, changes.(47) This torsion bond angle varies by up to 83^{o} between polymorphs and is responsible for the variety of colours associated with the polymorphs. The following are in order of decreasing torsional angle θ from Y to R (Y ~ YN > OP > ON > ORP > R).* The C–C≡N angle deviates from the expected angle of 180˚ in all polymorphs, ON in particular (176.2˚). The oxygen of the nitro group and the amino hydrogen form an intra–molecular hydrogen bond in all polymorphs. None exhibit inter–molecular hydrogen bonds except polymorph Y, which is due to a short contact between the amino hydrogen of one ROY molecule to the cyano group of a neighbouring molecule. The remaining polymorphs are arranged together via van der Waal's forces. The polymorphs of ROY have been produced by a variety of methods including solution crystallisation,(43) vapour deposition on single–crystal substrates,(48) melt crystallisation,(49, 50) from liquids in contact with polymers,(51) gold islands,(39) and liquids within confined environments such as capillary tubes,(52) and porous solids.(53)

1.7 Amorphous Solids, Solvates and Co–Crystals

Further solid state forms include amorphous solids, solvates and co–crystals. Amorphous solids are made of randomly orientated molecules with no long range order and are thus non-crystalline.(54, 55) Amorphates can offer increased bioavailability; however as they are typically metastable their lack of long–term physical stability can pose development challenges.(29) Means of mitigating these issues include incorporation of the amorphous form into formulations by co–processing with suitable polymers in spray dried dispersions and hot melt extrudates to maintain physical stability by inhibiting crystallisation.(56, 57)

Solvates and co-crystals are similar in that both are multi component crystals containing the API with an additional molecule.(58) Solvates consist of the incorporation of some solvent into specific lattice sites with a defined stoichiometry. Where water is present as the solvent, its solvates are termed hydrates. Phase

transformations can occur from the solvated form to the non-solvated forms due to changes in temperature, relative humidity and degree by which the solvate molecule is bound to the lattice. Co-crystals consist of an additional molecule which is a solid at room temperature – such molecules are termed co-crystal formers. In API formulations co-crystallisation of APIs with suitable excipients represent a new category of pharmaceutical material. Apart from the possible benefits in bioavailability, stability and solubility, co-crystals present a viable opportunity to improve manufacturing characteristics such as compressibility, hygroscopisity and flowability of a compound.(12, 20, 23, 59, 60)

1.8 Regulatory Filings

Extensive solid state screening of candidate APIs prior to scale–up and formulation can enable an informed choice as to which solid form will perform as intended and is a prerequisite from regulatory bodies for newly developed drugs. For both new drug applications (NDAs) and abbreviated new drug applications (ANDAs), the US Food and Drug administration (FDA) requires near–total characterisation of the API.(61, 62) These include specifications relating to solubility, purity, morphology, particle size, surface area, crystal properties and detailed investigations of the influence of the structure of the API and its formulated product on stability and dissolution *in vivo*. International Conference on Harmonisation (ICH) guidelines which have been adopted across a number of regulatory agencies incorporate a series of decision trees (Fig. 5 and 6) to aid in the assessment of the impact of polymorphism in drug substance and products.(62, 63) Detection and quantification of low levels of an undesired solid state form present in a formulation is required from a quality assurance point of view, particularly where the two polymorphs are not bioequivalent. Establishing analytical methods to determine low levels of alternate polymorphs in formulations can impart increased confidence that these forms can be detected should they be present at the time of production or develop throughout the product's shelf–life.

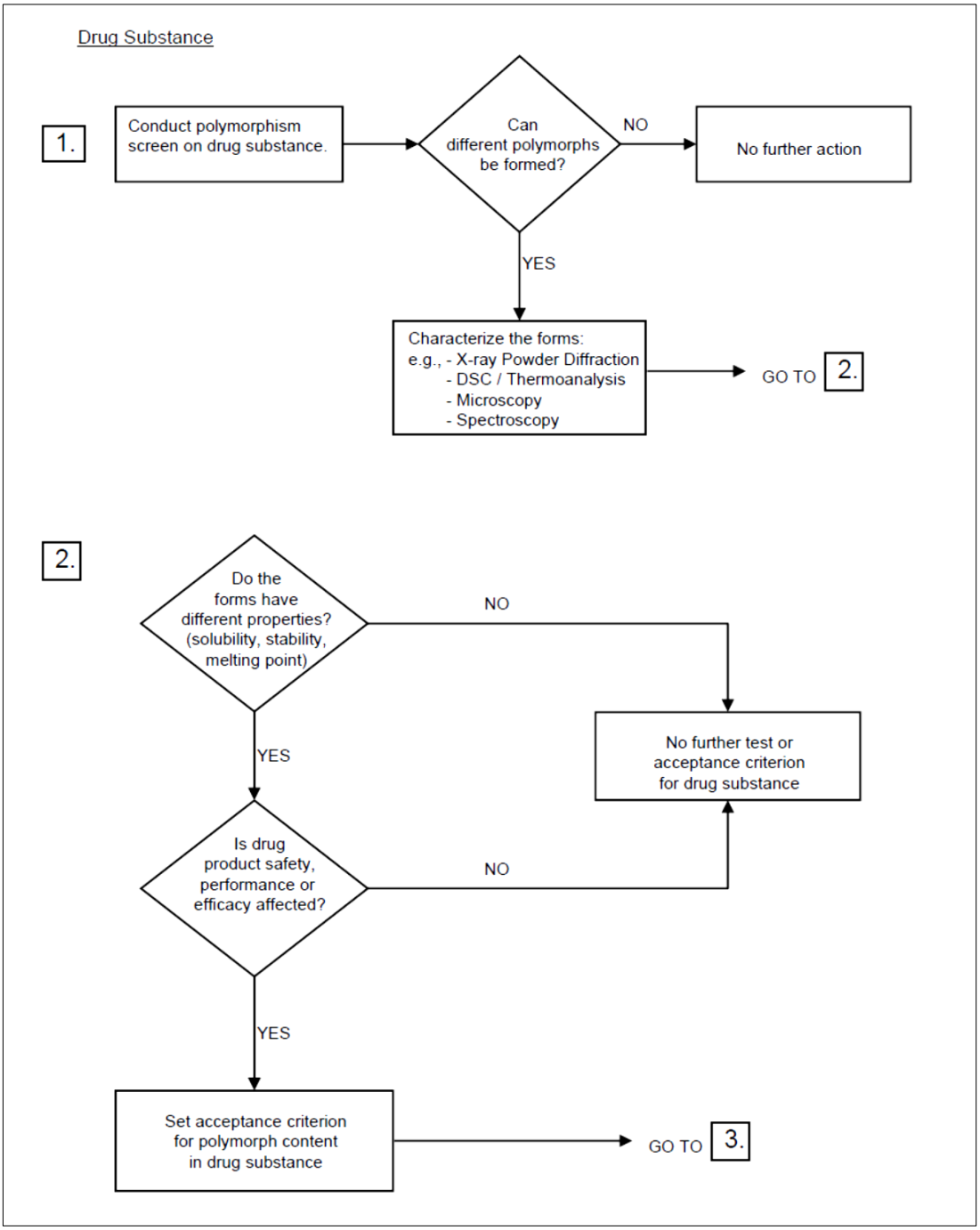

Figure 5 Drug substance decision trees reproduced from ICH Q6A guidelines. (64)

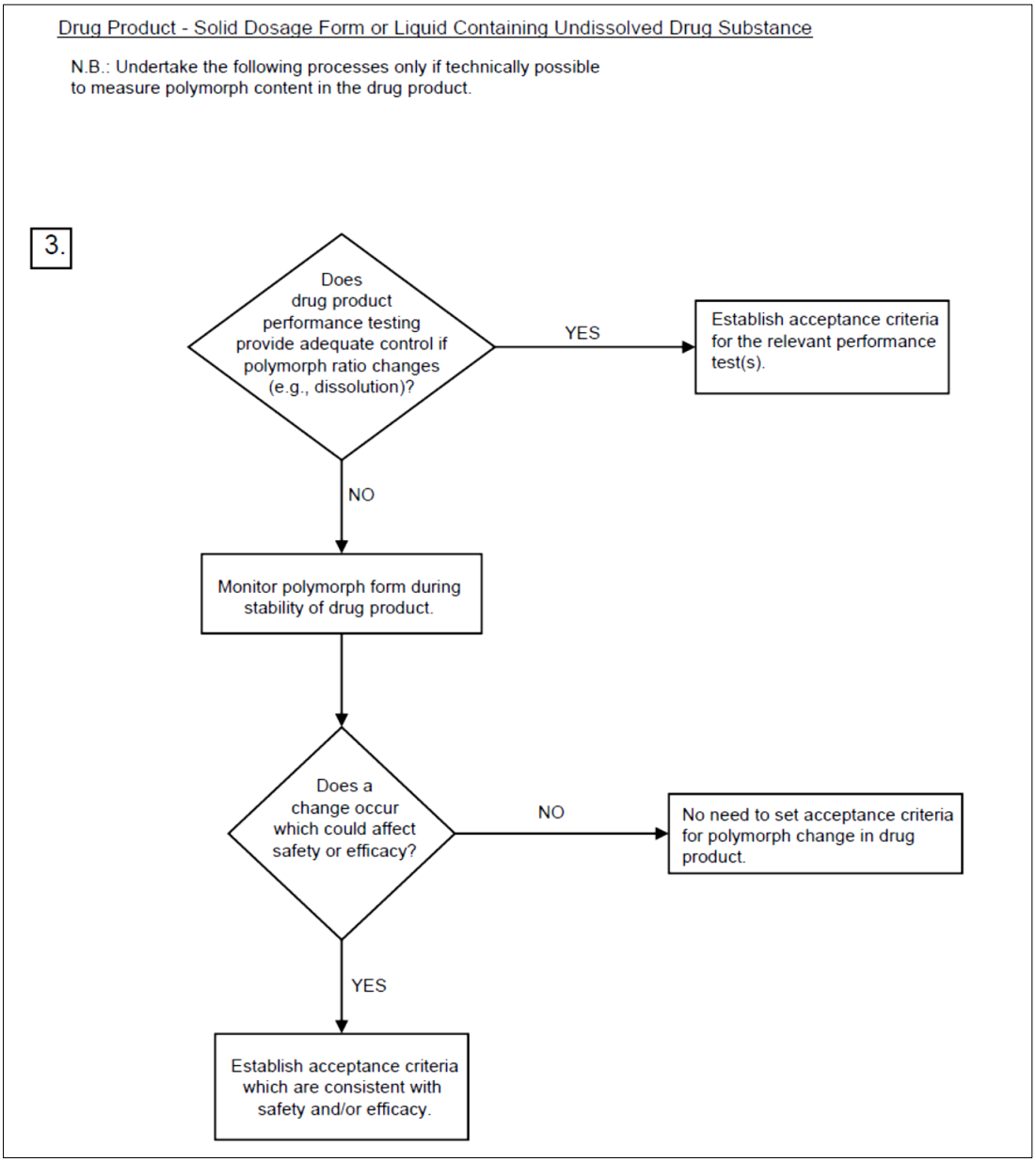

Figure 6 Drug product decision trees reproduced from ICH Q6A guidelines.(64)

1.9 Patent infringement

Incidences of polymorphism can also provide unfavourable patent issues where not all polymorphs or solid state forms of an API are provided and documented in a patent, providing opportunities for competitors to generate new polymorphs which may possess similar or improved performance characteristics. Conversely, discovery of new polymorphs can expand the range of possible development strategies and offer a means to extend patent protection. GlaxoSmithKline's (GSK) discovery of a

new polymorph of ranitidine hydrochloride enabled GSK to submit a new patent for this newly found polymorph which extended the product life and their production exclusivity of Zantac, for which ranitidine hydrochloride is the active ingredient. This new polymorph also offered improved filtering and drying characteristics.(48) Litigation ensued when a generic competitor, Novopharm, wished to produce a generic product containing the original polymorph used by GSK on expiry of the patented original form. Novopharm challenged the original patent by claiming that there was no way to produce the off patent polymorph from the original patent as described by GSK, Novopharm could only generate the newly patented form by the method described for GSK's newly patented polymorph.(43) Independent studies confirmed that it was possible to prepare the original polymorph as described by the original patent. GSK contended that Novopharm were in breach of the later patent for the new polymorph alleging that there must be seeding of Form II occurring and that Novopharm could not be producing a pure Form I drug substance. Later Novopharm were able to demonstrate using PXRD patterns that they were able to produce Form I with no detectable contamination of Form II and were thus granted approval to market the product.(44, 51) Additional examples of patent litigations dealing with polymorphs include Cefadroxil, Paroxetine Hydrochloride, Pantoprazole Sodium and Terasosin Hydrochloride.

2 Analytical techniques for solid–state analysis

2.1 Vibrational spectroscopy

Vibrational spectroscopy is very sensitive to small force field changes caused by structural changes in molecules caused by solid state transformations and polymorphism. In polymorphism, the vibrational modes associated with each crystal lattice can vary which can result in unique band positions specific to each form allowing for their identification.(65) Raman and NIR spectroscopy are based on different phenomena and are governed by their own specific selection rules which will be discussed below.

2.2 Molecular vibrations

The bonds within molecules are in constant motion via vibrations, rotations and translations. Atoms connected together by chemical bonds displace one another in relation to the other in a frequency that can be defined by the strength of the bond and the mass of the individual bonded atoms or the groups attached. In the simple Harmonic Oscillator approximation the chemical bond between two atoms is considered to act like a perfectly elastic spring, which can be described by Hooke's law where the restoring force exerted by a spring is proportional to its displacement where k is the restoring spring constant;

$$F = -kx$$

Force is related to potential energy by F = –dV/dx and expressed as follows;

$$V = \frac{1}{2}kx^2$$

The energy of a harmonic oscillator is quantized;

$$E = h\tilde{\upsilon}\left(v + \frac{1}{2}\right)$$

The vibrational terms of a molecule can be expressed as follows where E = hcῡ;

$$\tilde{\upsilon} = \frac{1}{2\pi c}\sqrt{\frac{k}{\mu}}$$

where μ represents the reduced mass of a diatomic molecule given by;

$$\mu = \frac{m_1 m_2}{m_1 + m_2}$$

A molecular potential energy curve characteristic of a harmonic oscillator is depicted in Fig. 5 below. This approximation consists of a potential energy well that is symmetrical between the binding potential of the bonding electrons and the repulsive forces between the atomic nuclei with evenly spaced energy levels. This approximation takes no account of bond dissociation and although it can be a good estimate of the distance between lower energy levels it fails at higher excitation energies. An additional restriction is that transitions can only occur from one level to another which is adjacent to it.

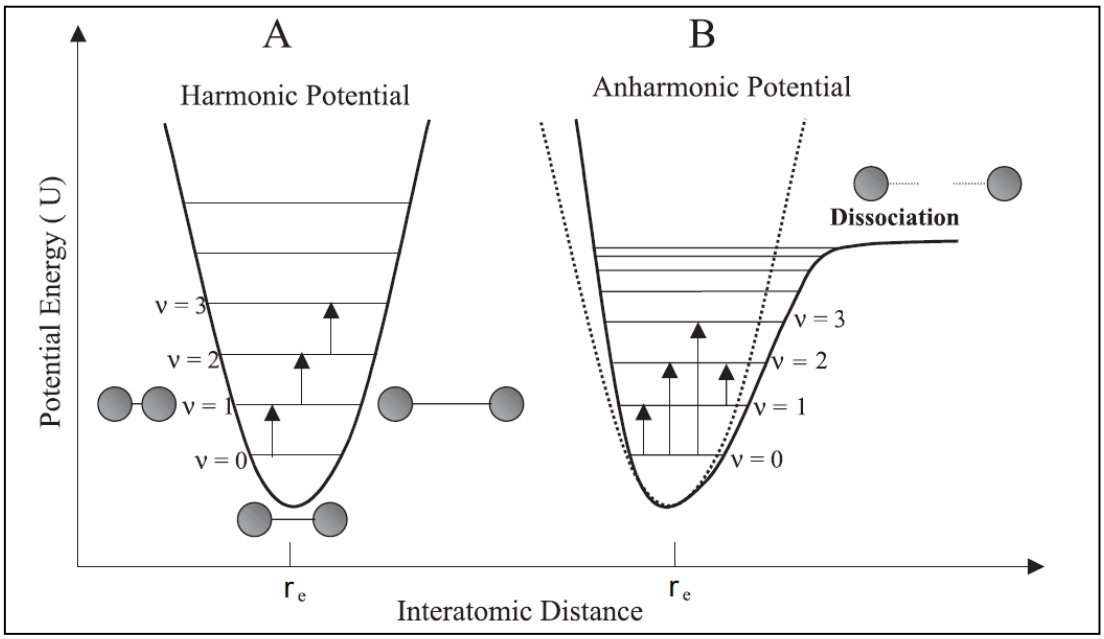

Figure 7 Molecular potential energy plots, adapted from Pasquini *et al.*(66)

A more realistic approximation accounting for anharmonicity is the Morse potential energy curve where the number of bound levels is finite and the spacing between each energy level converges as the number of energy levels increases until the dissociation energy is reached (Fig. 5). The potential energy of the anharmonic model can be expressed as;

$$V = D_e\left[1 - e^{-a(r-r_e)}\right]^2$$

where *a* is the constant for a given molecule, D_e is the spectral dissociation energy, r is the distance between the atoms and r_e is the equilibrium distance between the atoms. Applying quantum mechanics to the Morse equation results in the vibrational levels being described by the following equation;

$$E = h\tilde{\upsilon}\left(v + \frac{1}{2}\right) - x_m h\tilde{\upsilon}\left(v + \frac{1}{2}\right)$$

where x_m is the anharmonicity constant of the vibration. Transitions from one energy level to others non–adjacent to the originating energy level can occur as well as the existence of combination bands between vibrations. The vibrations are no longer independent of each other and can interact with one another. The strength of an absorption depends on the number of molecules in a particular energy level and this is governed by the Boltzmann distribution;

$$N_i = \frac{Ne^{-E_i/kT}}{q}$$

where N_i is the number of molecules in an energy level with energy E_i, N is the total number of molecules in system, *k* is the Boltzmann constant, T is temperature and *q* is the partition function.

Vibrations, rotations and translations of the atomic bonds are a result of the interaction of photons with the molecule. For a polyatomic molecule the presence of N atoms results in 3N degrees of freedom. For a linear molecule three co–ordinates

are enough to define the center of gravity of the molecule and to describe the translational motion of the molecule. For a non–linear molecule three additional co–ordinates are required to specify the orientation of it resulting in 3N – 6 vibrational degrees of freedom. For a linear molecule this is 3N – 5 as only orientational co–ordinates are necessary.(67)

2.3 Raman Spectroscopy

Raman observed the Raman effect in 1928 and was awarded the Nobel prize in Physics two years later for this discovery. The Raman effect occurs when the interaction of a molecule and an electromagnetic field results in inelastic scattering of an incident photon.(68, 69) Radiation may be scattered in two ways, elastically and inelastically, Fig. 8. The elastic scattering of light is referred to as Rayleigh scattering where there is no change in the energy of the photon on interaction with radiation. Roughly 99.99% of light is scattered in this manner. Radiation inelastically scattered is the Raman effect and is due to the interaction of photons with molecules which results in an exchange of energy where radiation is scattered at differing frequencies corresponding to vibrational excitation and de–excitation of the molecule.

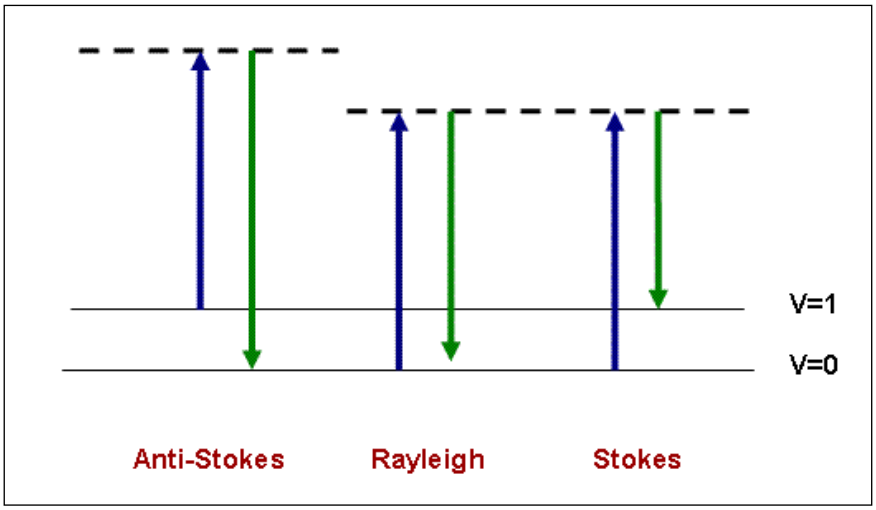

Figure 8 Schematic energy level diagram highlighting the three different ways in which light can scatter. V=0 corresponds to the ground state and V=1 corresponds to an excited vibrational energy state.

The Raman effect relies upon a change in polarizability of a molecule by the electric field of incoming light. (69) This can be expressed mathematically where the dipole moment, P, induced in a molecule by an external electric field, E, is proportional to the electronic field. The proportionality constant, α, is the polarizability of the molecule.

$$P = \alpha E$$

Polarizability measures the ease with which the electron cloud around a molecule can be distorted. The induced dipole emits or scatters light at the optical frequency of the incident light wave. The main selection rule of Raman spectroscopy is that for a Raman active vibration there must be a change in polarizability during the vibration. If a vibration does not greatly change polarizability, the intensity of the Raman band will be low. Bond bending and/or stretching substantially changes electron density distribution of bonds resulting in bands of stronger intensity. Changes in polarizability as a result of the molecular bonds stretching and vibrating allows for the molecular identification of the entity of interest by Raman spectroscopy.(67, 69) Typical strong Raman scatterers are moieties with distributed electron clouds i.e. C=C. The π electron cloud is easily distorted in an external electric field. Many APIs contain aromatic functional groups with symmetric vibrational modes and are strong Raman scatterers, while most pharmaceutical excipients lack aromaticity rendering them poor Raman scatterers.(70)

As Raman is based on a scattering phenomenon it allows for little or no sample preparation and enables facile *in–situ* analysis. Further advantages include sampling in aqueous media, as water is weakly Raman active, and remote sampling by use of fiber optics. Drawbacks include fluorescence, sample degradation by high intensity light illumination, poor sensitivity at low analyte concentrations and expense of instrumentation. Fluorescence is observed in spectra by a broad high intensity band which can smother some or all of any information pertaining to the Raman effect. Fluorescence involves the absorption of energy by a molecule elevating it to a higher energy state which rapidly returns to the ground state by emission of a photon with energy equal to the difference between the higher energy and ground energy states.(71) It is a phenomenon which can be orders of magnitude greater than the Raman effect. In some instances this can be mitigated by selection of an appropriate,

typically NIR (1064 nm), laser excitation wavelength and careful utilisation of suitable pre-processing measures.(69, 72)

2.3.1 Backscattering and Transmission Raman

In Backscattering Raman spectroscopy (BRS) the excitation light impinges on the surface of the sample and the Raman signal is collected at an angle of 180° to the spectrometer. Using this typical configuration, the sampling volume is located primarily at the surface and the immediate sub–surfaces of the sample and is determined by a combination of opacity and scattering potential of the material in combination with instrument parameters. In Transmission Raman spectroscopy (TRS) a collimated laser beam is incident on one side of the sample and the Raman signal is collected from the opposite side after passage through the whole of the sample.(73, 74)

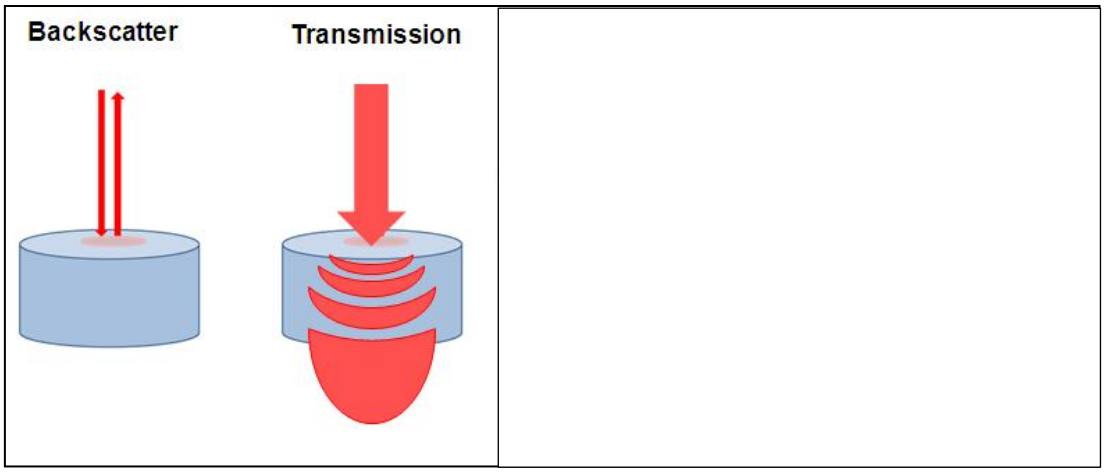

Figure 9 Schematic of Backscattering and Transmission Raman collection geometries. On the right a Monte Carlo simulation of Raman signal generated by TRS adapted from Macleod *et al.* (81)

The main difference between these two geometries which is critical, is the sampling volume accessible with each, Fig. 9. In BRS as the Raman signal generated is typically representative of the immediate layers just below the surface where the laser point has penetrated, sub–sampling can be the main limitation of this geometry.(75) This can be mitigated somewhat by the use of surface mapping where the laser collects a spectrum from each point on a pre–determined mapped out area

of the sample surface, by sample rotation or by use of probes which allow for larger laser spot sizes, often termed as wide area illumination to irradiate the surface (i.e. PhAT probe, Kaiser Optical Systems Ltd. as used in Wikstrom *et al.* and Allan *et al.*).(76-78) Johansson *et al.* conducted a study comparing four different laser irradiation layouts as shown in Fig. 10. The layouts were as follows; point irradiation consisting of a total of 5 points, two circle patterns of 2.5 and 5 mm diameter where spectra were acquired from the circles' perimeter and a 5 mm diameter circle where the entire area of the circle was analysed. This study demonstrated the sub–sampling issues associated with the various irradiation patterns and intuitively it was found that irradiation of a larger tablet surface area resulted in quantitative models with lower prediction errors.(75)

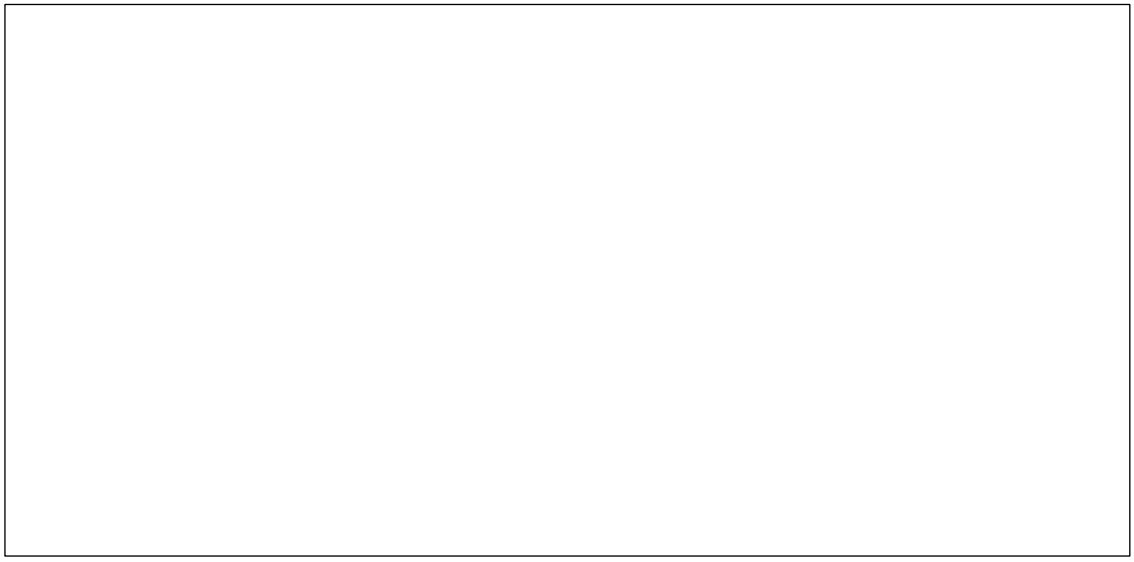

Figure 10 Adapted from Johansson *et al.* (75) Irradiation layouts to the left of the image and to the right PLS calibration plots of prediction of API content vs. UV reference values for each laser irradiance pattern.

Unfortunately mapping generally does not solve the penetration depth issue. Additionally the use of mapping can be accompanied by a severe time penalty. For example, in the case of tablets manufactured from a non–uniform powder blend of multiple components, any heterogeneity due to this poor sample mixing could impact accurate quantitation. In the case of typical pharmaceutical solid dosage forms, many incorporate surface coatings, allowing ease of ingestion or control over the location of drug release such as enteric coatings, and signals arising from such coatings can swamp signals pertaining to the API or the excipients found within the tablet mass.

In TRS the Raman signal is more representative of the entire tablet undergoing study as Raman photons can be generated at any point at which the collimated laser beam passes through the tablet to reach the detector on the opposite side.(73) Larger spot sizes are typically used, thus sampling a much greater proportion of the tablet. This reduces the issue of sub–sampling leading to spectra which are more representative of the tablet bulk. TRS was demonstrated by Schrader and co–workers as far back as 1967 however it is only now within the past decade that interest in TRS has returned, due to advancements in instrumentation, with a number of pharmaceutically relevant studies highlighted in Table 1.(79)

This is due in part to the development of spatially offset Raman spectroscopy (SORS), where the laser beam and its point of contact with the sample and the Raman collection zone are spatially offset on the sample surface. Depending on the spatial offset used, Raman spectra can be collected from different depths within a sample as those photons originating from deeper within the sample can be spread further apart as they reach the surface.(80) Such spectra can contain some lingering Raman signal pertaining to the surface layer and this can be eliminated from the spectra by spectral subtraction returning a Raman spectrum representative of the sample contents. This has applications in the security and pharmaceutical raw material identification fields as SORS allows for analysis through material packaging such as paper sacks or solid plastic containers without the requirement for sampling bulk materials as is currently the case within pharmaceutical companies.(81-83) Such an example is provided in Fig. 11 for neopentyl glycol which was analysed through its blue plastic sack packaging. A BRS spectrum was acquired and although it contains some features of the glycol it heavily features a Raman signal due to the packaging material (low density polyethylene glycol – LD-PE) and from 200 – 1000 cm^{-1} this swamps any Raman signal of the glycol from the spectrum. The SORS spectrum does not have this issue and matches quite closely the glycol reference spectrum generated across the entire spectral range.

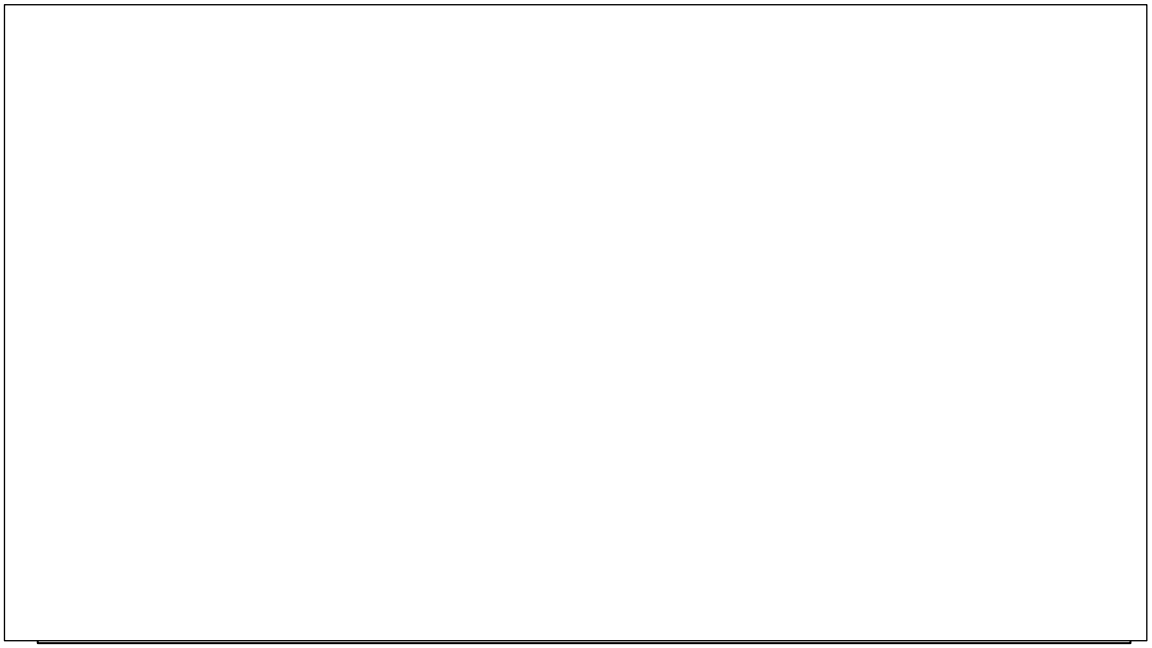

Figure 11 Adapted from Bloomfield *et al.* (83) SORS and BRS Raman spectra of neopentyl glycol through LD–PE sacks with reference spectra of the individual materials.

TRS can effectively be viewed as an extreme case of SORS where the laser beam and Raman collection zone are separated by the maximum by being located on opposite sides of the tablet. In a direct comparison of BRS and TRS, experimental work and Monte Carlo simulations of a pharmaceutical tablet–like system was undertaken where an impurity layer of paracetamol was moved from the sample surface to a depth of 3 mm within the tablet medium of trans–stilbene, Fig. 12.(73) The simulations supported the experimental work where it was found that TRS was able to detect the impurity layer's presence no matter where the layer was located i.e. at the top, middle or bottom of the tablet–like medium. The particular BRS set–up employed for the same analysis was incapable of detecting the impurity at any other layer than when it was present as the surface layer. Characteristic peaks of paracetamol in the 1200 – 1480 cm^{-1} spectral range were absent in the BRS spectrum when this layer was located at the bottom of the tablet medium unlike TRS spectra where all peaks were present. Further studies detail experimentally the sub–sampling issue associated with BRS and the lack thereof associated with TRS and will be discussed in Section 2.5. (84, 85)

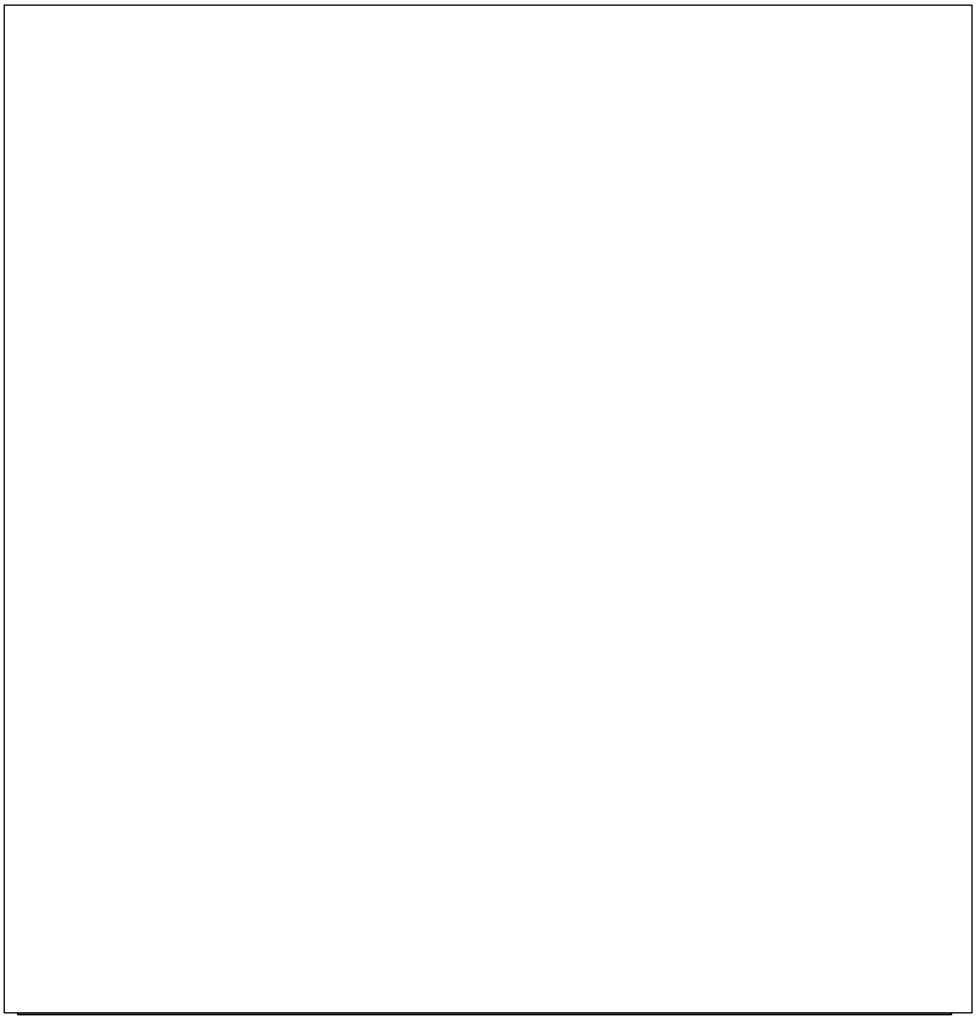

Figure 12 Adapted from Matousek *et al.* (73) Raman spectra obtained from a two–layer sample (3.9mm thick paracetamol tablet and 2mm thick trans–stilbene powder layer) using (a) conventional backscattering geometry and (b) transmission geometry. The measurements are performed at twos ample orientations, with paracetamol at the top and at the bottom of the trans–stilbene cell, as indicated in the graphs. The top and bottom spectra are those of paracetamol and trans–stilbene, respectively, obtained in separate experiments. Legend: p – paracetamol, t – trans–stilbene, R – Raman light, L – laser beam.

Table 1 Summary of pharmaceutically relevant transmission Raman studies.

Year	Compound	Synopsis	Results	Reference
2007	Undisclosed API	Comparison of TRS and BRS for quantitation of unknown API in tablets.	PLS model RMSEP for API content within tablets of 2.2% and 2.9% for TRS and BRS respectively. Capsules have a RMSEP of ± 3.6%. Leaner calibration models can be built using 2 or 3 calibration spectra.	Johansson *et al.* (84)
2008	Undisclosed API	Analysis of production capsules filled with unknown API and 3 excipients by TRS.	CLS and PLS models built where PLS reported a RMSEP of ± 1.2% with 5 s acquisition time.	Eliasson *et al.* (86)
2010	Flufenamic acid	Analysis of binary polymorph mixtures by TRS and BRS.	TRS offers improved modelling of system with increase of percentage of variance for first loading in comparison to BRS; 98.09% and 89.7% respectively.	Aina *et al.* (87)
2010	Co–crystals of salicylic acid–nicotinic acid; and DL–phenylalanine,6HNA, and 3,4–dihydroxybenzoic acid with oxalic acid cocrystals	Characterisation of co–crystals by TRS, BRS, PXRD and DSC.	Low wavenumber Raman bands accessed using TRS suitable for identification of co–crystals from co–crystal formers.	Elbagerma *et al.* (88)
2010	Paracetamol	Tablets of API and 4 excipients analysed using TRS and multiple multivariate techniques.	PLS, CLS and MCR comparable in prediction performance; 2.4–3.4%. Simple lean calibrations with few components were generated using TRS data.	Fransson *et al.* (89)
2011	Undisclosed API	Capsules comprising API and 3 excipients studied by TRS.	RMSEP of 1.5% reported for API concentration. TRS insensitive to capsule fill weight, allowed for a model made from a batch at a single fill weight to be applied to batches of varying fill weights.	Hargreaves *et al.* (85)

Table 1 (continued) Summary of pharmaceutically relevant transmission Raman studies.

Year	Compound	Synopsis	Results	Reference
2012	Ranitidine hydrochloride	Comparison of BRS to TRS for quantification of polymorphs in a spiked commercial formulation.	Powder models of MCC and binary polymorph mixture. Spiked tablets and capsules. More accurate PLS models yielded for tablets than capsules. RMSECV 4.80 and 2.40% for capsules and tablets. RPD reported of 14.62 and 7.42% for tablets and capsules.	McGoverin *et al.* (90)
2012	Flurbiprofen and nicotinamide co–crystal	TRS for supervised classification of model co–crystal tablet formulations.	PCA can discriminate between two APIs and co–crystal in second loading. First loading concerned with amount of APIs present.	Burley *et al.* (91)
2012	Sulfur	Effect of particle properties of MCC powders in TRS.	TRS signal intensity found to be sensitive to particle size differences.	Townshend *et al.* (92)
2012	Chlorpheniramine maleate	Quantification by TRS and BRS of API at 2% w/w level within marketed tablets by use of external calibration samples	MCC of differing particle sizes were incorporated into calibration samples. TRS was found to be sensitive to particle size differences. BRS and TRS results were in agreement with HPLC.	Townshend *et al.* (93)
2012	Ambroxol	Study of effects of coloured capsule shells on API prediction models.	Formulation containing capsules showed a slight decline in PLS prediction accuracy due to weak fluorescence of blue and green coloured capsules.	Lee *et al.* (94)

2.4 Near Infra–red Spectroscopy

Near infra-red spectroscopy (NIR) was championed 50 years ago by Karl Norris during his studies of moisture content in agricultural products.(95) Since then its applications have grown exponentially and its development and widespread use has been aided by the technological progression of instrumentation, fiber optics and new mathematical methods allowing data treatment. Such developments have facilitated the growth of NIR substantially in it's application as a quality control technique in the pharmaceutical industry.(96)

NIR refers to the region of the infra-red spectrum closest to the visible light region which is specified as the region lying between 750 and 2500 nm. The region can be divided into 3 sub–regions;

- Region I (800–1200 nm) where 2^{nd} and 3^{rd} overtones and combination modes of XH (X = O, N, C) stretching vibrations are present.
- Region II (1200–1800 nm) where 1^{st} overtones of XH stretching vibrations and various types of combination modes of XH stretching vibrations are found.
- Region III (1800–2500 nm) is the combination mode region. Overtones, if present, can be attributed to the 2^{nd} overtones of carbonyl stretching vibrations.

Overtones occur at integral multiples of fundamental bands. Combination bands appear near the sum or difference of two or three fundamental bands. Under the quantum Harmonic Oscillator approximation, overtones and combination modes are known as forbidden transitions and should not occur. As detailed in Section 2.2 only transitions from one level to another adjacent to the originating level is permitted in the simple harmonic oscillator approximation. Additionally the vibrations under this approximation would be independent and their combinations would not exist. A better approximation is that of the anharmonic model using the Morse potential which accounts for transitions greater than one and combination bands between vibrations. Since these bands are weaker, the NIR region has an excellent

permeability to IR radiation which allows non–destructive analysis and experimentally allows for a thicker/longer sampling path–length to be used.

For a band to be IR and hence NIR active it must exhibit a change in its dipole moment during a vibration and if the resonant frequency of the vibrating bond matches that of the incident radiation, absorption will occur. Molecules that absorb NIR energy vibrate in stretching and bending modes. Stretching is the continuous change in the interatomic distance along the axis of the bond between atoms. Bending is defined as changes in bond angles. Functional groups such as C–H, N–H, S–H and O–H feature strongly in NIR spectra. C=O and C–C bonds can also be evident in NIR spectra when combined in overtone–combination bands with the aforementioned functional groups. The bands in the resultant spectra are typically broad which can overlap making band assignment challenging. The development of mathematical methods in the field of chemometrics has allowed for band interpretation and NIRS coupled with chemometrics is a powerful technique in the identification and quantification of components in samples such as tablets or reaction vessels.

Analysis of solid samples using NIR spectrometers is generally performed using two modes of sampling, transmittance and diffuse reflectance. Transmittance can be described by the Beer Lambert Law where the ratio of intensities for light transmitted through a given path length is related to the materials molar absorptivity, and concentration as follows;

$$A = log\frac{I_0}{I} = eCl$$

This works well for materials in solutions however in terms of solid samples the radiation can not only be absorbed or transmitted, which the Beer–Lambert Law assumes; the radiation can interact with the solid materials through diffuse reflection, diffuse transmission, specular reflection or transflection. A more suitable means of describing this relationship is through the Kubelka–Munk equation: (97)

$$f(C) = \frac{(1-R)^2}{2R}$$

where R is the diffuse reflectance, obtained by:

$$R = \frac{I_R}{I_{R0}}$$

where I_R is the intensity of radiation reflected by the sample and I_{RO} is the same quantity reflected by a non–absorbing material over the full spectral range of measurement. This treatment is valid for transparent homogeneous materials and establishes a linear relationship between concentration and diffuse reflectance. In analytical development the following relationship is employed where, for small changes in reflectance, it is presumed there is a linear relationship between reflectance and the concentration of the analyte.

$$f(C) - \mathrm{Log}\frac{1}{R}$$

2.5 Raman vs. NIR

Both types of spectroscopies rely on differing phenomena to occur and are governed by different rules. The Raman effect is due to the inelastic scattering of light which changes the polarizability of a molecule whilst NIR involves the absorption of light where a change in the dipole moment of the molecule results in a NIR spectrum. It has been shown from group theory that if a molecule has a centre of symmetry, vibrations which are Raman active will be silent in IR and vice versa.(95) This is known as the rule of mutual exclusion. Such an example is that of CO_2, where the symmetric stretch of this centrosymmetric molecule causes a change in polarizability resulting in a Raman active vibration. The anti–symmetric stretch of CO_2 results in a change in the dipole moment of the molecule and is an IR active vibration. Raman and IR can be considered as complementary techniques in that they provide different information that the other cannot due to their different selection rules.

NIR shares with Raman spectroscopy similar advantages; for example, little or no sample preparation is required and the sample can be of various shapes, thicknesses and physical states; analysis can be performed *in–situ*, in reactor vessels or storage containers as it is suitable to be coupled with fiber optics which allows for remote operation and analysis of on–line processes.(98) NIR, though not as sensitive as MIR to water, is moisture sensitive and is useful for quantification of water absorption in tablets unlike Raman where water is a poor Raman scatterer. Raman spectra exhibit high chemical specificity, consisting of sharp well resolved bands which assist facile monitoring of fundamental vibrational modes, whereas NIR spectra consist of overtones and combination modes of fundamental molecular vibrations that occur in the IR region. The spectra typically consist of broad and often overlapped bands which are difficult to assign so spectral assessment is further compounded by this. NIR is also sensitive to physical differences in samples such as tablet hardness or excipient particle size within spectra. (99, 100) Recent studies by TRS show that it too can also be sensitive to particle size effects as was found to be the case for different particle sizes of MCC in aspirin and chlorpheniramine maleate containing samples.(92, 93)

A further drawback of NIR for quantitative analysis is the requirement of large calibration data sets with plenty of variation for the generation of a robust NIR calibration model.(98) For pharmaceuticals, normal production conditions or batches of pharmaceutical formulations should not deviate much in terms of sample characteristics such as API loading or hardness. For robust NIR calibration models to be generated, formulations outside of the normal specifications should be produced to allow for model development.(101)

Lean calibration opportunities by spectroscopic means could have potentially great impact in early development pharmaceutical manufacturing settings where there may be few tablets available for analysis. For TRS it has been shown that far fewer samples are required for calibration set generation to build a quantitative model for propranolol; as the number of samples decrease the RMSEP associated with TRS models remains relatively unchanged.(84) This contrasted with BRS where the RMSEP increased with decreasing calibration samples (Fig. 13). Another example of

the lean calibration of TRS by the previous authors demonstrated no difference in prediction errors between calibration models built using only two samples and using half the available samples (18 tablets in total).(89) .No reports of a direct comparison between NIR and TRS for the generation of lean calibration models has been reported thus far in the literature.

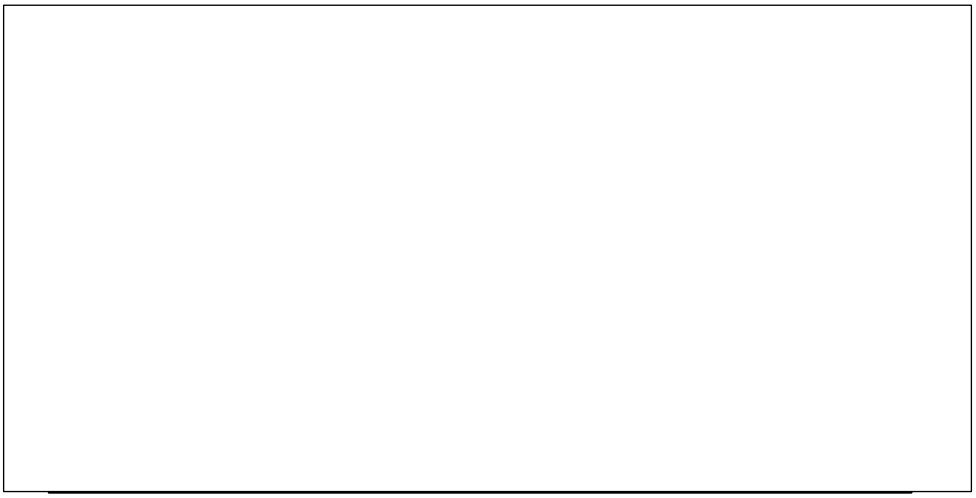

Figure 13 Plot describing the effect on RMSEP of reducing the number of samples used for generation of calibration models by BRS (open circles) and TRS (black circles) reproduced from ref (84).

2.6 Powder X-ray diffraction

Powder X-ray diffraction (PXRD) can be considered to be the definitive method in the characterisation and identification of solid state crystalline forms in powders. Since polymorphs and all other solid state forms differ in their crystal structures such differences lead to the characterisation of individual forms.(102) PXRD patterns result from the fulfilment of the Bragg formula when an X-ray hits an atom in a crystal lattice and is diffracted according to the following equation;

$$n\lambda = 2dsin\theta$$

where λ is the wavelength of the X–ray radiation, d is the distance between individual parallel planes in a crystal lattice and θ is the angle between the incident radiation and the set of parallel planes at which constructive interference results. Diffraction patterns are obtained by measuring the intensity of scattered waves as a function of scattering angle.

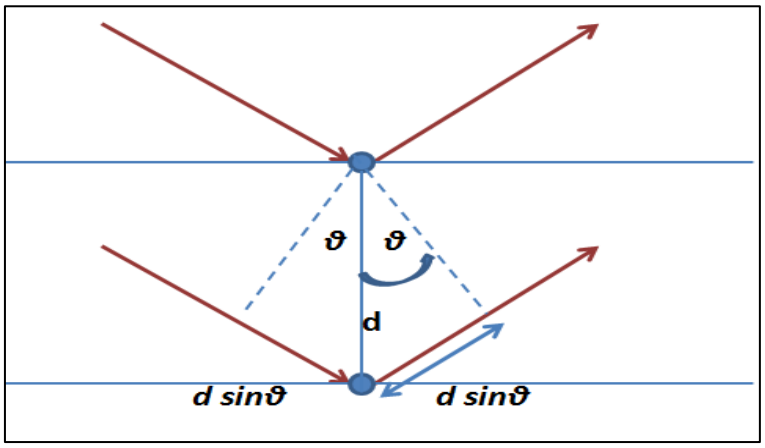

Figure 14 Schematic of Braggs law.

In comparison to spectroscopic methods, PXRD can be more time intensive as samples must be analysed off–line often requiring a longer analysis time, minutes compared to the seconds required for spectroscopy. Furthermore PXRD can be sensitive to particle effects such as preferred orientation where the samples may arrange themselves in the sampling compartment in such a way that only certain faces of the crystals/fine powder are exposed resulting in diffraction patterns that are not truly representative of the bulk crystalline material.(102) This can be observed in PXRD patterns by peak intensity variation. This effect can be reduced by grinding of the samples to reduce particle size as long as such grinding causes no solid state changes and by rotation of the sample during analysis.(103)

Crystalline compounds show strong diffraction patterns, typically featuring sharp, high intensity peaks in a diffractogram. Compounds of low crystallinity tend to exhibit peaks of weak intensity and in amorphous compounds a "halo" effect (apparent in top diffraction patterns depicted in Fig. 15) is observed where a broad featureless band encompasses the diffraction pattern resulting in qualitative and quantification challenges. Chieng *et al.* generated the amorphous form of ranitidine hydrochloride by cryo–milling the API and were able to demonstrate decreasing crystallinity and increasing amorphous content in the compound by PXRD (Fig. 15).(104)

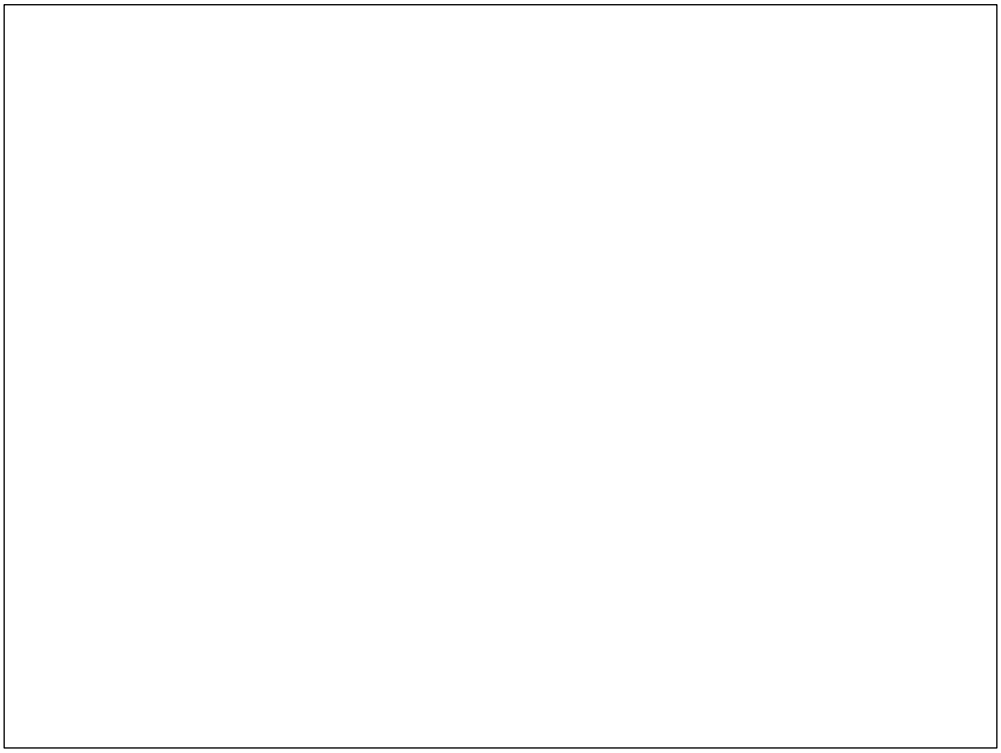

Figure 15 PXRD diffraction patterns of ranitidine hydrochloride demonstrating the conversion of crystalline polymorphic forms to amorphates on cryo–milling over extended periods of time. Reproduced from Chieng *et al.* (104)

From PXRD patterns it is also possible to determine the components and their concentrations in multi–component mixtures as long as there is limited interference to the peaks of interest, for example the quantification of API in a powder formulation containing several excipients.(105, 106) In all patent submissions to the regulatory agencies, powder patterns and crystallography data are required, as unique crystal structures provide definitive evidence of non–equivalent crystal structures. PXRD in combination with vibrational spectroscopic techniques has been widely used to study multicomponent mixtures. (11, 105, 107-110)

2.7 Pharmaceutical applications of Raman spectroscopy

Raman spectroscopy and its use in pharmaceutical settings has grown substantially in recent decades with examples including quantification of polymorphic mixtures, tablets, capsules and for inline analysis of fluid bed drying processes.(70, 84, 111-113) Its uses have been highlighted by extensive reviews and a book on the subject.(70, 113-119) Pharmaceutical materials are ideal to study by Raman

spectroscopy as they are typically strong Raman scatterers due to the presence of aromatic functional groups with symmetric vibrational modes contained within the API molecule whose changes in polarizabilities cause Raman scattering.

Raman has been used to qualify and quantify components of multi component mixtures including powder mixtures,(105, 120, 121) tablets,(110, 112, 122) and suspensions.(123) Raman can be used to monitor solid form changes including PITs and solid state transformations of the API occurring in production settings.(124, 125) In addition Raman has successfully been utilised to study the effect of storage conditions such as humidity, pressure, grinding and temperature on APIs as summarised in a recent review by Chieng *et al.* (126)

Modern instrumentation and improved optical filters provide the necessary Rayleigh rejection filtering to analyse down to low wavenumbers. The spectral region from ~45–400 cm^{-1}, the phonon mode region, is associated with crystal lattice vibrations which will show differentiation between polymorphs as they can have non–identical crystal structures. This can be demonstrated by indomethacin as reported by Hédoux *et al.* where clear differences between both polymorphs and the amorphous form are evident in low wavenumber spectral regions, Fig. 16.(127) Other examples of utilisation of this region include Raman analysis of thermally induced phase transitions of paracetamol.(128)

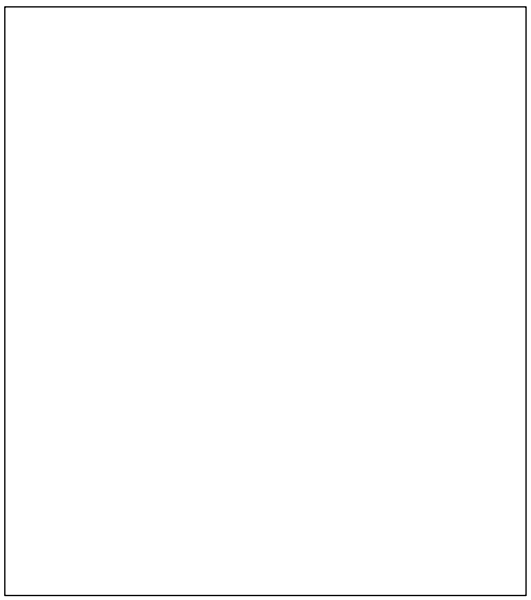

Figure 16 Raman spectra of the phonon mode region of three solid state forms of indomethacin as reported by Hedoux *et al.* (124)

2.7.1 Quantitation of polymorph mixtures

Vibrational spectroscopic methods, mostly in combination with PXRD for comparison, have been utilised for the quantification of polymorphs where present in mixtures alone or within formulations and are summarised in Table 2. This is likely due to the rapid and non–invasive nature of the spectroscopic techniques whilst revealing specific bands or subtle changes associated with each polymorphic form. DSC and ssNMR methods have also been used though not to the extent of the previously mentioned methods.(129, 130) Quantification of polymorphic mixtures has been achieved using a range of analytical techniques including; solid state NMR (SS-NMR) (131), PXRD (132-140), spectroscopic methods including infra-red (120) (133, 141), near infra-red (120, 142-145), Terahertz and Raman (119, 120, 146-148) in combination with univariate and multivariate chemometric methods.

The analysis and successful quantitation of a polymorphic system is very much case dependent. This can be due to the API itself and which technique is optimal in terms of selectivity for characterisation of the polymorph. One must take into consideration the rate of transformation and how the sample presents itself for analysis. For example, monitoring a slow form transformation over time in a tablet matrix or rapid phase change in slurry formulations can aid the analyst in the appropriate techniques to begin investigation with – in the former example speed of measurement may not be an issue whereas for the latter some in–situ real time measurement may be of use. For some cases, PXRD out–performs spectroscopic methods as in the case of sulfamerazine where PXRD was the most accurate for determination of a sample, followed by DSC and then Raman (BRS).(130) It was noted by the authors that the two polymorphs were present in different crystal habits which would impact how well the samples could be mixed to homogeneity and how well the sample could be packed. This would have a two–fold effect on Raman measurements; non–representative spectra as the sampling volume would be as small as the laser spot diameter (typically ~300 μm) and the samples are not a perfectly homogenous mixture, and, large intensity differences due to difficulty ensuring the sample surface is flat.

Previous studies have highlighted possible sources of error associated with Raman spectroscopy and PXRD for the quantification of polymorph mixtures. (149, 150) Similar to the sulfamerazine case discussed above, such sources of error include sample preparation and wide particle size ranges of the polymorphs utilised which can be alleviated by careful sample packing, use of sample rotation to improve sample representativeness and use of sieves to ensure tighter particle sizing. (149, 151, 152)

TRS has recently been used to quantify ranitidine hydrochloride in binary polymorph mixtures with microcrystalline cellulose (MCC) in tablets and capsules compared directly to previously generated BRS and NIR quantitative studies by McGoverin *et al*. (90, 146, 153) It was reported that TRS outperformed all previously generated quantitative models, with more accurate PLS models yielded for tablets than capsules with RMSEVs of 4.80 and 2.40% for capsules and tablets respectively.

Table 2 Summary of polymorph quantification studies.

Compound	Year	Methods	Results	Reference
Benzimidazole	2005	FT–Raman	Quantification of 3 polymorphs varied between 5–10% of a 5% drug loading in a suspension–emulsion formulation.	De Spiegeleer *et al.* (147)
Bicafidene HCl	2005	ATR–IR, ATR–NIR, Raman and PXRD	Quantification of binary polymorph mixtures where NIR proved to be most accurate for quantitation	McArdle *et al.* (105)
Buspirone HCl	2006	FTIR and PXRD	FTIR and PXRD used for quantitation of binary polymorph mixtures.	Sheikhzadeh *et al.* (154)
Carbamazepine	2004	Raman	Raman analysis of binary polymorph mixtures with PCA provides a quantitation limit of < 2%.	Strachan *et al.* (155)
Casopitant mesylate	2011	Transmission PXRD and ss–NMR	Transmission PXRD and SS–NMR allow quantitative detection of alternate polymorph which by a range of preformulation tasks could prove to be non–CQA. Identification of alternate polymorphs in development candidate	Cimarosti *et al.* (129)
Clopidogrel bisulphate	2009	IR and Raman	Reported 1% LOD for both in combination with CLS, PCR and PLS for quantification of binary mixtures.	Nemet *et al.* (151)
Famotidine	2009	PXRD and BRS	BRS is more accurate and precise than PXRD for quantification of binary mixtures, spatial averaging improves sample representativity.	Nemet *et al.* (156)
Fluconazole	2011	NIR and PXRD	NIR and PXRD interchangeable for quantification of FII fluconazole in mixtures of FII and FIII.	Ziemons *et al.* (157)
Flufenamic acid	2010	TRS and BRS	TRS offers improved modelling of system with increase of percentage of variance for first loading in comparison to BRS; 98.09% and 89.7% respectively for binary mixtures.	Aina *et al.* (87)
Indomethacin	2003	NIR and PXRD	NIR found to offer lower SDs and higher correlation coefficient than PXRD. Both suitable for prediction of external samples of polymorphs in powder blends and tablets.	Otsuka *et al.* (158)
	2007	NIR and Raman	NIR more accurate for quantitation than BRS limited to a small extent by fluorescence of samples in ternary mixtures of solid state forms.	Heinz *et al.* (159)

Table 2 (continued) Summary of polymorph quantification studies.

Compound	Year	Methods	Results	Reference
Mannitol	2002	PXRD	Investigation of preferred orientation effects by PXRD of binary polymorph mixtures. Sample rotation and particle size reduction improved LOD and LOQ by half.	Roberts *et al.* (149)
	2002	BRS	Quantification by BRS improved when particle size was controlled and a rotating sample holder was employed for analysis of binary polymorph mixtures.	Roberts *et al.* (160)
Mebendazole	2010	DRIFTS and ANN modelling	Simultaneous quantification of three solid state forms by ANN modelling produced lower RMSEP values than PLS models.	Kachrimanis *et al.* (161)
Olanzapine	2007	PXRD	Quantification of binary polymorph mixtures by PXRD with LOD and LOQ of 0.40 and 1.22% w/w respectively.	Tiwari *et al.* (106)
Paracetamol	2002	FT–IR and Raman	Univariate analysis performed showing high correlation coefficients with both technique and a LOD of 1.2% of monoclinic form.	Al–Zoubi *et al.* (148)
	2007	FT–Raman	RMSEP of 054 % monoclinic form by PLS in combination with OSC pre-processing.	Kachrimanis *et al.* (162)
Ranitidine HCl	2000	Raman	Demonstrated monitoring of low content FII contaminant in tablets. No model built.	Taylor *et al.* (163)
	2002	BRS	PCA and quantitative models with a quantitation limit of less than 2% in binary polymorph mixtures of powdered tablets.	Pratiwi *et al.* (146)
	2006	NIR	BRS found to be more accurate for quantification of polymorphs in binary mixtures.	McGoverin *et al.* (153)
Ranitidine HCl	2009	PXRD and BRS	BRS provided better PLS models for quantification than PXRD for quantification of 3 solid state forms.	Chieng *et al.* (121)
	2012	BRS and TRS	Comparison of BRS to TRS for quantification of polymorphs in a spiked commercial formulation. More accurate PLS models yielded for tablets than capsules. RMSECV values of 2.40 and 4.80% respectively.	McGoverin *et al.* (90)

Table 2 (continued) Summary of polymorph quantification studies.

Compound	Year	Methods	Results	Reference
Risperidone	2007	IR, BRS and PXRD	IR and Raman incapable of identifying presence of form A in tablets despite lower detection limits reported, PXRD proved better suited for proving presence of polymorph in stability study.	Karabas *et al.* (164)
Sulfamerazine	2011	DSC, PXRD and BRS	DSC and PXRD more accurate than BRS for quantification of binary polymorph mixtures.	Tan *et al.* (130)
Sulfathiazole	2000	NIR	Binary polymorph mixtures quantified by NIR of FI in FIII sulfathiazole.	Luner *et al.* (165)
	2001	NIR	Binary polymorph mixtures quantified by NIR with a LOD of 0.3% API reported.	Patel *et al.* (166)
	2010	ATR–IR, NIR and BRS	NIR followed by BRS provided best models for quantification for analysis of ternary polymorph mixtures.	Hu *et al.* (120)
Undisclosed	2007	Raman	Raman mapping of undesired polymorphic form	Sasic *et al.* (167)
	2008	BRS, NIR and PXRD	BRS advantageous for quantification of amorphous form in blend and tablets.	Xie *et al.* (168)
	2012	Raman	Raman mapping of spiked formulation of two different polymorphs and an amorphate with contaminant levels of 0.025 to 0.1% w/w tablet.	Sasic *et al.* (169)

2.7.2 Quantification of active ingredients

High performance liquid chromatography (HPLC) is commonly used to determine the content uniformity of tablets and formulations with the capability to detect the presence of low levels of API. Highly specific methods can be produced by this technique for the quantification of API and its associated degradation products. The major drawback with HPLC is that it requires destructive sample preparation. HPLC can also require the use of large volumes of expensive solvents and is not considered to be a "green" technique. Spectroscopic methods such as NIR and Raman can be used for the quantification of APIs and their excipients within formulations with minimal sample preparation, with no use of solvents and by real–time measurements as exemplified by the studies reported in Table 3. The increased efficiency associated with spectroscopic methods due to the relative speed of analysis in comparison to HPLC and the capability of high sample throughput all aid the case for implementation of spectroscopic techniques, where appropriate, in pharmaceutical environments as exemplified by the examples in Table 3.

Several reports in the literature detail the generation of calibration sets based on laboratory samples and their potential and real application to the prediction of production samples.(170-175) In the case of NIR it is generally recommended to make use of transmittance over diffuse reflectance mode as a greater volume of the sample is probed.(176-178) Raman mapping has also been employed by Sasic *et al.* for the study of API distribution in Zanax tablets.(179) However there is a time penalty associated with performing mapping of statistical significance as described in their paper. In the case of Raman, BRS and TRS can provide great differences in their predictive ability due to the inherent sub–sampling issue associated with BRS and the lack thereof associated with TRS.

The popularity of TRS has increased significantly in the past decade, particularly for pharmaceutical analysis such as API quantification and excipients in pharmaceutical tablets and capsules, polymorphs in pharmaceutical formulations and calibration transfer.(84, 87, 180-182) Fransson *et al.* were able to develop simple lean

calibrations with few components/latent variables on pharmaceutical tablets composed of paracetamol with four excipients.(89) Johansson *et al.* compared the two geometry modes on pharmaceutical tablets and yielded an improved relative Root Mean Square Error for prediction (RMSEP) of API content of 2.2% with Transmission Raman as compared with 2.9% for Backscatter mode.(84) Hargreaves *et al.* have utilised Transmission Raman for quantitative analysis of pharmaceutical capsules achieving a relative RMSE for prediction of API concentration of 1.5%.(85) In this study API was quantified in capsule formulations of varying fill weights. By pre-processing the spectra to account for variations in the Raman signal intensity due to these varying fill weights the authors were able to develop a single PLS model to predict the active content across the entire fill weight range – 100–400 mg. Townshend *et al.* reported quantification by TRS and BRS of chlorpheniramine maleate content at 2% w/w level with marketed tablets.(92, 93) The author noted that accurate prediction of the API content by TRS could only be achieved by ensuring that the calibration tablets generated externally matched the photon propagation properties of the sample tablets. Additionally the effects of coloured capsule shells on prediction models of ambroxol in encapsulated formulations generated using TRS showed a slight decline in PLS prediction accuracy due to weak fluorescence of blue and green coloured capsules. (94)

Table 3 Recent API quantitation studies by spectroscopic methods.

Compound	Year	Methods	Results	Reference
Acetaminophen and caffeine anhydrate	2010	NIR – transmittance	Bilayer tablets containing each API. PLS models built for both API content determinations.	Ito *et al.* (178)
Acetaminophen, aspirin and caffeine – Excedrin and Vivarin	2012	Transmission FT–Raman	Tablet cores, increased representativeness of spectra due to increased sampling volume.	Pelletier *et al.* (183)
Alprazolam – Zanax	2007	Raman mapping	Use of PCA to evaluate API dispersion in low–level API tablets,(0.4 and 0.8% w/w)	Sasic *et al.* (179)
Ambroxol	2004	FT–Raman	For a 200 mg tablet, 29.6 mg of API was LOQ associated with Raman models.	Szostak *et al.* (184)
	2012	TRS	Capsules containing formulation did show a slight decline in PLS prediction accuracy due to weak fluorescence of blue and green coloured capsules.	Lee *et al.* (94)
Aminophylline	2008	Raman	Injection solution analysed where multivariate models were found to be more accurate than univariate models. Level of quantification matches pharmacoepeial method.	Mazurek *et al.* (185)
Atorvastatin Calcium	2009	Raman and UV	Powders and pellets of model formulations analysed with high correlation coefficients reported.	Mazurek *et al.* (172)
	2008	Raman, PXRD and IR	Raman had a LOD of 1 wt% in comparison to 3.33 and 6.66 wt% for PXRD and IR respectively.	Skorda *et al.* (186)
Bromazepam	2005	NIR and HPLC	Comparable results with HPLC reference method. 0.17 mg RMSEP reported for API quantitation.	Chalus *et al.* (187)

Table 3 (continued) Recent API quantitation studies by spectroscopic methods.

Compound	Year	Methods	Results	Reference
Caffeine anhydrate	2008	NIR – transmittance and reflectance	Tablets analysed using both modalities showed lower errors associated with transmittance.	Ito *et al.* (176)
Captopril	2006	Raman	RMESP values of API PLS models were 1.8–2.2% and 2.7–3.1%, Three commercial preparations of captopril containing 12.5mg and one 25mg of API per tablet were quantified using developed models.	Mazurek *et al.* (171)
Chlorpheniramine maleate	2012	TRS and BRS	MCC of differing particle sizes were incorporated into calibration samples. TRS was found to be sensitive to particle size differences. BRS and TRS results were in agreement with HPLC.	Townshend *et al.* (93)
Clonazapam	2005	NIR and HPLC	Comparable results with reference method. ~ 0.07 mg RMSEP	Chalus *et al.* (187)
Diltiazem HCl	2002	FT–Raman and HPLC	Comparable results between both techniques for experimental and commercial tablets.	Vergote *et al.* (170)
Diclofenac sodium	2008	Raman	Tablets and capsules analysed with RMSEP values in the range of 2.6 – 3.5 and 1.4–1.7 respectively.	Mazurek *et al.* (188)
	2006	Raman	Injection formulation with RMSEP from 0.4–2.4% API for PLS model	Mazurek *et al.* (185)
Diphenhydramine HCl	2006	FT–Raman and HPLC	Liquid formulation analysed and though a much lower LOD associated with HPLC, prediction errors similar between the two methods.	Orkoula *et al.* (189)
Ibuprofen	2008	NIR – transmittance	0–5% w/w API tablet formulations analysed and details the importance of choosing an appropriate calibration range for model development.	Alcala *et al.* (190)
	2010	NIR	Highlighted the effects of particle size, lacquer coating and compression in calibration development. RMSEPs of 1.1–1.5% API reported.	Blanco *et al.* (174)
Indapamide	2012	NIR and HPLC	2.08% w/w RMSEP reported for API quantification.	Porfire *et al.* (191)

Table 3 (continued) Recent API quantitation studies by spectroscopic methods.

Compound	Year	Methods	Results	Reference
Irbesartan and paracetamol separately	2011	NIR	Extended variable model incorporating physical characteristics of samples utilised for quantification of tablets containing irbesartan and paracetamol separately.	Blanco *et al.* (175)
Hydrochlorothiazide	2012	DR–NIR and HPLC	RMSEP of 1.7% API reported and found to be 15 times faster than HPLC method employed.	Ferriera *et al.* (192)
Metformin HCl	2012	NIR	Calibration model built using powder samples and applied to commercial samples.	Blanco *et al.*, (193)
Paracetamol	2010	TRS	PLS, CLS and MCR comparable in prediction performance; 2.4–3.4% API. Simple lean calibrations with few components were generated using TRS data.	Fransson *et al.* (89)
Potassium sodium dehydroandroandrographolide succinate	2011	DR NIR	Artificial neural networks produced RMSEPs of low values for both API and water content determination.	Li *et al.* (194)
Prednisolone	2006	Raman	RMSEP values of API PLS models generated were reported as 1.8–2.1% and 3.2–3.7% respectively.	Mazurek *et al.* (171)
Ranitidine HCl	2008	NIR and HPLC	RMSEP of 1.49% API reported as best model and NIR demonstrated to show good precision and reproducibility by authors.	Rosa *et al.* (195)
Risperidone	2008	FT–Raman	Coated and uncoated tablets analysed and with improved LODs for uncoated tablets.	Orkoula *et al.* (196)
Sulfathiazole and Sulanilamide	2008	Raman	Simultaneous determination of 2 APIs in powder mixtures to sub 4% API with highly reproducible measurements.	Lopez–Sanchez *et al.* (197)
Thiamine HCl	2012	Raman, DRIFT and ATR–IR	Raman and DRIFT comparable in terms of RMSEP values, 2.1 and 2.2% API.	Mazurek *et al.* (198)

Table 3 (continued) Recent API quantitation studies by spectroscopic methods.

Compound	Year	Methods	Results	Reference
Tianeptine	2011	NIR	Two independent validation sets used with RMSEP values of 2.0 and 2.7% API reported. The effect of model transfer to a different instrument investigated and RMSEP values increased – this was overcome by additional data processing.	Boiret *et al.* (199)
Unspecified	2007	TRS and BRS	PLS model RMSEP for API content within tablets of 2.2% and 2.9% for TRS and BRS respectively. Capsules have a RMSEP of ± 3.6%. Leaner calibration models can be built using 2 or 3 calibration spectra.	Johansson *et al.* (84)
	2008	NIR	Highlights time difference between HPLC analysis and NIR, 5 hrs to 12 mins. Comparison of 3 NIR instruments for determination of API.	Sulub *et al.* (200)
	2008	TRS	CLS and PLS models built where PLS reported a RMSEP of ± 1.2% with 5 s acquisition time	Eliasson *et al.* (86)
	2009	NIR and HPLC	Content uniformity of tablets with differing grades of excipients showed no effect on model prediction ability.	Li *et al.* (173)
	2009	NIR – transmittance	Content uniformity determination of 125 and 500 mg tablets with RMSEP values of 1.6 and 1.5% HPLC value respectively.	Xiang *et al.* (177)
	2010	NIR and HPLC	Two models of similar correlation coefficients produced and authors used accuracy profiling to determine each models' ability to quantify API over the chosen API range.	Mantanus *et al.* (201)
	2010	Raman	Family class assignment based on Raman and chemometric treatment	Roggo *et al.* (202)
	2011	TRS	RMSEP of 1.5% reported for API concentration. TRS insensitive to capsule fill weight, allowed for a model made from a batch at a single fill weight to be applied to batches of varying fill weights.	Hargreaves *et al.* (85)

3 Data analysis and chemometrics

3.1 Introduction

The analysis and monitoring of chemical systems and processes can result in large datasets as the case may be for quality assurance and reproducibility studies. Spectroscopy can be utilised for at, in and online analysis of processes for such studies and the spectral output is typically highly multivariate in nature. Spectra are often a result of not only the chemical response (pH, concentration) of the component of interest but further responses due to other components such as physical responses (particle size) or instrumental artefacts (noise).

Chemometrics can be utilised to extract useful information from complex datasets by simplifying data via the generation of mathematical expressions that can correlate differing responses into meaningful information which can allow for enhanced knowledge of the system. (203) According to the International Chemometrics Society, chemometrics is the science of relating measurements made on a chemical system or process to the state of the system via application of mathematical or statistical methods. It is considered by the FDA to be a PAT tool as listed in their Process Analytical Technology Initiative.(204) The aim of PAT is to increase process understanding, assure and build in quality throughout the manufacturing process (Quality by Design – QbD). (205, 206) The most commonly used chemometric methods include classification and regression. Classification methods such as principal component analysis (PCA) group samples together according to their spectral variations and correlate these changes with other variables. Regression methods such as multi–linear regression and partial least squares (PLS) link the spectra recorded to quantifiable properties of the sample.

3.2 Univariate & Multivariate Methods

Univariate calibration is typically useful for situations where the analyte of interest's concentration is the only factor on which the instrument response depends, e.g. the linear relationship between analyte concentration and absorbance in UV visible spectroscopy as described by the Beer–Lambert Law. In the case of complex spectra if one peak attributable to a single variable can be identified it can be useful for the monitoring of one variable, such as peak area changes due to change in concentration in the case of piracetam. (207) However in the majority of cases where multivariate spectral data is concerned, discrete changes of multiple variables are taking place. Multivariate calibration is capable of monitoring the changes of multiple variables in one step. It is useful where chemical or physical responses occur across a variety of spectral regions, allowing for simultaneous analysis of multiple variables in contrast to univariate methods where only one variable can be monitored at a time. Due to this and its coupling with pre-processing steps, discrete changes in spectral data across a wide spectral range can be used for quantitative or qualitative analyses.

3.3 Spectral data pre-processing

Pre–processing is commonly applied to data to enhance chemometric model performance by improving signal to noise ratios and/or removing interference effects that are not correlated to analyte changes. Examples of such interferences include shot noise, detector noise, fluorescence and baseline offsets. This can result in an improvement in errors associated with chemometric modelling as variable responses such as noise can be suppressed. Care must be taken when selecting suitable pre-processing methods; for it to be useful it must enhance chemically related information in the data while a poor pre-processing method can impair chemical information and generate spurious models. For Raman spectra sources of noise include; photon shot noise, sample–generated noise such as fluorescence, detector noise and externally–generated noise such as cosmic rays.(72, 208) Typically NIR spectra contain baseline offsets associated with the interaction of NIR radiation with the samples where the diffusion of light through a sample can be influenced by the

compression method used, particle size of the material and sample presentation to the instrument i.e. use of vials, direct placement on analysis interface, etc.(209, 210)

3.3.1 Normalisation

Normalisation is of particular use when pre-processing Raman spectroscopic data as there are inherent intensity differences in the spectra due to power fluctuations of the laser source throughout data collection. There are multiple means of how one can normalise spectral data, the most common is that of normalising the spectrum to a constant area of a specified band which will act to remove the fluctuating signal's effect.(211)

3.3.2 Multiplicative Scattering Correction

Multiplicative Scattering Correction (MSC) is a pre-processing method which is a variant of normalisation that corrects for differences in baseline offsets and scattering variations which are often due to particle–size distributions and the interaction of light with the solids.(209) It does this by first calculating a reference spectrum which is the average of all spectra in the dataset. For MSC a linear regression of each spectrum against the reference spectrum is made. The least squares coefficients of the linear regressions are determined and are then used to calculate the MSC–corrected spectrum.

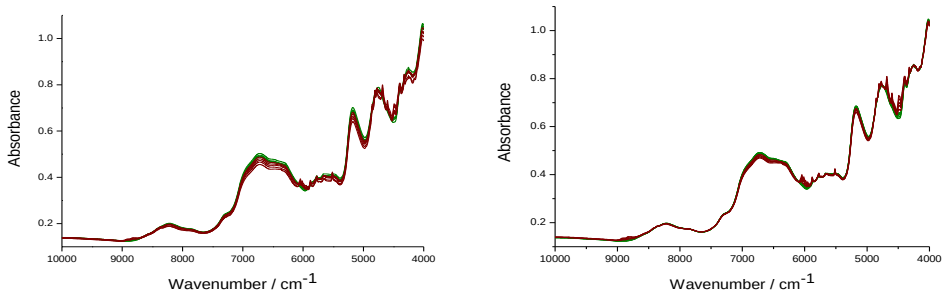

Figure 17 NIR spectra of tablets containing mostly MCC. Left, raw NIR spectra exhibiting small baseline offsets. Right, MSC treated NIR spectra. (Piracetam tablet spectra)

3.3.3 Standard Normal Variate

Standard Normal Variate (SNV) is a normalisation variant similar to MSC where it is used to correct for baseline offsets and scattering variations in spectra. In SNV the mean of each spectrum is subtracted and then divided by the standard deviation. It produces very similar results to MSC.

3.3.4 Derivatives

Derivatives are often used to remove offset and background slope variations between spectra and enhance spectral differences. First derivatives remove baseline offset variations from spectra while second derivatives can remove both baseline offset variations and differences in baseline slopes between spectra. First derivatives provide the slope at each point of the original spectrum and have peaks where the original spectrum has maximum slope and crosses zero where the raw spectrum had peaks. Second derivatives measure curvature at each point in the original spectra and are more similar to the non–processed spectrum as peaks are approximately in the same place however with a reverse configuration i.e. where a band has high intensity in the original spectrum, the band will have a large negative intensity post second derivatisation.

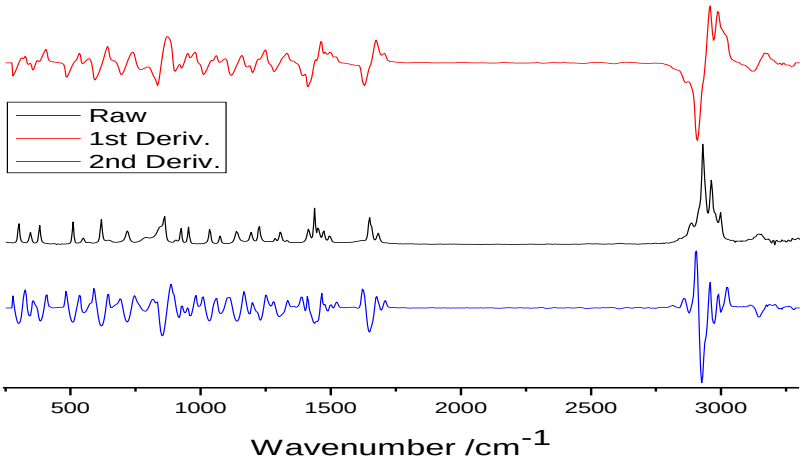

Figure 18 Raman spectra of FIII piracetam. Top, first derivative spectrum. Middle, raw spectrum. Bottom, second derivative spectrum.

A commonly used derivatisation method is the Savtizky Golay filter which is used for smoothing and derivation.(212) It is a polynomial smoothing function that

analyses the spectra and estimates the smoothing derivation for each point separately. There are 3 parameters to be considered when using this filter; degree of derivative sought, number of points to be used in the smoothing and the polynomial order of the smoothing function. As the degree of derivation increases, the signal to noise ratio decreases as the amount of signal is reduced.(213-215) This is particularly true when few points are used in the smoothing and/or a high polynomial order is used for the smoothing function. Derivatives can also be used to compensate for the effects of minor fluorescence where present in a Raman spectrum.

3.3.5 Mean centering

Mean centering is used to centre the data relative to the mean of the data set to emphasize differences in the spectral features of the dataset. It is performed by calculating the average data vector of all n rows in a dataset and subtracting it point by point from each vector in the dataset.(211)

3.4 Chemometric methods of analysis

There are a variety of chemometric methods which can be employed for multivariate analysis. Known system responses, such as concentration of API present, can be modelled with spectral data to build models for quantification. In this thesis PCA was mainly used for determination of powder blend homogeneity prior to preparation of tablets. PLS was used to build quantitative models of API concentration and polymorph contamination in model formulations.

3.4.1 Principal component analysis

PCA a qualitative exploratory tool where the data matrix is decomposed into a number of principal components (PCs) that maximise the explained variance in the data on each successive component under the constraint of being orthogonal to the previous PCs.(216, 217)

$$X = TP' + E$$

X is a M × N matrix where M corresponds to samples with N measured variables. T is a M × A matrix and P^t is an A × N matrix where A is the number of calculated PCs. T and P are vectors. E is a M × N matrix containing the PCA model residuals, i.e. variance unexplained by the PCs.

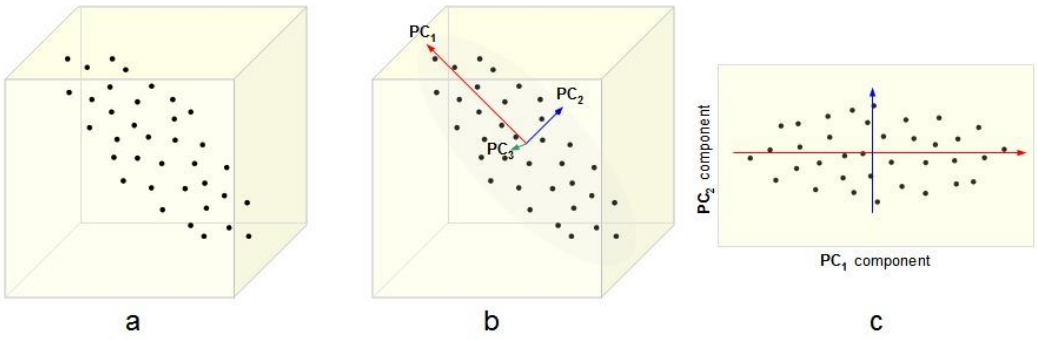

Figure 19 An illustration of PCA; a). A typical dataset; b) 3 orthogonal principal components for the data, ordered by variance; and c) the scores plot of the data set into the first two components.

The first PC explains as much of the variation in the data as possible. The second PC is orthogonal to the first and describes as much of the remaining variation as possible, and so on. Plotting the PCs results in a scores plot which can be used for the interpretation of the PCA model and the samples which were analysed. Score plots can reveal patterns or trends in the data; for example, in the case of counterfeit pharmaceuticals where counterfeit and genuine article pharmaceutical tablet spectra cluster together separately allowing for identification and even knowledge of counterfeit origin.(218, 219) An illustrative example is the use of NIR by Hu *et al.* to show the clustering of crystallised samples based on relative humidity in Fig. 20.(220) The samples were composed of a mixture of the FI polymorph and amorphate of sulfathiazole that had been prepared by milling FII for 120 mins prior to placement at a number of different % RH conditions ranging from 10 to 98% RH. The greatest differences arose across PC1 which represents the recrystallisation of the mixtures to alternate polymorphs, FII, FIII and FIV. At 10% RH the amorphous content of the mixture converted to FI. At higher relative humidities the mixtures converted to FII and mixtures of FIII and FIV. This could be seen spectrally at 6880 cm^{-1} where peak intensity decreases as a result of diminishing amorphate content.

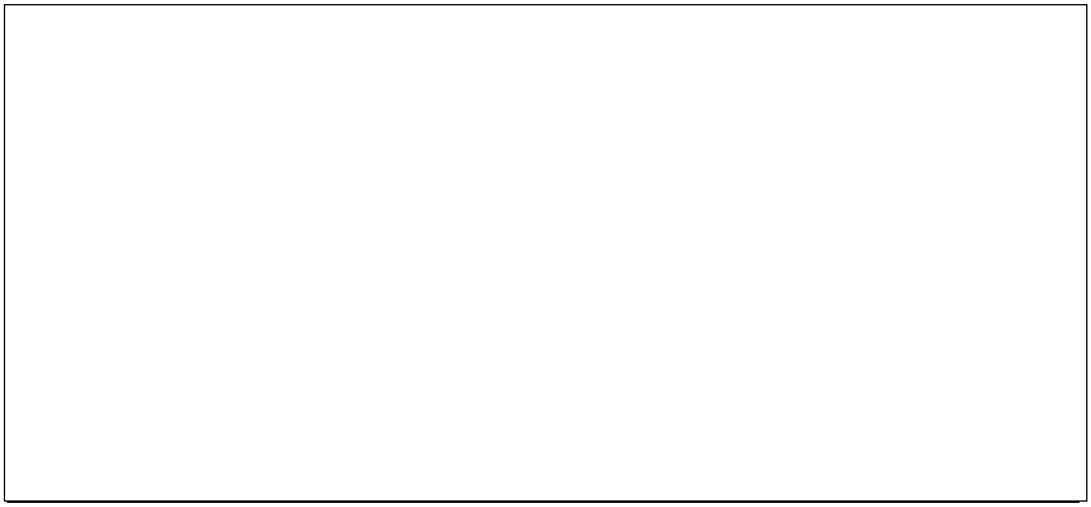

Figure 20 a) PCA scores plot of the NIR spectra of milled samples stored at different humidity conditions. b) NIR spectra of milled FII samples stored (1) at 10% RH for 28 days; (2) at 43% RH for 14 days; (3) at 43% RH for 28 days; (4) at 43% RH for 56 days; (5) at 75% RH for 14 days; (6) at 98% RH for 14 days. Reproduced from Hu *et al.(220)*

3.4.2 Partial Least Squares

Partial Least Squares (PLS) is used to develop regression models that formulate linear relationships between variables and properties of interest i.e. spectral data with analyte concentrations.(221, 222) It attempts to find factors which both capture variance and achieve correlation between these different information sets. The matrices of both the variables (X) and the property of interest (Y) are decomposed to generate a matrix of scores and loadings for both information sets where T and U correspond to the matrix of scores, P' and C' represent the loadings, and E and F signify the residuals for each respective information set as follows;

$$X = TP' + E$$

$$Y = UC' + F$$

PLS aims to model all these components for X and Y such that both sets of residuals are approximately equal to zero. Residuals are the differences between the actual and predicted values of a dependent variable. A relationship between each set of scores is generated where orthogonal variables are calculated leading to reduced dimensionality. This can be further improved upon by using further iterations to increase covariance between the two information sets.

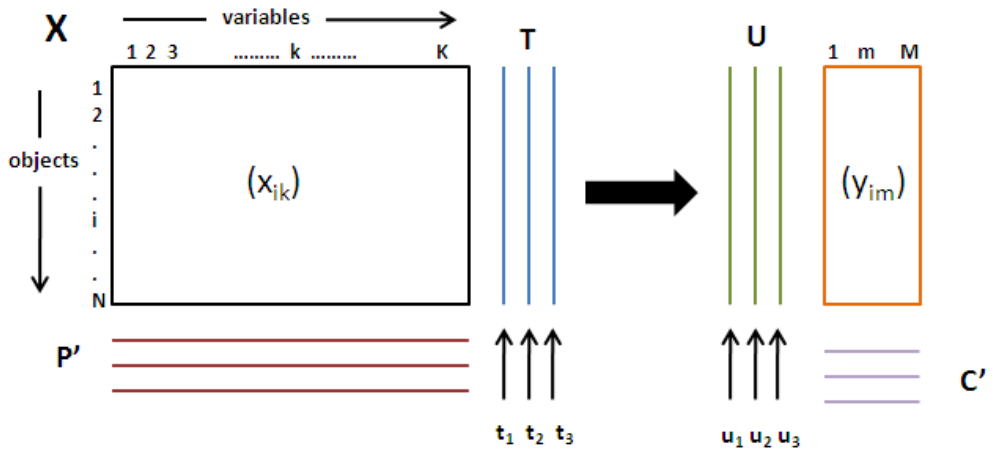

Figure 21 Graphical description of PLS regression. Adapted from Kourti *et al.* (205)

There are multiple PLS methods in use currently however the focus of all work in this thesis will focus on PLS1. This PLS method consists of generation of separate calibration models built for each column in Y. A calibration set of samples are prepared, analysed and the data is used to build the calibration model. A further set of samples called the prediction set are used to test the calibration model.

3.5 Model evaluation

In chemometric modelling, hundreds of calibration models can be generated in a relatively short time. Selection of the optimal model requires systematic evaluation of models based on characteristics common to all. The performance of the calibration models can be evaluated using the correlation coefficient and the root mean square error (RMSE) as defined by the following equation;

$$RMSE = \sqrt{\sum_{i=1}^{n} \frac{(y_i - \hat{y}_i)^2}{n}}$$

where y_i is the reference value, $\hat{y}_i$ is the calculated value and n is the number of samples.(211) RMSE is termed as the root mean square error of calibration (RMSEC) for the calibration set, the root mean square error of cross validation of the calibration set (RMSECV) and the root mean square error of prediction (RMSEP) for the prediction set. The correlation coefficient, R^2, is a measure of the linearity of the

data and the closer this value approaches 1, the better the fit of the measured Y vs. predicted Y. The RMSECV is derived using a leave–one–out cross validation procedure which iteratively selects a sample from the dataset and uses this sample for prediction by a calibration model built by the remaining unselected samples. This is an approximation of the error linked to prediction of samples. RMSEP is used to test the error associated with the calibration model for the prediction of samples new to or unseen by the calibration model. This is the real test of the model by observing the errors associated by measuring new samples and using the established calibration model to predict for these new samples.

3.6 Limits of detection and quantification

The limit of detection (LOD) refers to a qualitative measurement where the lowest concentration of a substance can be detected with reasonable certainty by an analytical technique.(90, 211) The limit of quantification (LOQ) signifies the level at which an acceptable quantitative analysis can be made.(211) The LOD and LOQ for each correlation were calculated using the equations below, which were based on the standard deviation of the response and the slope, where the standard deviation (SD) of three measurements of a sample and the slope (m) of the calibration plot of a PLS model was used.(223)

$$LOD = \frac{3STD}{m}$$

$$LOQ = \frac{10STD}{m}$$

3.7 Mean square of differences

Mean square of differences, was used to determine homogeneity where a spectra from different time points of mixing is subtracted from the spectra preceding it and the difference is squared and normalised and plotted against mixing time.(224) This is given by;

$$S^2 = \frac{\sum_{i=1}^{m}(A_i^{t_1} - A_i^{t_0})^2}{m}$$

where $A_i^{t_1}$ is the absorbance at each wavelength i for the spectrum measured at a given time t_i and $A_i^{t_0}$ is the absorbance at the same wavelength for the spectrum recorded at the preceding time t_0. Subtracting the two terms from each other and squaring the difference results in the mean square of differences. The closer the difference is to zero, the more similar the spectra are and once this value oscillates closely to a minimum the mixture can be assumed to be homogeneous.

4 Experimental Chapter

4.1 Materials

4.1.1 Tablet preparation

Powder mixtures of the desired components were first prepared in 2 g quantities and mixed until homogeneous. Such quantities were used so as to ensure that the mixing vials were at least half filled to minimise weighing errors and that the vials would have sufficient fill volume to allow for NIR analysis. Homogeneity was determined by analysis of the powders using NIR at 30 second intervals between mixing using a Vortex mixer. Analysis using Mean Squares of Differences (MSD) was used to assess homogeneity. A spectrum from different time points of mixing was subtracted from the spectrum immediately preceding it and the difference was squared and normalised and plotted against mixing time as per Blanco *et al.*(224) The closer the MSD value was to zero the more similar the spectra, thus this acted as an indicator of homogeneity. PCA was also used to visualise spectral similarity and supported the MSD results.

Using the homogeneous powder blends, each tablet was prepared by hand–filling into a standard IR die hydraulic press (Perkin Elmer) with a 13 mm die set and a compression of 253 kPa was employed. All tablets were prepared in triplicate. After each tablet was produced 5 measurements of thickness were collected per tablet using digital callipers. The mean and standard deviation of each replicate set containing 10 tablets, totalling 30 tablets per thickness, was calculated. The % error reported with each is the result of dividing the standard deviation by the mean for each tablet thickness and multiplication by 100 to express as a percentage. The following sub–sections detail the tablets prepared for each experiment.

4.1.1.1 ROY tablets

Tablets used for Chapter 5 consisted of 5–methyl–2–[(2–nitro phenyl) amino] 3–thiophenecarbonitrile (ROY) as the model active ingredient in an excipient matrix of microcrystalline cellulose (MCC) and magnesium stearate (MgSt). Powder blends were prepared as outlined by the general methodology above and both PCA and MSD plots are presented in Fig. 22. PCA was used on spectra that were pre-processed using a combination of MSC and a 2nd derivative.

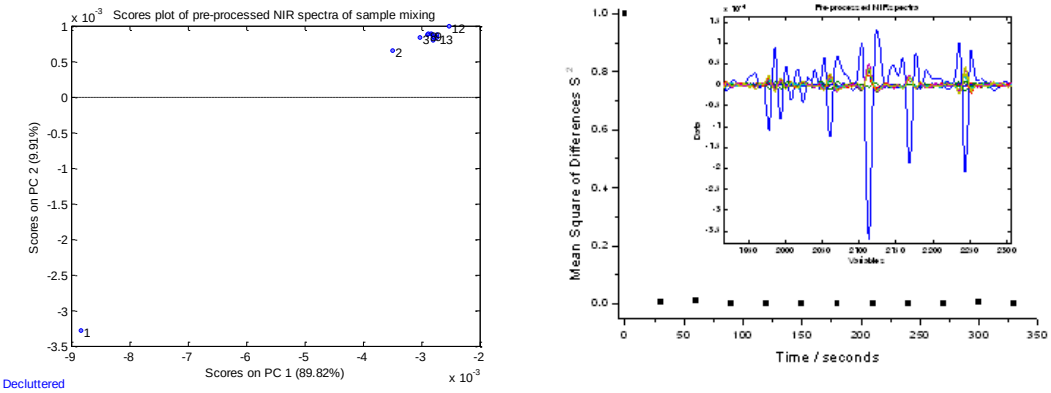

Figure 22 Left, PCA scores plot of NIR spectra from mixing experiment, number refers to order in which spectra were collected, and right; NIR spectra pre-processed using MSC and a 2nd derivative with a mean squares of differences plot inset.

Sample 1 (large blue spectrum in Fig. 22) is from time zero with no mixing, with all subsequent measurements collected after 30 seconds of mixing. As PCA demonstrates, the time zero spectrum is distinct from the main grouping of samples where even after 30 seconds, there was some level of mixing achieved. Variation is greatly reduced amongst the main grouping and this is supported by the MSD plot. The mean square was initially very high as to be expected with the time zero sample but then dropped to ~zero, the values then fluctuated narrowly around the zero value as the mixing time progressed. Both PCA and MSD confirmed that the powder mixtures where sufficiently homogenous for subsequent tablet production.

Tablets of different thicknesses (0.75, 1.00, 1.25 and 1.50 mm) were prepared with ten different ROY concentrations, entire compositions are detailed below (Table 4). Each tablet, at each concentration, and thickness were prepared in triplicate, resulting in 120 tablets in total. These tablets served as the calibration set. Four separate

tablets at the concentrations of 4, 6, 9 and 14% at four different thicknesses were prepared in an identical manner and used as the validation set.

Table 4 Composition of model ROY tablets in % w/w.

	Concentration (% Weight)		
Calibration Samples	**% ROY**	**% MCC**	**% MgSt**
1	1.0	95.0	4.0
2	2.0	94.0	4.0
3	3.0	93.0	4.0
4	4.0	92.0	4.0
5	5.0	91.0	4.0
6	7.5	88.5	4.0
7	10.0	86.0	4.0
8	12.5	83.5	4.0
9	15.0	81.0	4.0
10	17.5	78.5	4.0
	Concentration (% Weight)		
Validation Samples	**% ROY**	**% MCC**	**% MgSt**
P4	4.0	92.0	4.0
P6	6.0	90.0	4.0
P9	9.0	87.0	4.0
P14	14.0	82.0	4.0

After each tablet was manufactured, the variation associated with thickness was assessed. The variation in tablet thickness was low, with a maximum % error of 1.1% for the 0.75 mm, 0.5% for the 1 mm, 0.45% for the 1.25 mm and 0.57% for the 1.5 mm tablets as shown in Table 5 below.

Table 5 Thickness data collected using digital callipers from ROY tablets.

	0.75 mm		1 mm		1.25 mm		1.5 mm	
Replicate	**Mean**	**STD**	**Mean**	**STD**	**Mean**	**STD**	**Mean**	**STD**
A	0.775	0.010	1.002	0.005	1.265	0.004	1.520	0.005
B	0.788	0.008	1.005	0.005	1.264	0.005	1.519	0.009
C	0.782	0.008	1.005	0.005	1.232	0.008	1.491	0.012
Avg Mean	0.782		1.004		1.254		1.51	
Avg STD	0.007		0.005		0.006		0.009	
% Error	1.096		0.505		0.446		0.565	

4.1.1.2 Piracetam contaminant tablets

4.1.1.2.1 Preparation of polymorphs

Piracetam (FIII polymorph form purity confirmed by DSC and PXRD) was supplied by Sigma Aldrich and used as received. The FII polymorph was prepared by first generating the FI polymorph by heating the FIII (previously ground roughly using an agate pestle and mortar for 1 minute to decrease particle size) to 140°C in an oven for 72 hours. The FII form was then formed from the unstable FI form at room temperature over four days with the conversion process monitored by Raman spectroscopy, spectra and their discussion presented in Chapter 8.(225, 226)

4.1.1.2.2 Preparation of contaminant tablets

Preparation of tablets containing piracetam (mixtures of FII and FIII) as an active ingredient with calcium carbonate ($CaCO_3$) and microcrystalline cellulose (MCC) as excipients were mixed in a 10:10:80 ratio by weight. The piracetam component (10% by weight) comprised of mixtures of FII and FIII which varied from 0.1:99.9% FII:FIII to 99.9:0.1% FII:FIII (Table 6).

Table 6 Composition of piracetam polymorph contaminant tablets in % w/w.

Calibration Samples	% FII	% FIII
FIII100	0	10.0
FII01	0.1	9.9
FII02	0.2	9.8
FII04	0.4	9.6
FII08	0.8	9.2
FII10	1.0	9.0
FII20	2.0	8.0
FII50	5.0	5.0
FII80	8.0	2.0
FII90	9.0	1.0
FII92	9.2	0.8
FII96	9.6	0.4
FII98	9.8	0.2
FII99	9.9	0.1
FII100	10.0	0
Validation Samples	**% FII**	**% FIII**
FII04	0.4	9.6
FII10	1.0	9.0
FII90	9.0	1.0
FII92	9.2	0.8

To ensure that the powder mixtures were homogeneously mixed prior to tablet manufacture, NIR was used to monitor homogeneity at 30 second time points throughout mixing. Spectra were pre-processed using MSC and a second derivative.

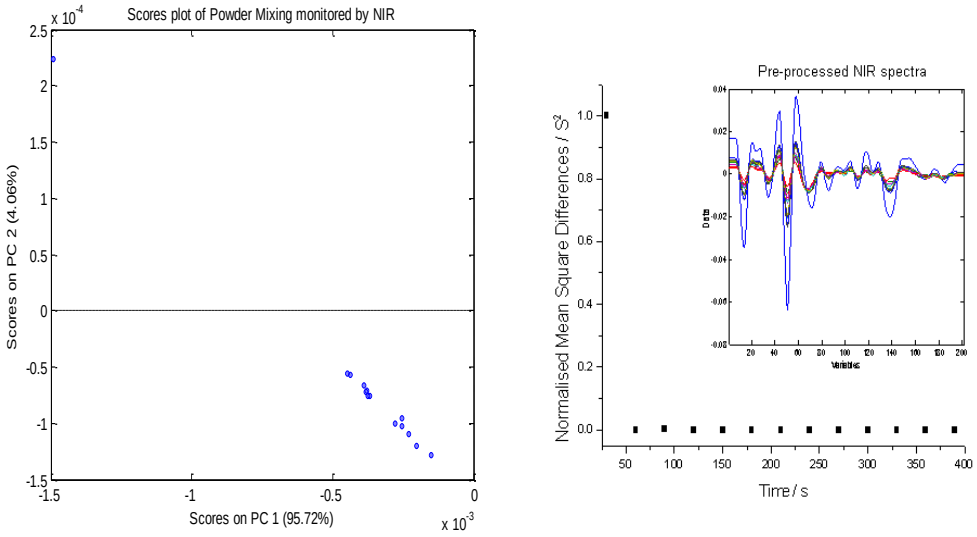

Figure 23 Left, PCA scores plot of NIR spectra from mixing experiment, and right; NIR spectra pre-processed using MSC and a 2nd derivative with mean squares of differences plot.

The resulting spectra were used for PCA and the scores plot is shown in Fig. 23. Sample 1 (large blue spectrum in Fig. 23 right) is from time zero with no mixing, with all subsequent measurements collected after 30 seconds of mixing by using a Vortex Mixer. The mixing profiles seen here match that of the ROY powder blends where the initial time zero spectrum was vastly different to all subsequent spectra as mixing progressed. All subsequent spectra after 30 seconds of mixing were highly similar as demonstrated by their close clustering in the PCA plot above and their low MSD values close to zero indicating that the powder blends were well mixed in preparation of compression.

Table 7 Measurement of thickness of the piracetam tablets and associated errors with the reproduction of tablets.

	1 mm Tablets		2 mm Tablets		3 mm Tablets	
Replicate	**Mean**	**STD**	**Mean**	**STD**	**Mean**	**STD**
A	0.982	0.007	1.969	0.008	2.938	0.005
B	0.997	0.006	1.977	0.004	2.987	0.007
C	0.993	0.011	1.968	0.005	2.987	0.007
AVG Mean	0.991		1.971		2.971	
AVG STD	0.008		0.006		0.006	
% Error	0.813		0.297		0.211	

After the tablets were manufactured the thickness of each tablet was measured as previously detailed in Section 4.1.1.1. The variation in tablet thickness was low, with

a maximum % error of 0.8% for the 1 mm, 0.3% for the 2 mm and 0.21% for the 3 mm tablets as shown in Table 7 above.

4.2 Analytical techniques

4.2.1 Backscatter Raman spectroscopy

BRS data were collected at room temperature using a RamanStation spectrometer (AVALON Instruments Ltd., Belfast, Northern Ireland; now PerkinElmer) with 785 nm laser diode excitation with a spot size of ~ 200 μm in diameter, a cooled (–77 ºC) CCD detector and a motorised XYZ stage. Spectra were acquired from 250–3310 cm^{-1}. Tablets were analysed using a custom made multi–tablet holder plate. Powders were placed in aluminium crucibles (Thorn Scientific Services Ltd, UK) of 2 mm depth and 5 mm diameter. In all cases a sampling grid employing 0.5 mm spacing was used to minimize spectral variance and reduce sub–sampling effects. The spectra collected were then averaged for subsequent data analysis. Table 8 details the acquisition parameters and instrument settings used for all analyses.

Table 8 Conditions employed for backscatter Raman analyses.

Experiment	Resolution / cm^{-1}	Laser power / mW	Acquisition parameters	Grid size
ROY tablets	4	55.9	2 seconds × 8	3 × 3
Piracetam binary mixtures	4	79.9	2 seconds × 10	3 × 3
PiraTabs	4	79.9	2 seconds × 10	4 × 4
PiraConversion	2	79.9	2 seconds × 10	4 × 4

4.2.2 Transmission Raman spectroscopy

TRS data were collected using a Cobalt Light Systems Ltd. TRS100 Transmission Raman Optical Engine at an excitation wavelength of 830 nm and a laser power of 0.65 W. Tablets were arranged on a multi–tablet holder plate for analysis. Powders were measured by placing in polyethylene bags and placement on a custom plate for analysis. A spot size of 8 mm was used and spectra were collected at a resolution of 7 cm^{-1} from 50 to 2400 cm^{-1}. Acquisition parameters and instrument settings used for all analyses are detailed in Table 9.

Table 9 Conditions employed for transmission Raman analyses.

Experiment	Resolution / cm^{-1}	Laser power / W	Acquisition parameters
ROY tablets	7	0.65	0.1 seconds × 50
PiraTabs	7	0.65	0.2 seconds × 32

4.2.3 Near infra-red spectroscopy

NIR reflectance spectra were collected using a Perkin Elmer NTS ATR–FT–NIR fitted with an NIR reflectance attachment at a resolution of 4 cm^{-1} from 10000 to 4000 cm^{-1} with 32 co–added scans per spectrum. Interleaved scanning mode was used for collection of all spectra which allows for a ratio of the sample spectrum against a background that is recorded almost simultaneously, eliminating residual atmospheric absorptions for the final spectrum. Three spectra of each tablet was collected after rotating the tablet 120° on the sampling mount and these spectra were averaged for subsequent data analysis. For powders, sample vials were shaken and repositioned between triplicate measurements of each sample. Details of parameters used for analyses are detailed in Table 10.

Table 10 Conditions employed NIR analyses.

Experiment	Resolution / cm^{-1}	Acquisition parameters	Accessory
ROY powder blends	4	32	Reflectance
ROY tablets	4	32	Reflectance
Piracetam binary mixtures	8	32	Reflectance
PiraTabs blend	8	32	Reflectance
PiraTabs	8	32	Reflectance
PiraTabs	4	32	Transmittance

4.2.4 Powder X-ray diffraction

PXRD data of the ROY tablets and piracetam polymorphs generated, were collected using an Inel Equinox 3000 (Artenay, France) powder diffractometer equipped with a CPS180 fixed curved multi–channel detector. Diffraction patterns were collected for 16 minutes with the X–Ray generator operating at 35 kV with a 25 mA current. Samples were held in dedicated aluminium sample holders, fabricated in–house for each tablet thickness. Each sample was spun at a rate of 5 revolutions per minute during data collection and analysed in triplicate. The individual patterns were then averaged to provide a single powder pattern for each sample.

4.2.5 Differential scanning calorimetry

Differential Scanning Calorimetry (DSC) was performed on a Rheometric Scientific STA625 with a heating rate of 10 °Cmin^{-1} used for piracetam polymorph samples by Dermot McGrath, Chief Technical Officer, School of Chemistry, NUI Galway.

4.3 Data analysis

All multivariate data analysis was carried out using The Unscrambler software version 8 (Camo, Norway) and the PLS toolbox (Eigenvector) running on Matlab version 8 (Mathworks). A variety of several pre-processing methods were assessed for each analytical method and these included baseline correction, 1^{st} order and 2^{nd} order Savtizky–Golay derivatives, standard normal variate (SNV) and multiplicative scattering correction (MSC).(209, 227, 228) Principal Component Analysis (PCA) was used for qualitative analysis and standard Partial Least Squares (PLS) regression was used for quantitative modelling.(216, 229) The performance of the various PLS calibration models generated from data employing the different pre-processing methods was evaluated using the correlation coefficient and various root mean square error (RMSE).(211) The optimal number of PLS factors was determined by using a leave–one–out cross validation procedure.

For PXRD data of the piracetam binary polymorph mixtures, X'Pert HighScore Plus software (PANalytical) was used to calculate peak height intensity and area, and for correction of the shifts along the 2θ axis for PXRD scans. The cubic spline data interpolation technique was then used to reconstruct the PXRD scans. The PXRD and spectroscopic data were subjected to mean centring prior to partial least squares (PLS) analysis.

5 Comprehensive analysis of a model pharmaceutical tablet system incorporating ROY by the use of Raman, transmission Raman, and near infra-red spectroscopies and powder X-ray diffraction

5.1 Introduction

APIs are frequently delivered to the patient in their solid form by inclusion in tablets, capsules or as powders. A common issue associated with solid formulations is the need to accurately quantify the precise concentration of API loading. This is required for good manufacturing practices (GMP) and it is also desirable that one uses a method that is accurate, non–contact and non–destructive. This last point is important as HPLC, one of the most widely used analytical methods for API quantification, requires the samples to be destroyed and made up into solutions for analysis which can be costly in terms of time and solvents required. Spectroscopic methods provide a useful solution to these issues as they are amenable to fiber optic coupling, are non–destructive and rapid.

Here, we quantitatively assess the efficacy of several rapid characterisation methods (Backscatter and Transmission Raman spectroscopies and NIR spectroscopy) and PXRD in combination with chemometric methods for the quantitative analysis of an API in model tablets. The aim of this study is to compare and contrast the methods for a system with a range of API concentration from 1% to 17.5% by weight of the system which comprises of a model API, 5–methyl–2–[(2–nitrophenyl) amino]–3–thiophenecarbonitrile (ROY), with several excipients (*e.g.* microcrystalline cellulose and magnesium stearate). Tablets were manufactured with four different tablet thicknesses; 750, 1000, 1250 and 1500 μm. The data was then used to develop a range of calibration models for predicting ROY concentration with the best accuracy of ~0.3% API RMSEP being achieved with NIR and TRS.

5.2 Qualitative analysis

5.2.1 Powder X-ray diffraction

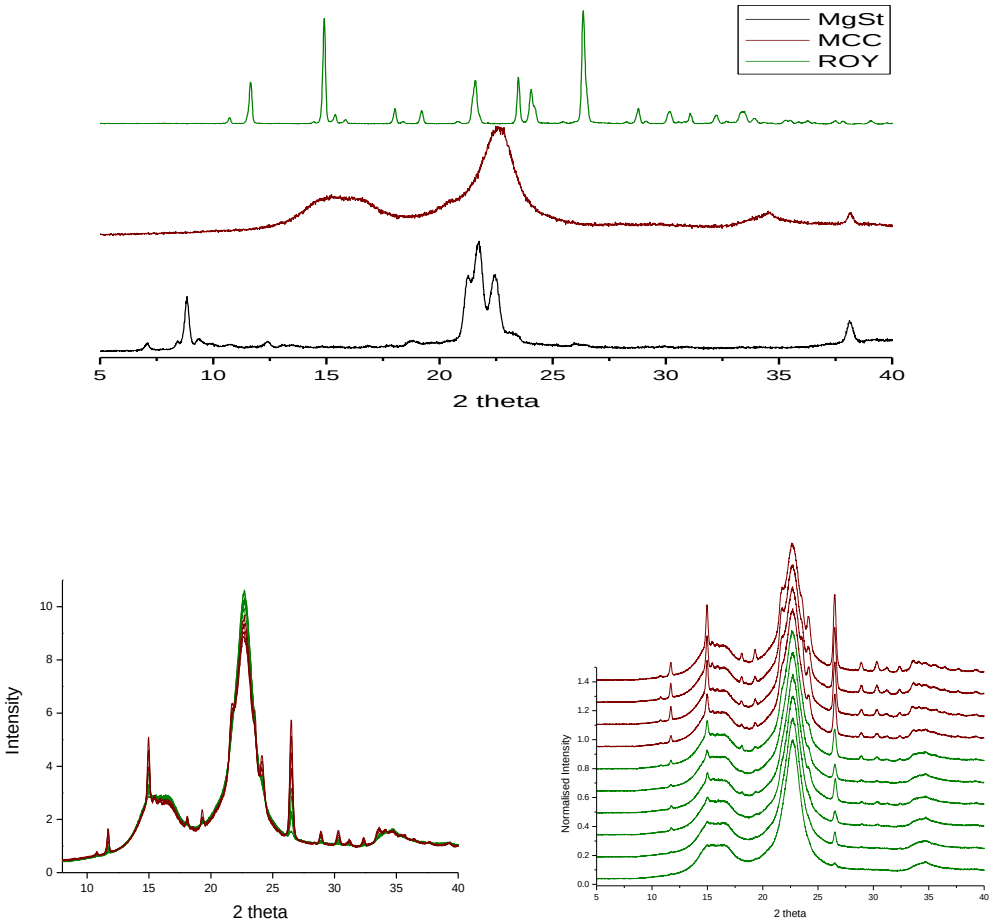

Figure 24 PXRD analysis of ROY, MCC and MgSt tablets; (top) raw PXRD diffraction patterns, (bottom) data reduced and mean normalised PXRD patterns of tablets where the green to red transition is due to increasing ROY content.

Fig. 24 shows the PXRD pattern of the components and their tablets from 10 to 40 2θ as this region contained the most information regarding the tablets as the majority of features to all tablet components were present in this region. In the tablet diffraction patterns, the three most intense peaks, 15.5 and 26.5 2θ, due to contributions from ROY, and the main broad band at 22.72 2θ, due to an overlap of bands of MgSt, MCC and ROY respectively as shown by the pure component patterns presented above. There is a linear change at these bands as the quantity of ROY decreases and the quantity of MCC increases in the tablets. Peaks attributable to ROY are evident

across the tablet patterns at 11, 15.2, 18, 19.2, 24.2, 26.5 and 30.5 2θ and grow in intensity as the concentration of ROY increases across the tablets manufactured.

5.2.2 Near infra-red spectroscopy

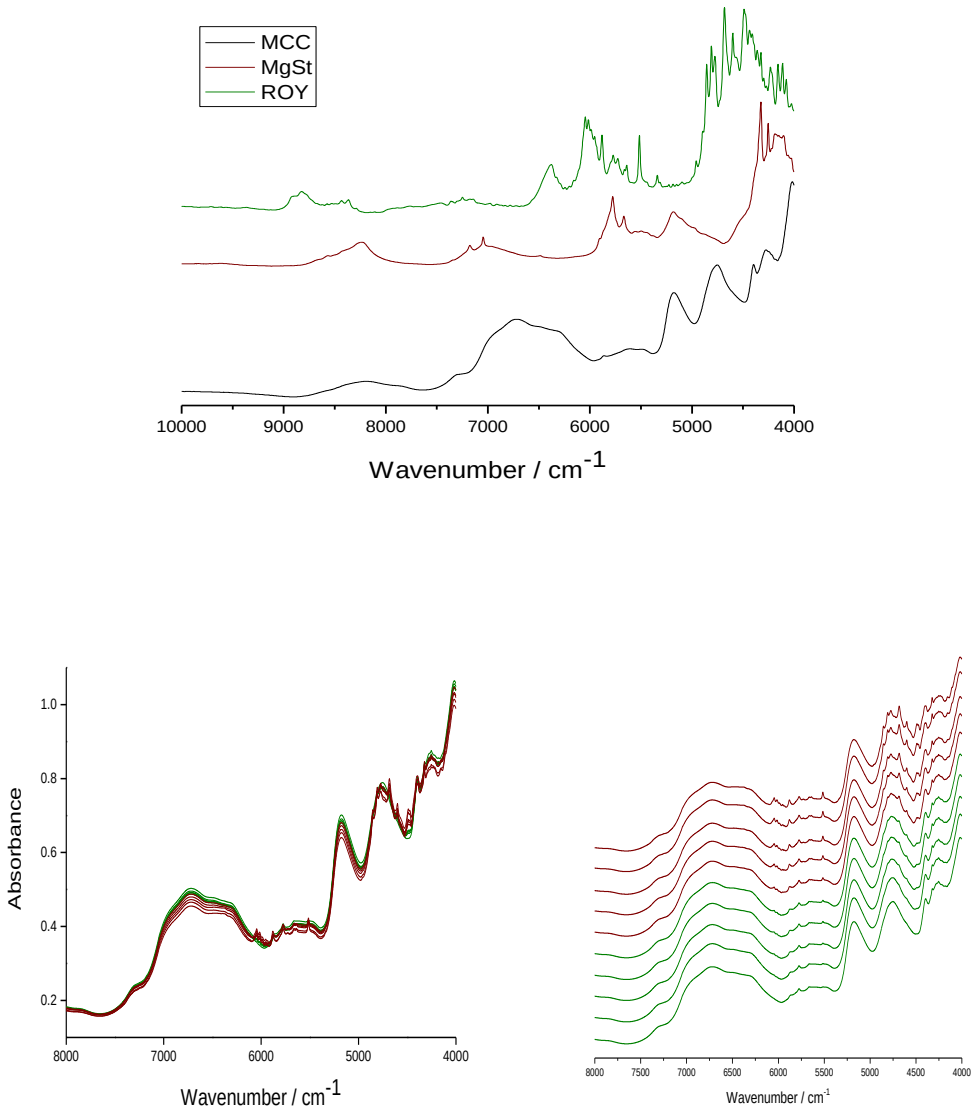

Figure 25 (top) raw NIR spectra of tablet components, (bottom) NIR spectra of the tablets overlaid and separated where the green to red transition is due to increasing ROY content.

The NIR spectrum of ROY exhibits many features, most notably around the 6000 – 4000 cm^{-1} spectral region which are due to CH and CH_2 combinations and around 5000 cm^{-1} bands associated with the primary amide and cyano moieties within the molecule. MgSt features a sharp band at 7045 cm^{-1} due to the carboxylate

functionality of stearate and a broad band at 5185 cm^{-1} in its spectrum.(230) The NIR spectrum of microcrystalline cellulose displays a large broad peak at 6800 cm^{-1} and several broad peaks in the 5300–4000 cm^{-1} region due to CH and CH_2 overtones.(230) The NIR spectra of the tablets strongly feature MCC characteristics which are as expected since it is the main tablet constituent. There are also scattering variations and baseline offsets due to the interaction of light with the tablets evident in the raw spectra. There are small peaks observable due to ROY present in the 6200–5300 cm^{-1} and 5000–4000 cm^{-1} spectral regions.

5.2.3 Raman spectroscopy

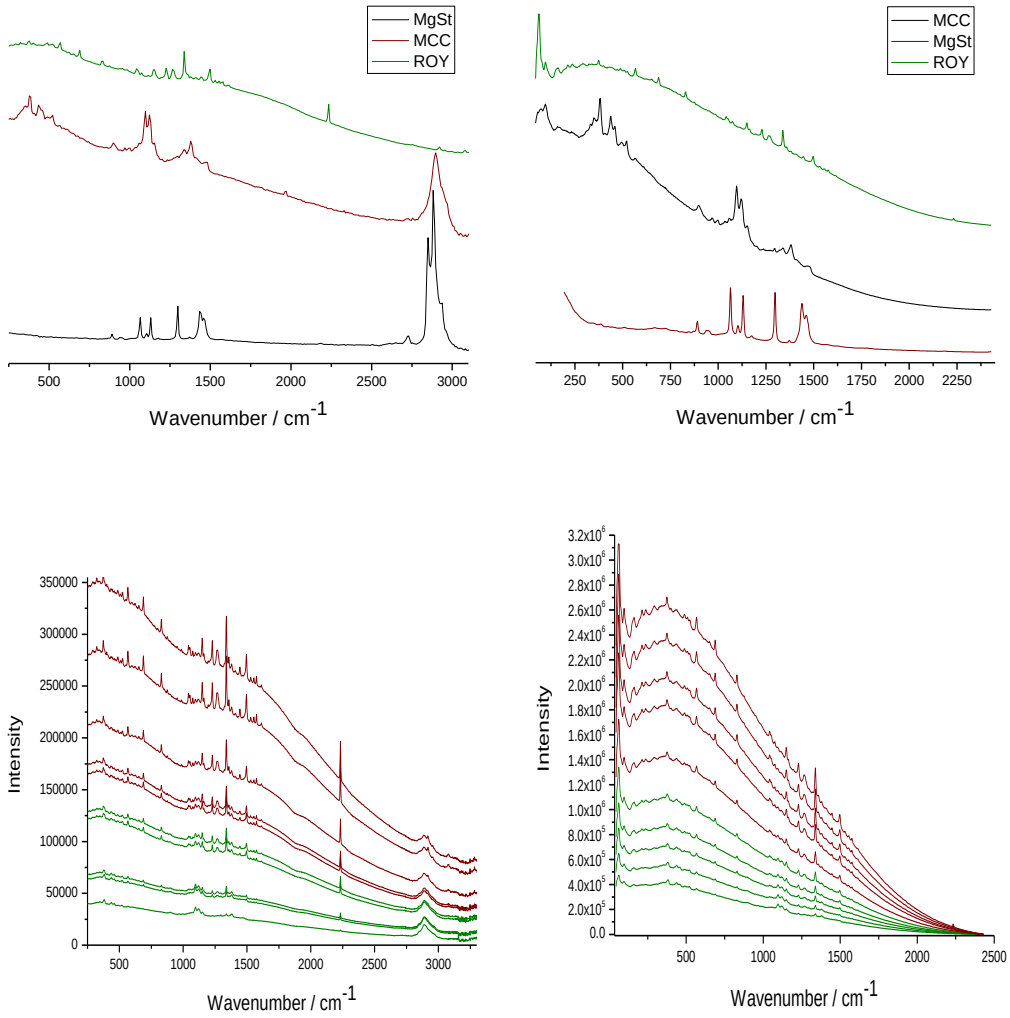

Figure 26 Top left and right, BRS and TRS spectra of tablet components respectively, and bottom left and right, BRS and TRS spectra of tablets respectively where the transition from green to red is due to increasing ROY content.

Fig 26 shows the BRS (250–3310 cm^{-1}) and TRS (44–2450 cm^{-1}) spectra of the tablet components and their Raman bands are listed in Table 11 – to our knowledge no detailed band assignment of ROY is available in the literature and is hence not provided here. Both sets of Raman spectra show well resolved bands which allow for facile observation of spectral differences between all components. One of the strongest features of ROY is the peak at 1338 cm^{-1} which may be attributable to $\nu(CNO_2)$ of ROY. MCC exhibits a sloping baseline with several bands in the 850 – 1500 cm^{-1} spectral region which are due to ν(C–O) and ν(C–C) stretching vibrations and $\delta(CH_2)$ deformations.(231-235) There are also peaks present at 380 and 460 cm^{-1} which are due to δ(CCC), δ(CO) and δ(CCO) binding vibrations and ring deformations.(236). A band at 1093 cm^{-1} is characteristic of unsubstituted cellulose rings which are found in MCC.(231) In the Raman spectrum of MgSt, bands at 1061 and 1128 cm^{-1} can be assigned to ν(CC) antisymmetric and symmetric stretching vibrations respectively and $\delta(CH_2)$ vibrations are responsible for Raman bands at 1294 and 1437 cm^{-1}.(71, 237)

A difference between the two Raman systems employed was the difference in spectral ranges accessible; the BRS system utilised the 250 – 3300 cm^{-1} range and the TRS system the 45–2500 cm^{-1} range. The TRS system allowed for the observation of Raman signal by the phonon mode region which can reveal bands specific to crystal lattice vibrations. It is also of interest to note that in this case ROY gives a strong Raman signal in this region without much interference from the excipients which may be of use for quantitative model generation.

As is evident particularly from the tablet spectral data generated by both Raman methods, ROY which is yellow in colour, imparts a growing fluorescent signal as the ROY content increases from 1 to 17.5% tablet weight. The laser power was adjusted to ensure that sample fluorescence did not swamp the Raman signal from the tablets, and a compromise of 70% laser power was used. Both Raman systems employed for this study made use of different laser sources, 785 and 830 nm for the BRS and TRS systems respectively which had an effect on the level of fluorescence present in each spectrum. The closer to a NIR wavelength that a laser employs the greater the reduction of the effects of fluorescence.

Table 11 Backscattered Raman bands of tablet components.

Compound	Raman Bands / cm^{-1}
ROY	290(w), 306(w), 323(w), 337(w), 370(m), 408(w), 442(w), 467(w), 490(w), 506(w), 522(w), 568(m), 603(w), 650(w), 689(m), 721(vw), 752(vw), 801(vw), 827(m), 873(vw), 921(vw), 952(vw), 1043(m), 1074(mw), 1122(w), 1147(m), 1196(w), 1226(m), 1267(m)m, 1338(s), 1377(w), 1442(mw), 1496(m), 1530(mw), 1554(mw), 1573(mw), 1611(mw)
Magnesium Stearate	888(w), 945(w), 1061(s), 1102(w), 1128(s), 1294(vs), 1437(s), 1458(m)
Microcrystalline Cellulose	343(w), 378(s), 435(m), 457(m), 517(m), 894(w), 1093(vs), 1120(s), 1152(m), 1335(m), 1378(m), 1473(w)

w, weak; mw, medium weak; m, medium; s, strong; vs, very strong.

5.3 Spectral region of interest selection

Specific regions of interest (ROIs) were selected from each set of spectral data for use in multivariate analysis. This allowed the analyst to make use of spectral features which were known to vary as a result of changing concentration *i.e.* the 625–1750 cm^{-1} spectral region specific to ROY in Raman spectral data; and also to omit spectral regions where little to no information could be utilised *i.e.* from 1800–2400 cm^{-1} in the TRS spectra or from 4–10 2θ in the PXRD patterns. This increased the speed of analysis. ROIs selected for multivariate analysis are detailed in Table 12.

Table 12 Regions of interest selected for model generation using NIR and Raman data.

Technique	Name	Wavenumber region / cm^{-1}
NIR	Full	10000–4000
	A and B	6200–4000
	A	6200–5400
	B	5400–4000
	ROY peak	5549–5481
Backscattered Raman	Full	250–3300
	A	250–626
	B	626–1750
	C	250–1750
	ROY peak	1314–1354
Transmission Raman	Full	44–2450
	A and B	44–1700
	A	44–625
	B	625–1700
	ROY peak	1327–1350

5.4 Spectral pre-processing

The aim of spectral pre-processing is to enhance information of interest such as that pertaining to the analyte of interest and to reduce redundant information such as noise which can impact quantitative analyses where unaccounted for. In the case of PXRD, data reduction was used to reduce analysis time. The original PXRD data files comprised 8192 data points over a range of PXRD diffraction patterns were reduced in half, using 4096 data points. This allowed for quicker model development and proved no worse than use of the full data set. Additionally a smoothing function and a normalisation step were applied to the PXRD data which both improved the noise levels and took account of intensity variations between the tablets. NIR raw spectra consist of much broader peaks and show some scattering variations and baseline offsets due to the interaction of light with the tablets. These scattering effects were corrected for using MSC (Multiplicative Scatter Correction) and all tablets have a uniform baseline (Fig. 27). This highlights the spectral differences between varying ROY concentrations which are present in the 6200 – 5300 cm^{-1} and 5000 – 4000 cm^{-1} spectral regions. The spectra were further pre-processed using a 15 point second derivative which maximised the ROY concentration differences between the tablets in the aforementioned regions.

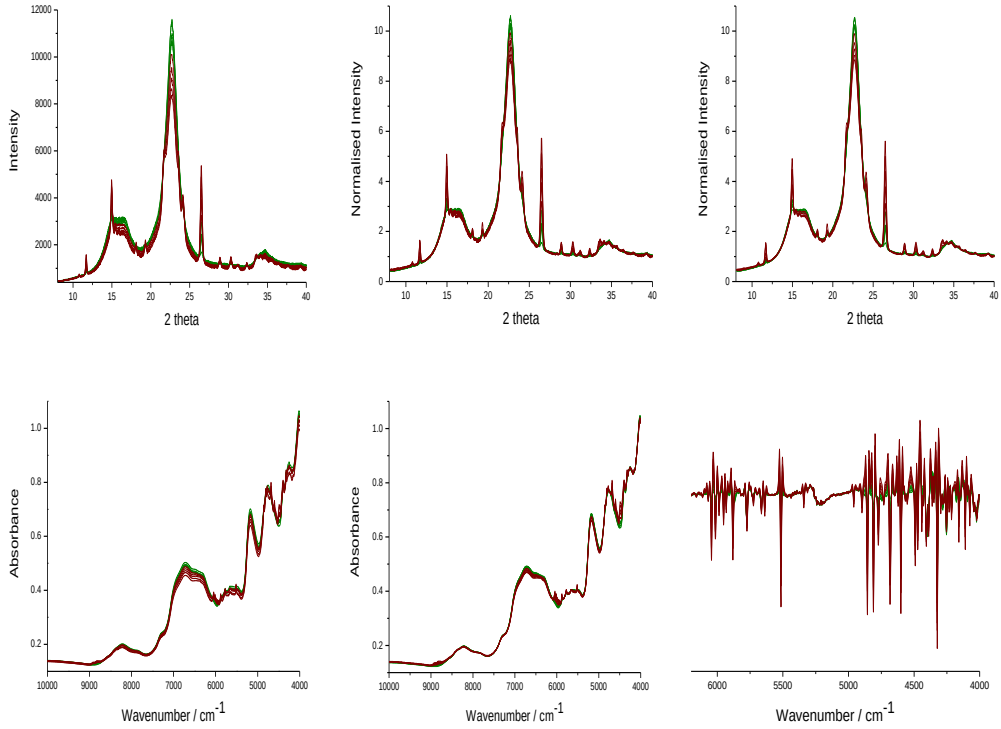

Figure 27 Top row from left to right; PXRD raw patterns, PXRD mean normalised patterns and PXRD mean normalised and smoothed patterns. Bottom row from left to right; NIR raw spectra, NIR MSC treated spectra and NIR MSC and second derivative pre-processed spectra

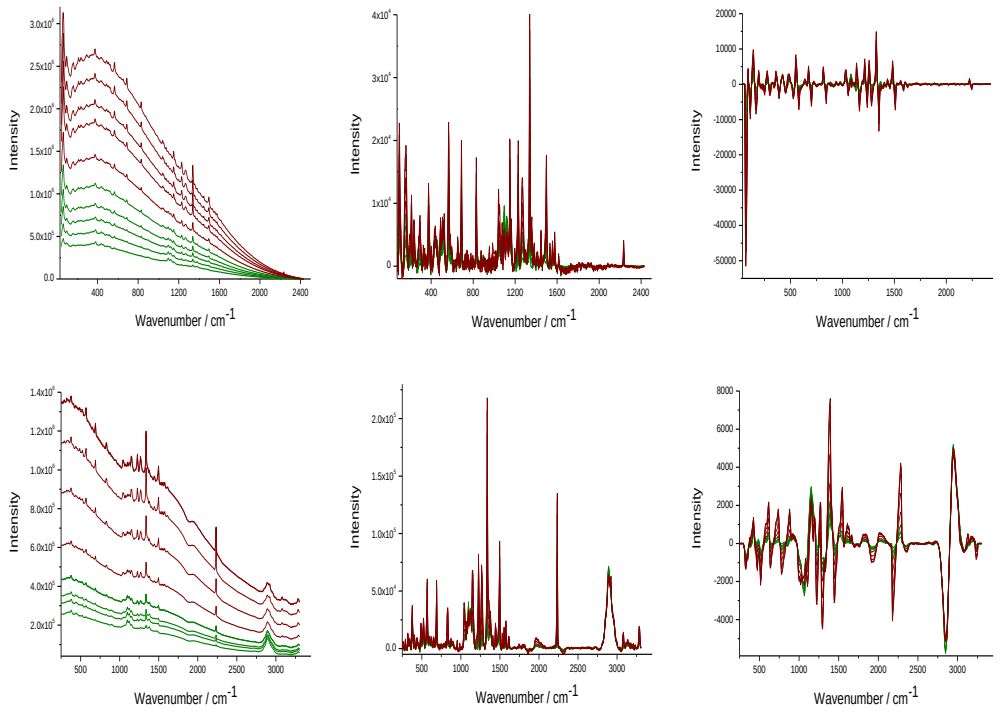

Figure 28 Top row from left to right; TRS raw spectra, baseline corrected spectra and baseline corrected and second derivative pre-processed spectra. Bottom row from left to right; BRS raw spectra, baseline corrected spectra and baseline corrected and second derivative pre-processed spectra.

Both sets of Raman spectral data contain a sweeping baseline due to fluorescence which goes upwards at lower wavenumbers (Fig. 28). In this case reduction of the laser power results in a reduction of the fluorescent baseline with less swamping of the ROY signals from the tablets. ROY has strong features particularly in the 600 – 1700 cm^{-1} spectral region. This area features a strong sharp peak associated with ROY at 1338 cm^{-1} which increases in intensity due to increasing ROY concentration. Two means of removing the effects of the fluorescent baseline were tested, manual baseline correction, the use of derivatives alone and in combination with baseline correction. The manual baseline correction required careful selection of a number of points in the spectra which were least affected by fluorescence and then fitted to an appropriate polynomial. This required an expert eye and careful review of the data. Derivatives are commonly used to correct for baseline changes due to fluorescence and most utilised are first and second derivatives. Both are shown by the two spectral sets in Fig. 28 which show strong fluctuations in their spectra that occur in spectral regions related to changing ROY concentration.

5.5 Quantitative Analysis 1mm tablets

5.5.1 Powder X-ray diffraction

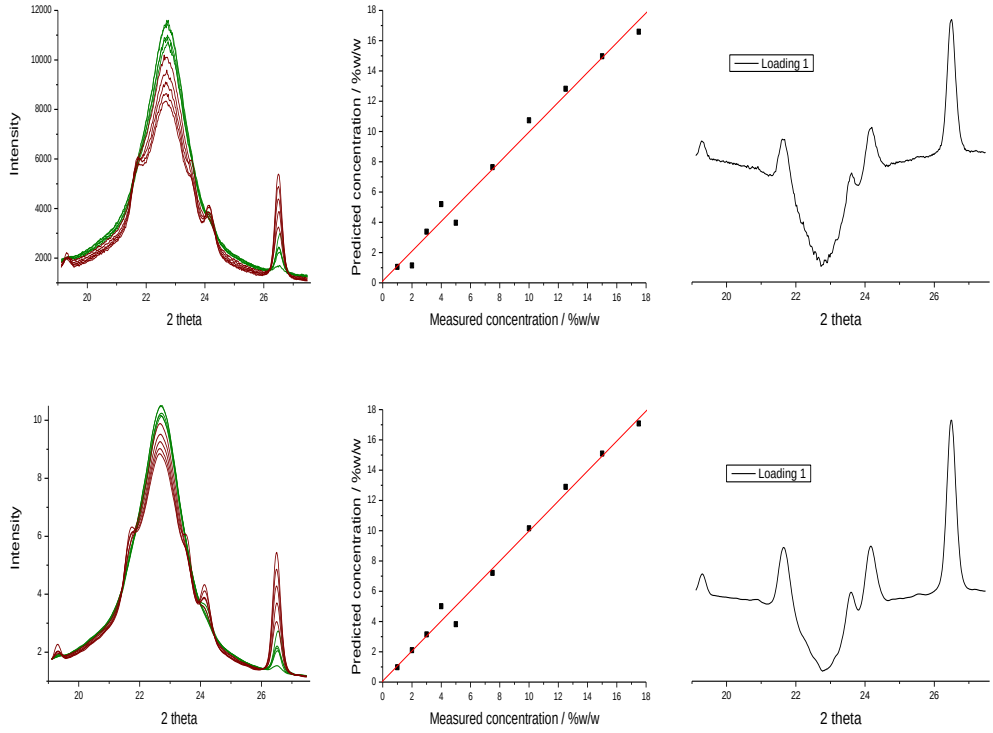

Figure 29 19 – 27.5 2θ region of PXRD patterns

The PXRD data was mean normalised and smoothed using a 5 point moving average (Fig. 29). The 5 point moving average serves to smooth data, reducing the signal–to–noise ratio of the data. PLS models were built using one PLS factor, with a selection of ROIs. One PLS factor was chosen as the majority of the x and y variance was captured in one latent variable with no appreciable improvement in model output when further loadings were incorporated into the models. The 19–27.5 and 19–26 2θ regions yielded lower RMSEs of 0.53% and 0.56% for calibration, and 0.58% and 0.31% for prediction, respectively (Table 13). The PC1 loading compares very well to the ROY diffraction pattern showing that this models biggest contributor is the changing concentration of ROY. The 2θ region from 21–24 2θ shows a dip in PC1 which can be attributed to the masking effects of MCC and MgSt in this region, as this is where both components have strong broad peaks which hide any diffraction

peaks of ROY from showing. The RMSEC values barely change between the mean normalised models in comparison with the mean normalised and smoothed models however the latter model has improved RMSEP values. The loadings are similar between the two with a negative contribution from the MCC broad peak at 22.8 2θ and with positive contributions with peaks associated with ROY i.e. 19.2, 24.2 and 26.5 2θ.

Table 13 Results of regression models built using PXRD 1mm tablet data.

Pre–processing	Region	LV	RMSEC	R^2	RMSECV	RMSEP
Data reduced	Half	1	0.71	0.9914	0.90	0.65
	A and B	1	0.70	0.9918	0.89	0.63
	A	1	0.78	0.9897	1.02	1.01
	B	1	0.87	0.9871	1.23	2.08
Mean normalised	Half	1	0.52	0.9954	0.64	1.04
	A and B	1	0.54	0.9952	0.65	0.81
	A	1	0.56	0.9946	0.74	0.42
	B	1	0.77	0.9901	0.91	1.26
Mean normalised & moving average	Half	1	0.52	0.9954	0.64	0.93
	A and B	1	0.54	0.9952	0.65	0.71
	A	1	0.56	0.9946	0.74	0.38
	B	1	0.77	0.9901	0.91	1.12

5.5.2 Near infra-red spectroscopy

PLS models built using NIR spectra treated with MSC pre-processing were made using 2 PLS factors for all ROIs that were selected. Regions of interest were selected to see if certain areas or combination of these areas could yield better PLS models with fewer PLS factors and lower RMSEs. Use of the full spectrum 10000–4000 cm^{-1} gave the best model with RMSEs of 0.26% for calibration and 0.31% for prediction (Table 14). A near equivalent performing model using the region of interest from 6200–4000 cm^{-1} encompassed the main features of the tablet components. MSC pre-processing performed very well in this area in particular, smoothing out differences in baseline offset and scattering variations in the model tablets (Fig. 30). MSC also reduced the number of latent variables to one for all models indicating that the models are now wholly concerned with the chemical differences between the tablets as opposed to the physical differences between the tablets which resulted in varying interactions with the NIR radiation. The loadings of PC1 closely resemble the spectrum of ROY showing that this model is mostly based on the changing

concentration of ROY of the model tablets. Noticeably in all loadings plots there is a negative contribution from the broad peak of MCC at 5300 cm^{-1}.

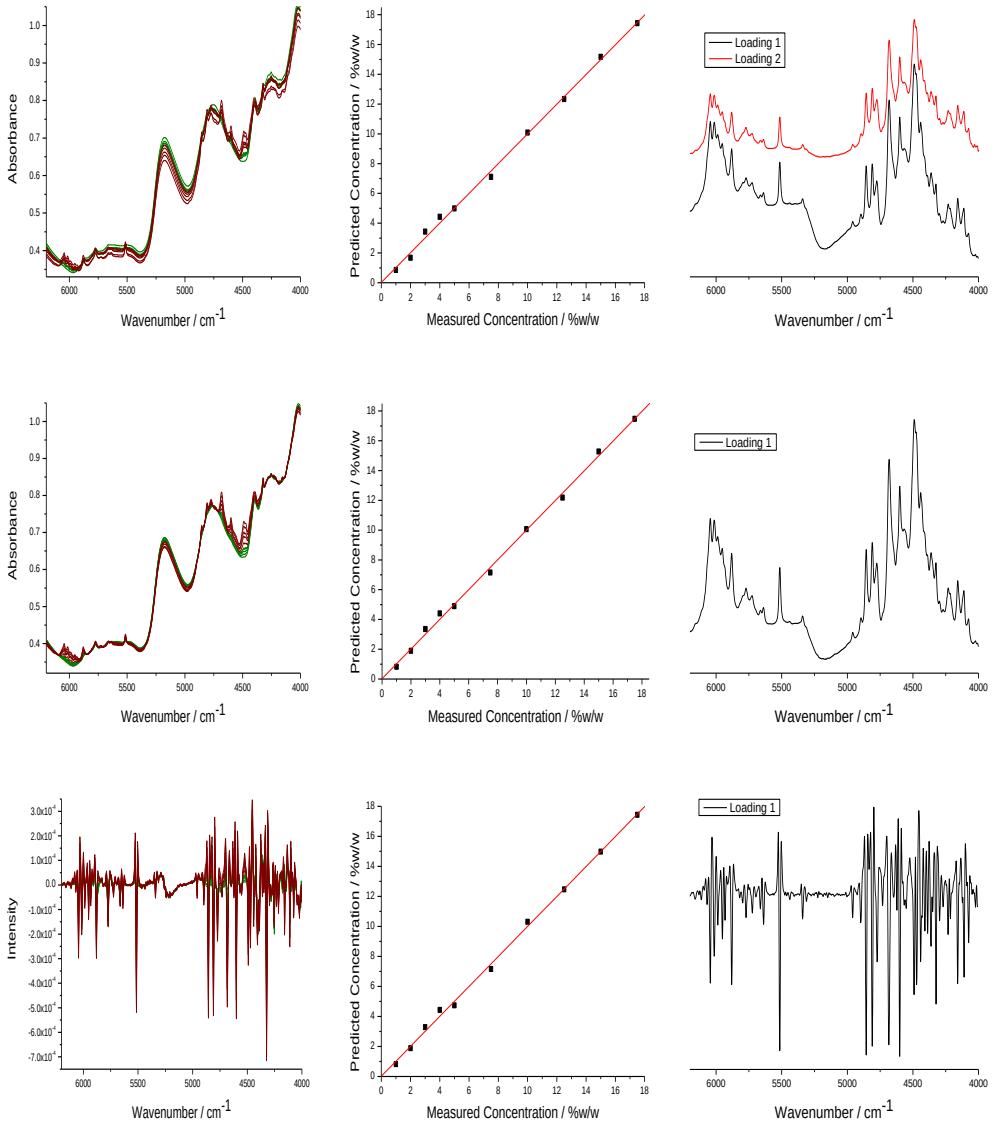

Figure 30 Top left, raw NIR spectra; top middle, measured vs. predicted ROY concentration plot; top right, loadings of PLS model of raw spectra; center left, MSC pre-processed NIR spectra; center middle, measured V predicted ROY concentration plot; and center right, loading of this PLS model. bottom left, MSC and 2nd derivative pre-processed NIR spectra; bottom middle, measured vs. predicted ROY concentration plot; and bottom right, loading 1 of best performing PLS model.

Table 14 Results of PLS models generated using 1 mm NIR spectral data. RMSE in % w/w.

Pre–processing	Region	LV	RMSEC	R^2	RMSECV	RMSEP
	Full	2	0.26	0.9989	0.38	0.31
	A and B	2	0.27	0.9988	0.36	0.30
Raw data	A	2	0.26	0.9989	0.33	0.42
	B	2	0.27	0.9987	0.38	0.29
	ROY peak	2	0.26	0.9989	0.31	0.46
	Full	1	0.23	0.9991	0.28	0.17
	A and B	1	0.25	0.9989	0.31	0.16
MSC	A	1	0.29	0.9986	0.34	0.23
	B	1	0.26	0.9989	0.32	0.19
	ROY peak	1	0.24	0.9990	0.28	0.48
	Full	1	0.22	0.9992	0.27	0.31
	A and B	1	0.22	0.9992	0.27	0.31
MSC & 2^{nd} deriv.	A	1	0.24	0.9990	0.29	0.29
	B	1	0.23	0.9992	0.27	0.35
	ROY peak	1	0.25	0.9990	0.29	0.43

Combining MSC and a second derivative pre-processing step results in further improvement of PLS models generated using the NIR data. All models are nearly equivalent with the best performing model being that concerning the entire or 6200 – 4000 cm^{-1} spectral regions which encompass all concentration differences between the tablets. Once MSC accounted for the baseline offsets of the data, the second derivative accentuates differences between the tablets which are a result of increasing concentration of ROY.

5.5.3 Backscattered Raman spectroscopy

Reviewing the effect of spectral region selection regarding the raw BRS spectral data shows no improvement on the RMSEC, RMSECV and R^2 values (Table 15). On pre-processing with a first or second derivative, there is little change in these values however there is a reduction in the RMSEP values. The smaller the difference between RMSEC and RMSEP the better the model and this is the case on pre-

processing with a first derivative. The B and C regions corresponding to 626–1706 and 250–1750 cm^{-1} provide the best quantitative models on that basis and their results are presented in Table 15 below. The loadings plot indicate that the peak at 1338 cm^{-1}, characteristic of ROY is a large contributor to all models as this peak increases in intensity with increasing ROY concentrations.

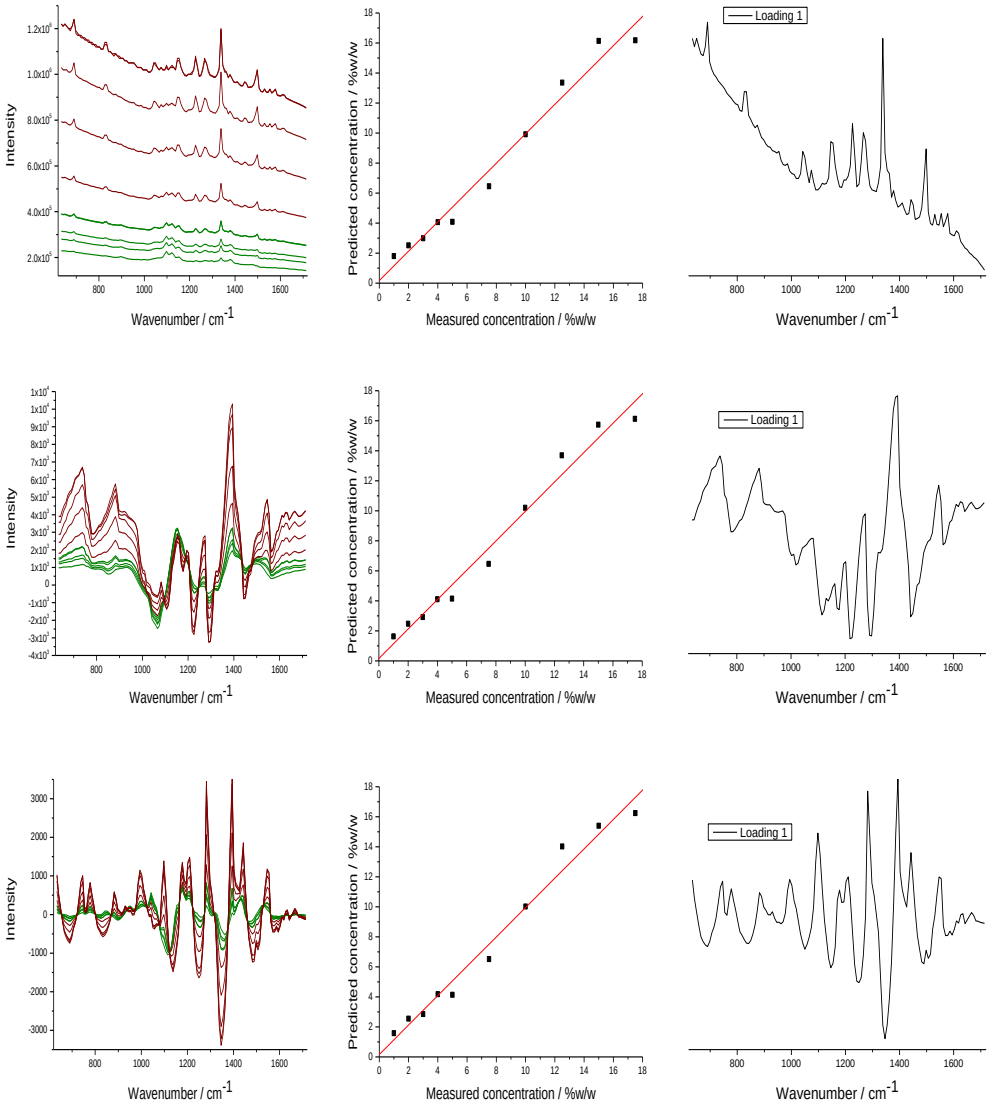

Figure 31 BRS spectra. Top row, raw BRS spectra, middle row, BRS first derivative pre-processed spectra, bottom row, BRS second derivative pre-processed spectra. First column, spectral data; second column, measured vs. predicted concentration plot of ROY concentration; and third column, loadings plots.

Table 15 PLS model results generated by use of 1 mm derivative BRS spectral data. RMSE in % w/w.

Pre–processing	Region	LV	RMSEC	R^2	RMSECV	RMSEP
Raw	Full	1	0.82	0.9887	1.08	1.11
	A	1	0.82	0.9887	1.08	1.11
	B	1	0.81	0.9888	1.07	1.10
	C	1	0.82	0.9888	1.08	1.11
	ROY peak	1	0.81	0.9888	1.07	1.03
1^{st} SG	Full	1	0.80	0.9891	1.05	1.04
	A	1	0.91	0.9860	1.24	1.08
	B	1	0.80	0.9893	1.04	0.85
	C	1	0.91	0.9889	1.06	0.89
	ROY peak	1	0.99	0.9836	1.31	2.03
2^{nd} SG	Full	1	0.81	0.9889	1.05	0.47
	A	1	0.84	0.9882	1.08	0.96
	B	1	0.80	0.9891	1.04	0.42
	C	1	0.81	0.9890	1.05	0.45
	ROY peak	1	0.81	0.9889	104	0.51

Baseline correction was also used to correct for the fluorescence baseline and subsequently pre-processed using either a first or second derivative (Table 16 and Fig. 32). Using a first derivative resulted in the best quantitative models for the B region which encompassed the main features of ROY. Selecting this area alone resulted in models with similar performance to the B spectral region.

Table 16 Results of PLS models generated using 1 mm BRS baseline corrected spectral data. RMSE in % w/w.

Pre–processing	Region	LV	RMSEC	R^2	RMSECV	RMSEP
Baseline corrected	Full	1	0.83	0.9885	1.09	0.37
	A	1	0.85	0.9878	1.11	0.89
	B	1	0.82	0.9885	1.08	0.34
	C	1	0.83	0.9885	1.09	0.36
	ROY peak	1	0.82	0.9888	1.07	0.38
Baseline corrected and 1^{st} SG	Full	1	0.80	0.9892	1.06	0.50
	A	1	0.83	0.9884	1.09	0.90
	B	1	0.80	0.9893	1.06	0.43
	C	1	0.80	0.9893	1.05	0.48
	ROY peak	1	0.80	0.9891	1.05	0.53
Baseline corrected and 2^{nd} SG	Full	1	0.81	0.9890	1.07	0.44
	A	1	0.83	0.9884	1.10	0.45
	B	1	0.80	0.9891	1.06	0.40
	C	1	0.80	0.9891	1.06	0.40
	ROY peak	1	0.81	0.9890	1.06	0.40

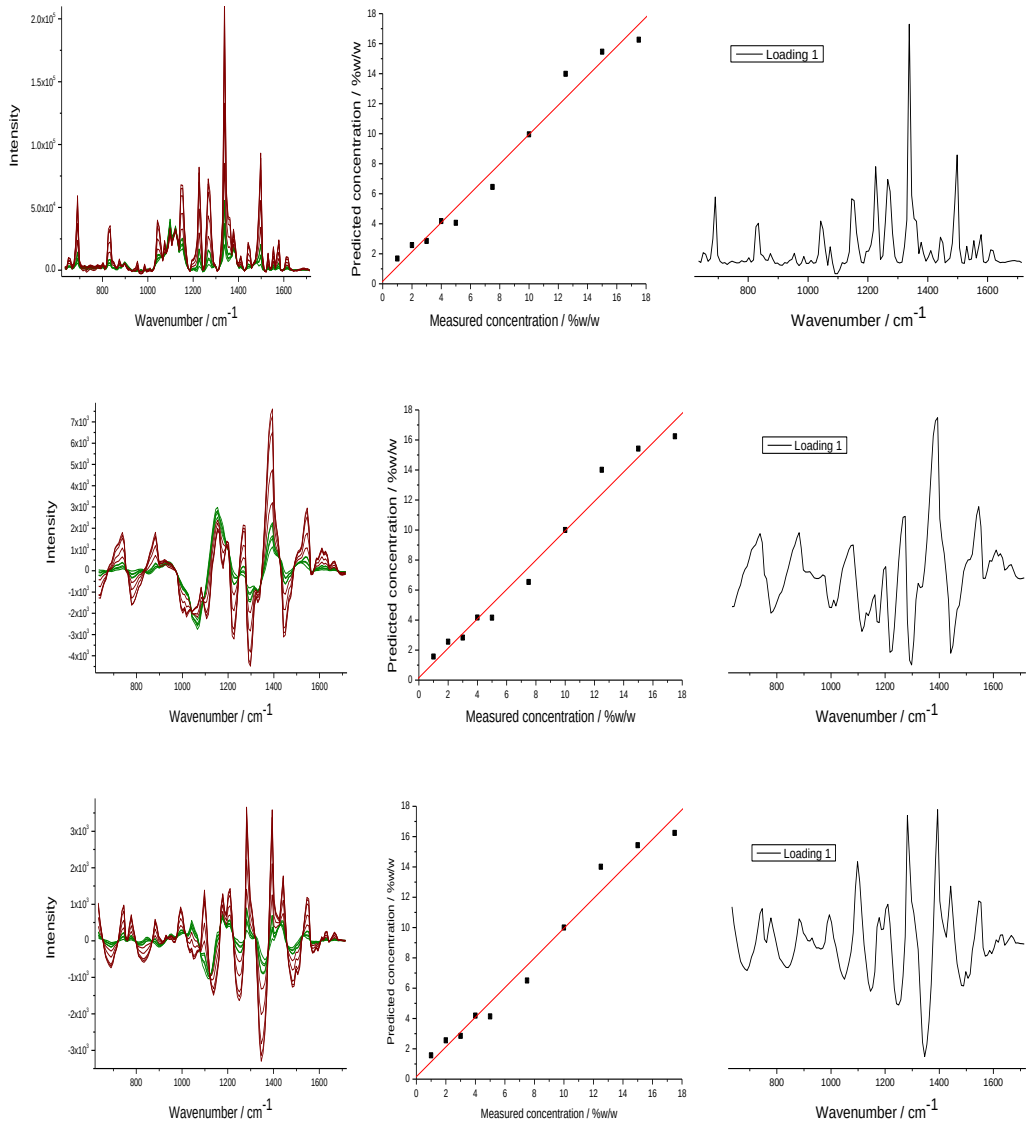

Figure 32 BRS spectra. Top row, baseline corrected BRS spectra, middle row, BRS first derivative pre-processed spectra, bottom row, BRS second derivative pre-processed spectra. First column, spectral data; second column, measured vs. predicted concentration plot of ROY concentration.

5.5.4 Transmission Raman spectroscopy

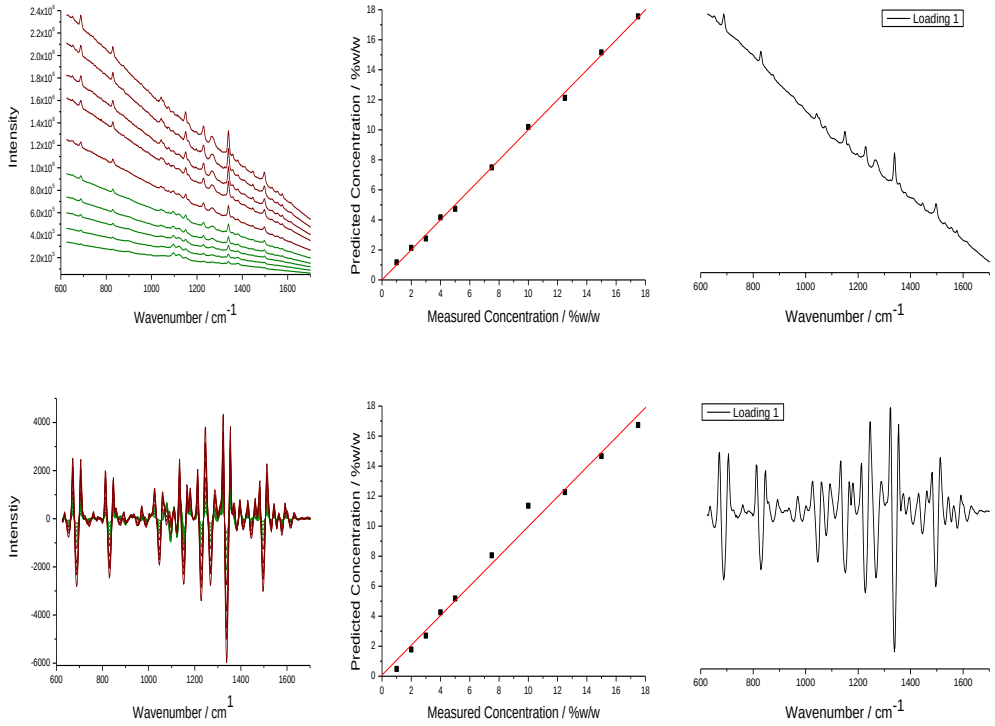

Figure 33 Top row, raw TRS spectra, bottom row, TRS second derivative pre-processed spectra. First column, spectral data; second column, measured vs. predicted concentration plot of ROY concentration; and third column, loadings plots.

All tablets share sloping baselines due to the increasing levels of fluorescence with increasing ROY concentration. The loadings plot of a PLS model built using the raw spectra of the 625–1700 cm^{-1} spectral region show that this fluorescent baseline dominates, however features of both MCC and ROY are present in the loadings plots particularly in the region around 1350 cm^{-1} which is due to the presence of ROY (Fig. 33). Using this region RMSEC and RMSECV values of 0.70 and 0.85% w/w were achieved with a high linear correlation of 0.9917 (Table 17). On testing the calibration model using the external prediction set a RMSEP of 1.72% w/w was achieved which suggests that these samples are poorly accounted for using a PLS model built using raw spectral data. This could be due to the effects of fluorescence on the spectral baseline. To counteract this fluorescent baseline a second derivative was applied to the spectral data. As shown in the above spectra, strong signals due to the changing concentrations of MCC and ROY are present. A higher correlation was

achieved with lower RMSEC and RMSECV errors reported in Table 17 with a much improved RMSEP of 0.33% w/w.

Table 17 Results of PLS models generated using 1 mm TRS spectral data. RMSE in % w/w.

Pre–processing	Region	LV	RMSEC	R^2	RMSECV	RMSEP
Raw data	Full	1	0.73	0.9909	0.87	1.77
	A and B	1	0.73	0.9909	0.89	1.78
	A	1	0.76	0.9903	0.92	1.82
	B	1	0.70	0.9917	0.85	1.72
	ROY peak	1	0.67	0.9924	0.80	1.46
2^{nd} Deriv.	Full	2	0.64	0.9931	0.83	0.40
	A and B	2	0.64	0.9930	0.83	0.41
	A	1	0.97	0.9842	1.24	0.47
	B	1	0.66	0.9926	0.79	0.33
	ROY peak	1	0.66	0.9927	0.78	0.31

Another approach commonly used to counteract fluorescent baselines in Raman spectral data is to baseline correct the spectra either manually or by some automated method such as the Lieber method. For this case manual baseline correction using Matlab proved to be the best for this case resulting in lower RMSE errors and also a lower RMSEP when compared to raw TRS data. Further pre-processing of the baseline corrected data using either a first or second derivative results in RMSEC and RMSECV values of 0.65 and 0.77% w/w using a first derivative which proves to be the best performing PLS model generated using the 625–1700 cm^{-1} spectral region (Table 18 and Fig. 34). Little difference was found between the second derivative TRS data and that which was baseline corrected prior to employment of the second derivative.

Table 18 Results of PLS models generated using 1 mm TRS spectral data. RMSE in % w/w.

Pre–processing	Region	LV	RMSEC	R^2	RMSECV	RMSEP
	Full	2	0.86	0.9877	1.09	0.46
	A and B	1	0.77	0.9900	0.97	0.37
Baseline corrected	A	1	0.88	0.9871	1.11	0.48
	B	1	0.62	0.9935	0.73	0.30
	ROY peak	1	0.63	0.9934	0.74	0.30
	Full	2	0.61	0.9937	0.82	0.40
	A and B	2	0.61	0.9937	0.83	0.40
Baseline corrected	A	1	0.92	0.9857	1.17	0.56
and 1st deriv.	B	1	0.65	0.9929	0.77	0.32
	ROY peak	1	0.65	0.9928	0.78	0.29
	Full	2	0.64	0.9931	0.83	0.40
	A and B	2	0.64	0.9930	0.83	0.41
Baseline corrected	A	1	0.97	0.9842	1.24	0.47
and 2nd deriv.	B	1	0.66	0.9926	0.79	0.33
	ROY peak	1	0.66	0.9927	0.78	0.31

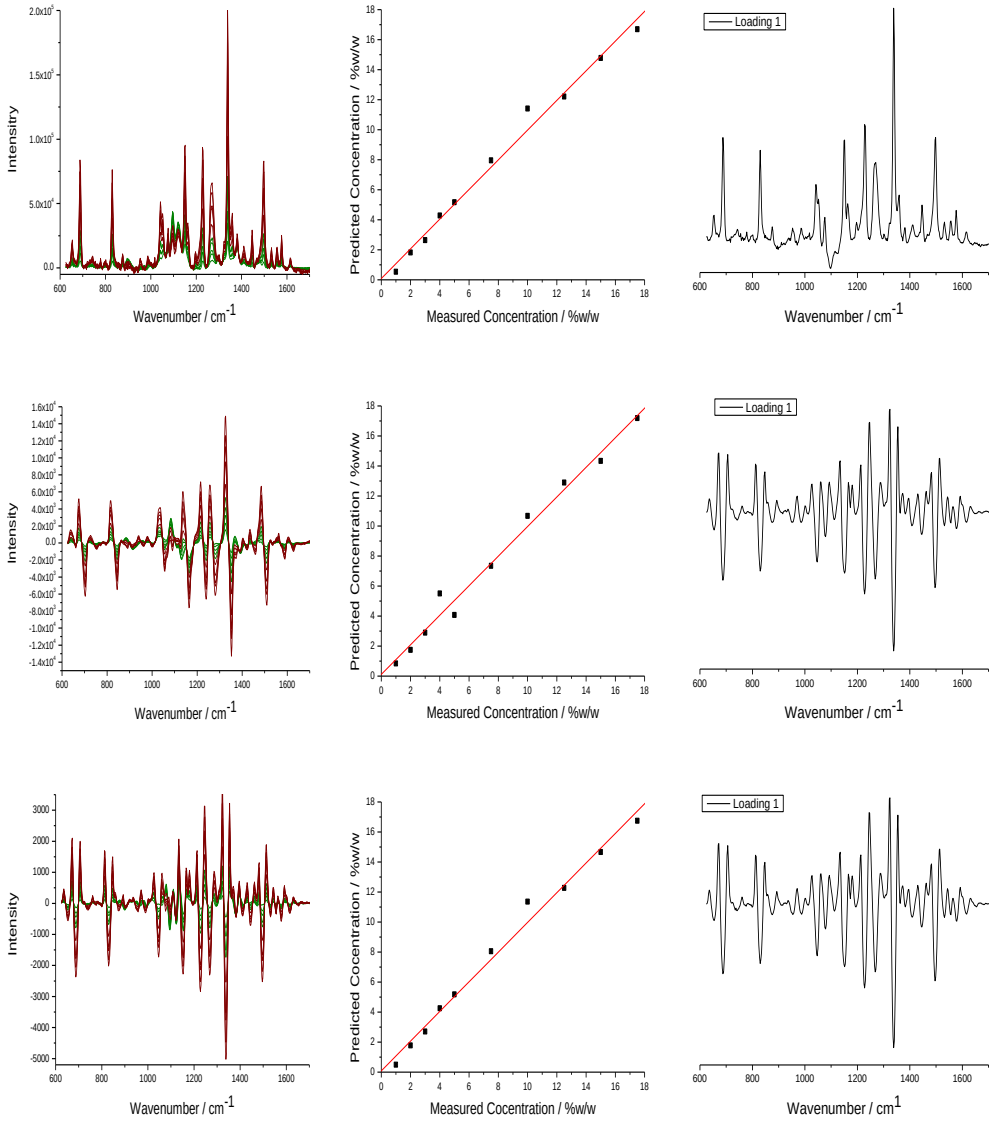

Figure 34 TRS spectra. Top row, baseline corrected TRS spectra, center row TRS and first derivative pre-processed TRS spectra, and bottom row, TRS baseline corrected and second derivative pre-processed spectra. First column, spectral data; second column, measured vs. predicted concentration plot of ROY concentration; and third column, loadings plots.

5.6 Discussion

A summary of the best quantitative models for 1 mm thick tablets is presented in Table 19 where the optimal pre-processing for each model is included.

Table 19 PLS quantification results of 1 mm tablets for analytical techniques using the best means of pre-processing for each technique using different regions of interest.

Method	Pre–processing	PLS Factors	RMSEC	R^2	RMSECV	RMSEP
NIR	MSC & 2nd SG	1	0.22	0.9992	0.27	0.31
TRS	Baseline corrected & 2nd SG	1	0.66	0.9926	0.79	0.33
BRS	2nd SG	1	0.8	0.9893	1.04	0.85
PXRD	Normalised & 5 point average	1	0.54	0.9952	0.65	0.71

Transmission Raman spectra which were collected at a 5 second total exposure time per sample yielded good PLS models consisting of 1 PLS factor in all cases once the spectra were baseline corrected and then pre-processed using a second derivative. Using a specific region of interest from 1700–625 cm^{-1} yielded the best model with RMSEs of 0.66% for calibration and 0.33% for prediction. This compared very well to what could be considered as the univariate analysis of a ROY specific peak at 1327–1350 cm^{-1} which produced a model with RMSEs of 0.63% for calibration and 0.30% for prediction. These two particular regions of interest may have performed better than those models built using the larger regions of interest such as the entire spectrum due to the fact that the region from 800–2450 cm^{-1} would have been easier to have baseline corrected manually in comparison to the highly increasing baseline from 44–800 cm^{-1}. These results mark an improvement in RMSEs previously published in the literature of 2.2% for pharmaceutical tablets and 1.5% for pharmaceutical capsules for quantitation of API content(180, 238).

In terms of the baseline corrected, derivatised and their combination of pre-processing Raman data showed that they were near equivalent in terms of RMSEC and CV values. However, there is a difference in RMSEP values reported for either pre-processing technique. Prediction errors associated with baseline corrected data

which is then subsequently derivatised result in very low values suggesting that the models generated may be over–predicting the validation data. The prediction errors associated with the derivative processed models is closer in value with the error associated with full internal cross validation and is a more reliable model to use for the quantification of ROY by BRS.

PXRD is considered the gold standard method in the differentiation of solid state forms however analysis time can be lengthy, for this experiment each tablet was analysed for 16 minutes by the diffractometer in triplicate resulting in a total analysis time of 48 minutes. For materials that are not particularly crystalline such as the MCC used in the fabrication of the tablets, broad peaks are present which can overlap and hinder analysis of peaks at the same value of 2θ. Normalisation and a moving average were utilised to improve the signal–to–noise ratio of the data.

In comparison, NIR is rapid, with each analysis taking roughly 2 and a half minutes per tablet, though similar to PXRD the broad nature of spectra does not lead to facile or direct interpretation. In addition for the case presented here the spectra closely mirror that of MCC with only subtle peaks due to ROY observable which require multivariate methods to be used for effective analysis. Across all thickness NIR was superior in measuring from 0.75 to 1.50 mm thick tablets with the Raman models hampered by fluorescence as shown in Table 20. TRS models appear to be better than the corresponding BRS models potentially due to enhanced sampling and slightly improved fluorescence dampening due to different laser sources – (830 nm vs. BRS 785 nm).

Table 20 PLS quantification results of tablets of all thicknesses for analytical techniques using the best means of pre-processing for each technique using different regions of interest.

Method	Thickness	Pre-processing	LV	RMSEC	R^2	RMSECV	RMSEP
NIR	0.75	MSC & 2^{nd} SG	1	0.43	0.9968	0.60	0.27
	1.00		1	0.22	0.9992	0.27	0.31
	1.25		1	0.42	0.9971	0.59	0.45
	1.50		1	0.38	0.9975	0.52	0.30
TRS	0.75	Baseline corrected	1	0.58	0.9944	0.74	0.43
	1.00	& 2^{nd} SG	1	0.66	0.9926	0.79	0.33
	1.25		1	0.43	0.9969	0.54	0.49
	1.50		1	0.87	0.9871	1.15	0.81
BRS	0.75	2^{nd} SG	1	0.84	0.9881	1.09	1.00
	1.00		1	0.80	0.9893	1.04	0.85
	1.25		1	0.41	0.9972	0.48	1.80
	1.50		1	0.76	0.9903	0.94	0.37

5.7 Chapter conclusions

Quantitative analysis of a model pharmaceutical tablet system consisting of an API–type molecule in a matrix of two excipients was feasible using NIR and Transmission Raman spectroscopies and PXRD. In each case, spectral pre-processing to remove instrumental and measurement artefacts were critical to the development of robust quantitative models.

PXRD based models could be generated with relatively high RMSEC and RMSEP accuracies of 0.56 and of 0.31 respectively. However, the method was more time consuming than vibrational spectroscopy based methods. NIR spectroscopy gave the best accuracy RMSEC of 0.26, RMSEP of 0.31, and the method is rapid. However, NIR spectra do not give much features with which one can analyse in detail variances in composition. Transmission Raman Spectroscopy (TRS) gave 0.66 (RMSEC) and 0.33 (RMSEP) which was intermediate in performance. The main factor which degraded the TRS performance was the substantial fluorescence in the model system arising from the MCC and the ROY itself, this reduced the S/N and made the generation of more accurate models unfeasible. In terms of time, TRS was by far the quickest means of analysis, taking approximately 5 seconds per tablet which contrasts to the 2.5 and 16 minutes per sample necessary for NIR and PXRD respectively.

6 Piracetam

The subsequent studies in this thesis focus on the quantitation of polymorphs of piracetam in both binary polymorph mixtures and within a model formulation to assess the ability of vibrational spectroscopy. Chapter 6 details the polymorphism of piracetam along with its spectral characterisation. Chapter 7 is concerned with the analysis of binary polymorph mixtures of piracetam FII and FIII. PXRD and vibrational spectroscopy was employed along with univariate and multivariate analyses to assess this binary system. Chapter 8 focuses on the use of vibrational spectroscopies for the determination of low level polymorphic contaminant in a model formulation.

6.1 Introduction to piracetam

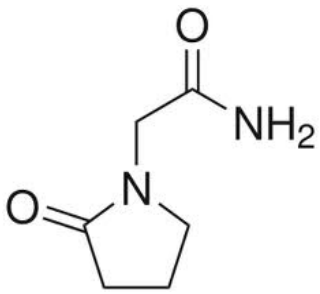

Figure 35 Chemical structure of piracetam (2–oxo–1–pyrrolidine acetamide).

Piracetam (2–oxo–1–pyrrolidine acetamide) is a nootropic drug which is linked to cognitive enhancement and has been used for the treatment of Alzheimer's and dementia.(239, 240) There are five polymorphs reported in the literature. Forms IV and V are yielded in a diamond anvil cell under high pressure (> 0.5 GPa) conditions.(35, 36, 225, 241) Forms I, II and III have all been characterised however Form I is very unstable and produced by heating Form II or Form III to 400 K and subsequent quenching to room temperature.(225, 226) Within hours it transforms to Form II. Form II is considered to be the metastable polymorph and Form III the stable polymorph, as determined by melting points by Kuhnert–Brandstatter *et al.*(241) The packing arrangements of FIII and FII are similar; they share the same hydrogen packing motif (Fig. 36) featuring networks of centrosymmetric hydrogen–bonded dimers of piracetam molecules; the two forms pack differently as shown.(242)

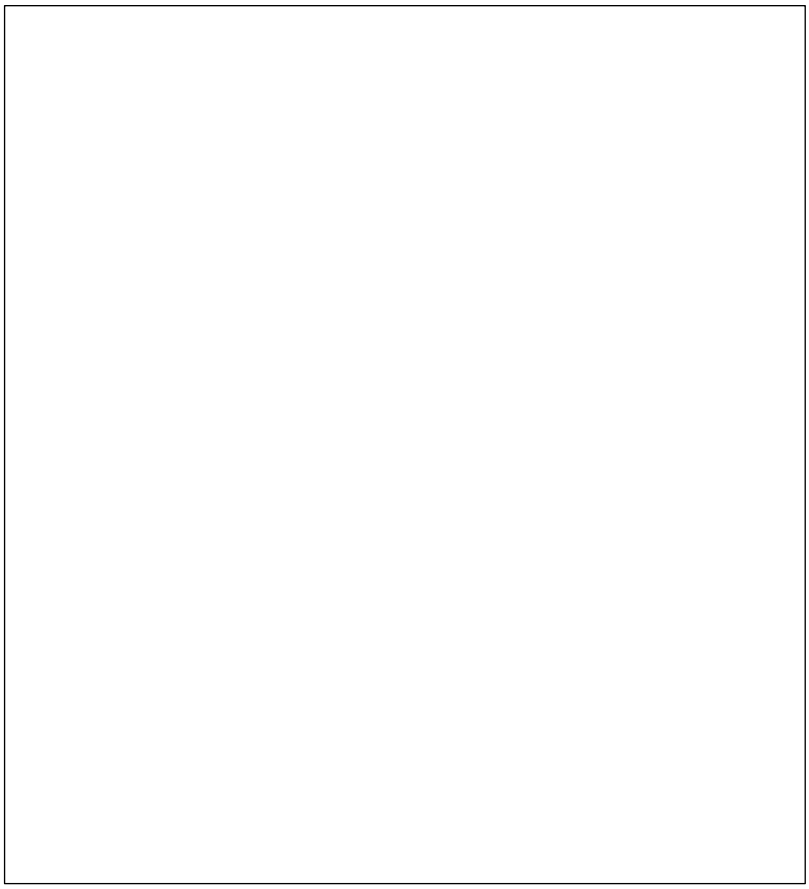

Figure 36 Schematics of form II and III piracetam molecular packing and their shared hydrogen bonding motif as reproduced from Ceolin *et al.* (226) and Fabbiani *et al.* (35).

Recent studies of piracetam include co–crystal generation, *in–situ* monitoring of supersaturation and polymorph interconversions in solvent systems. (243, 244) (207, 245). By use of carboxylic functionalised molecules several co–crystals of piracetam could be prepared by solvent evaporation, solvent drop grinding or crystallisation of mixtures of co–crystal formers and piracetam. (20, 244) Spectroscopic techniques including Raman and IR were used to monitor the polymorphic form produced and supersaturation of a cooling crystallisation of piracetam in ethanol. Raman showed particularly good differentiation between the two polymorphic forms and the authors made use of the differences found from 1640 – 1670 cm^{-1} to characterise the forms.(207) Energy Dispersive X-ray Diffraction (ED–XRD) was used to study solvent influences on the crystallisation of polymorphic and hydrate forms of piracetam where from a variety of solvents the crystalline form as a result of time and temperature could be monitored *in–situ*.(245)

6.2 Raman spectroscopy of piracetam

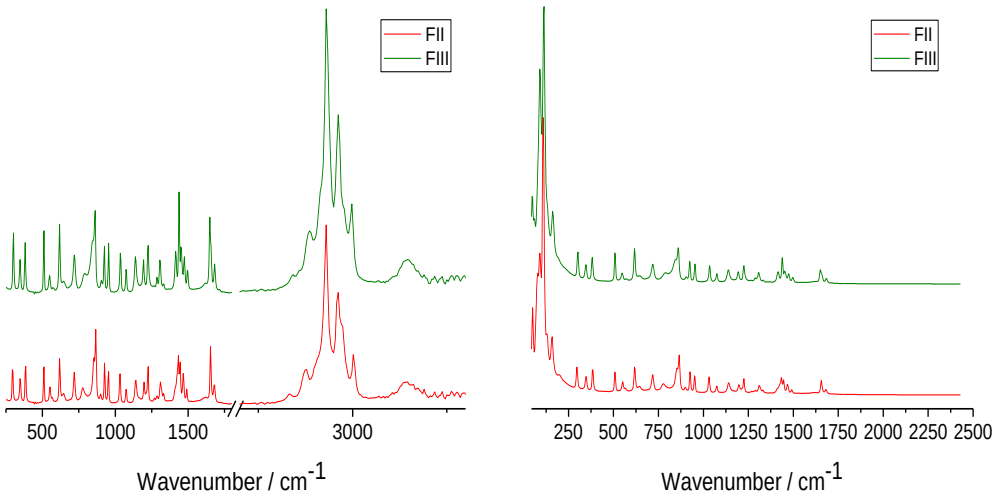

Figure 37 Raman spectra of FII and FIII piracetam, left BRS spectra and right TRS spectra.

The Raman spectra of the polymorphs show considerable differences, Fig. 37. Khamchukov *et al.* assigned Raman bands to piracetam ascribing the bands around 3140, 1680 and 1650 cm^{-1} to symmetric stretching vibrations of NH_2, and the amide C=O stretching vibration respectively in the ring and acetamide.(246) The bands around 2750–2990 cm^{-1} regions can be assigned to the symmetric and anti–symmetric stretching vibrations of the CH_2 groups.

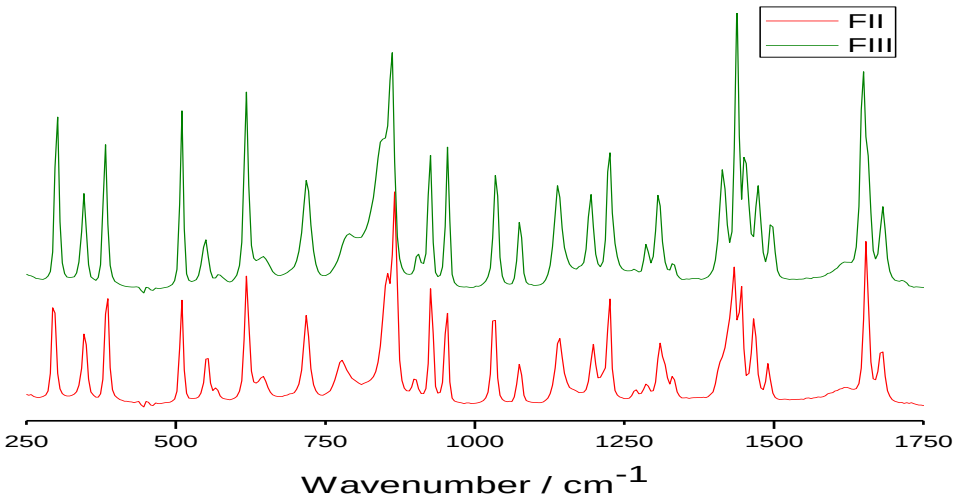

Figure 38 Raman spectra of piracetam polymorphs.

Inspection of the spectral region from 250–1750 cm^{-1} reveals many differences between the polymorphs, Fig. 38. FII has a single amide I band at 1654 cm^{-1}, while in the FIII form this is split into a pair of peaks at 1658 and 1648 cm^{-1}. A peak specific to FIII is present at 1410 cm^{-1} and band shifts are observable in the 1530–1370 cm^{-1} spectral region. Also evident are band shifts in the 890–1750 cm^{-1} spectral region which are due to changes in the bond lengths and angles made by atoms adjacent to the carbonyl groups.

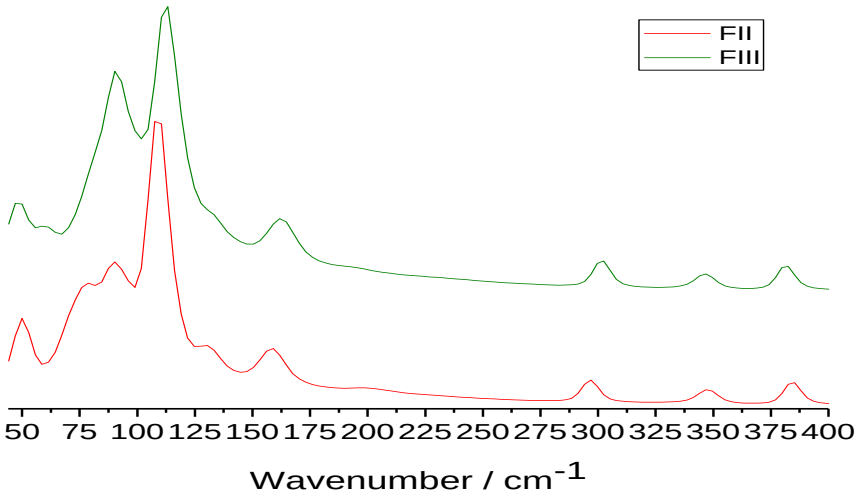

Figure 39 TRS spectra of piracetam polymorphs in 44–270 cm^{-1} spectral region.

Using this particular TRS instrument, information pertaining to the phonon mode region down to 44 cm^{-1} could be attained (Fig. 39). The spectra reveal very significant differences between the two polymorphs with 3–5 cm^{-1} differences observed for several of the bands at ~380, 300, 160, and 110 cm^{-1}. The other major difference is a splitting of the 91 cm^{-1} band in the FII polymorph where we see a reduction in the intensity at 91 cm^{-1} coupled with the appearance of a strong shoulder at 79 cm^{-1}. Khamchukov *et al.* observed the same bands at low wavenumbers, and ascribed the vibrational modes at 42, 84, 125 cm^{-1} to crystal lattice vibrations.(246) It is noted that in this work a band at 91 cm^{-1} and not at 84 cm^{-1} was observed as shown in Fig. 39. The peak shift around 106 cm^{-1} is attributed as an out-of-plane vibration in the amide group, which is due to the change in the angle between $C_6C_5N_3$ (the carbon adjacent to the ring, C=O and amide N) and $O_2C_5N_3$ (O of carboxyl group, C of carboxyl group and amide N) planes. The remaining Raman

band assignments are adapted from the literature and presented in the Table 21 overleaf. (246)

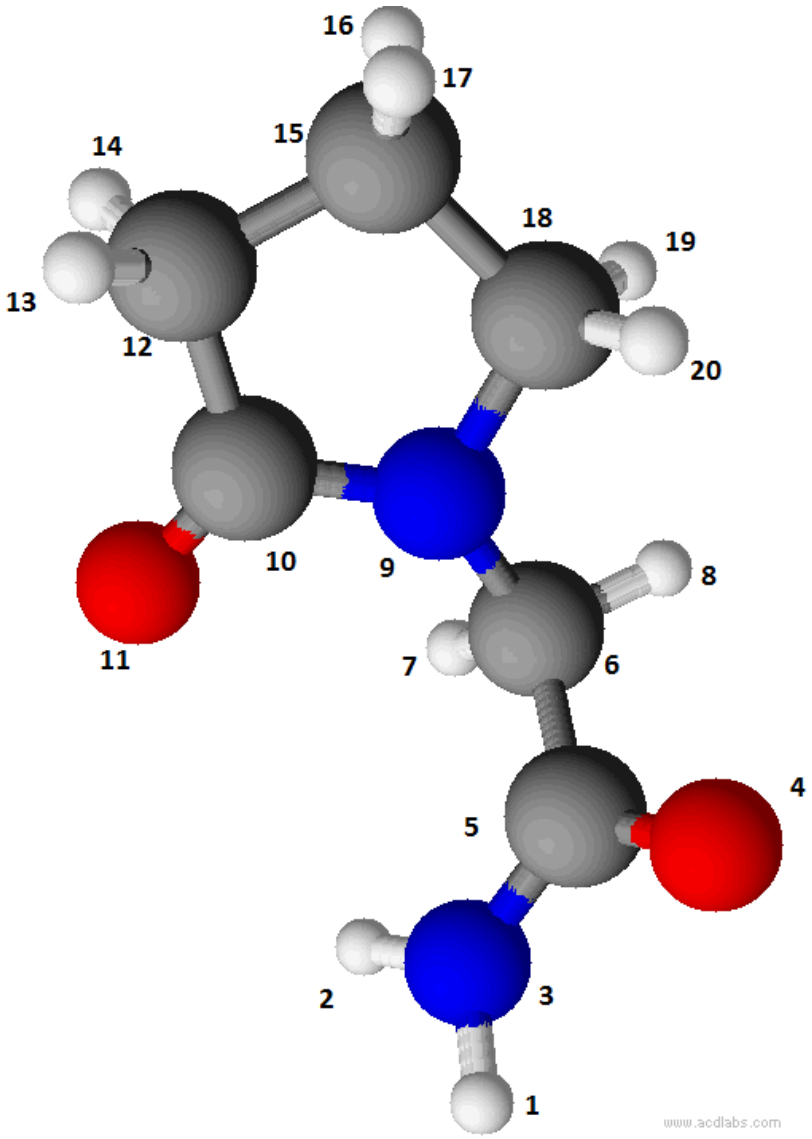

Figure 40 Numerical labelling of atoms present in piracetam and as described in band assignment table overleaf.

Table 21 Assignment of experimental vibrational spectral bands and modes of the calculated vibrations of piracetam. Adapted from ref (246).

V_R / cm^{-1}	Vibrational modes
v_1 42	Lattice mode
v_2 84	Lattice mode
106	($O_4C_5N_3$, $C_6C_5N_3$) ($C_{10}N_9C_6$)
v_3 125	Lattice mode
156	($N_9C_{10}C_{12}$), ($C_{10}N_9C_6$), ($C_{12}C_{10}N_9$, $O_{11}C_{10}N_9$), ($C_{12}C_{10}O_{11}$)
290	($C_{12}C_{10}N_9$), ($C_{12}C_{10}O_{11}$), ($C_{18}N_9C_6$)
342	($N_9C_{10}O_{11}$), ($N_9C_6C_5$), ($C_{18}N_9C_{10}$), ($C_{12}C_{10}C_{11}$)
379	($C_{18}N_9C_{10}$), ($C_{12}C_{10}N_9$), ($C_6N_9C_{10}$), ($C_5C_6N_9$)
503	($N_6C_6H_7$), ($C_{15}C_{12}C_{10}$), ($C_{18}C_{15}C_{12}$), ($C_{12}C_{10}O_{11}$), ($C_5N_9C_6$)
520	($O_4C_5C_6$), ($O_4C_5N_3$), ($C_5N_3H_2$)
550	($O_{11}C_{10}N_9$), ($O_{11}C_{10}C_{12}$), ($N_9C_6H_7$), ($N_9C_6H_8$)
610	($N_9C_6H_7$), ($N_9C_6H_8$), ($C_5C_6H_8$), ($C_5C_6H_7$)
715	($C_{15}C_{18}H_{20}$), ($C_{15}C_{18}H_{19}$), ($N_9C_{18}H_{20}$), ($N_9C_{18}H_{19}$)
729	($H_{14}C_{12}C_{15}$), ($H_{14}C_{12}C_{10}$), ($C_{10}N_9$), ($C_{12}C_{10}$), ($C_{15}C_{18}$)
807	($H_{13}C_{12}C_{15}$), ($H_{13}C_{12}C_{10}$), ($H_{17}C_{15}C_{12}$), ($H_{16}C_{15}C_{12}$)
845	**(C_6C_5), (C_5N_3), ($H_{14}C_{12}C_{15}$)**
861	**($C_{10}N_9$), (C_5N_3), ($C_{12}C_{10}$), (C_6C_5), ($H_{13}C_{12}C_{10}$)**
922	($C_{15}C_{18}$), ($H_1N_3C_5$), ($H_2N_3C_5$)
946	($H_1N_3C_5$), ($H_2N_3C_5$)
1025	($C_{12}C_{10}$), ($H_{14}C_{12}C_{10}$), ($H_{14}C_{12}C_{15}$), ($C_{12}C_{15}$)
1070	($C_{12}C_{15}$), ($H_{13}C_{12}C_{15}$), ($C_{10}N_9$), ($H_{14}C_{12}C_{10}$)
1136	($H_{13}C_{12}C_{10}$), ($H_{14}C_{12}C_{10}$), ($H_{13}C_{12}C_{14}$), ($H_{14}C_{12}C_{15}$)
1190	($H_7C_6C_5$), ($N_9C_6H_7$)
1220	($H_{16}C_{15}C_{12}$), ($H_{17}C_{15}C_{12}$), ($C_{18}C_{15}H_{16}$), ($C_{18}C_{15}H_{17}$)
1305	($C_{12}C_{15}$), ($C_5N_3H_1$), ($C_5N_3H_2$), ($N_9C_6H_8$)
1408	**($H_1N_3H_2$), (C_5N_3), (N_9C_6), (C_5C_6), ($H_7C_6C_5$), ($H_8C_6C_5$)**
1430	**($H_{19}C_{18}H_{20}$), ($C_{15}C_{18}H_{20}$), ($C_{15}C_{18}H_{19}$)**
1445	**($H_{16}C_{15}H_{17}$), ($H_{16}C_{15}C_{12}$), ($H_{17}C_{15}C_{12}$)**
1470	**($H_7C_8H_8$), ($N_9C_6H_7$), ($N_9C_6H_8$)**
1498	**($C_{18}N_9$), ($C_{15}C_{18}$), ($H_7C_6H_8$)**
1645	(C_5O_4)
1660	($H_{13}C_{12}H_{14}$), ($H_{13}C_{12}C_{15}$), ($H_{14}C_{12}C_{15}$)
1677	($C_{10}O_{11}$)
2750	($C_{12}H_{13}$), ($C_{12}H_{14}$)
2810	($C_{18}H_{19}$), ($C_{18}H_{20}$)
2840	(C_6H_7), (C_6H_8)
2886	($C_{15}H_{16}$), ($C_{15}H_{17}$)
2926	($C_{15}H_{16}$), ($C_{15}H_{17}$)
2960	(C_6H_8), (C_6H_7)
2997	($C_{18}H_{19}$), ($C_{18}H_{20}$)
3130	($C_{12}H_{14}$), ($C_{12}H_{17}$)
3340	(N_3H_1), (N_3H_2)

6.3 Near infra-red spectroscopy of piracetam

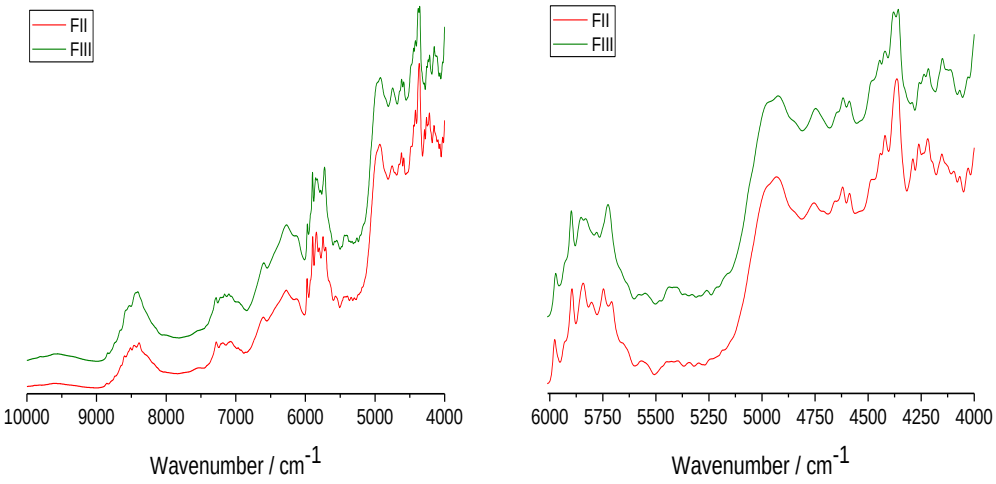

Figure 41 NIR spectra of piracetam polymorphs. Top left, Excipient spectra; top right, polymorph spectra; and bottom an expanded view of the 6000 – 4000 cm^{-1} spectral region.

NIR spectra of the two polymorphs show some differences in the 5870–5600 cm^{-1} and 4314–4080 cm^{-1} spectral regions as can be seen in Fig. 41 above. FIII has a characteristic single peaks at 5724 cm^{-1} and a peak split at 4364 cm^{-1}, while FII distinguishable features with two peaks present at 5748 and 5708 cm^{-1} and a further two peaks present at 4380 and 4358 cm^{-1} in its pure spectrum. These regions are related to CH and CH_2 overtones which differ between the polymorphs as different strains are present due to either polymorph. This can be seen in the Raman spectra of the polymorphs in Fig. 37 in the 2900–3150 cm^{-1} spectral region where the polymorphs feature differences in band shifts and peak intensities as a result of different packing arrangements within their respective crystal structures.

7 A comparative study of the use of powder X-ray diffraction, Raman and near infra-red spectroscopies for the quantification of binary polymorphic mixtures of piracetam

7.1 Introduction

Production of an alternate polymorph can impact the efficacy of a drugs performance in vivo as well as during processing and manufacturing operations. Quantification of an alternate polymorph in the presence of the desired polymorph is an area of concern for pharmaceutical researchers.(126, 247) ICH Q6A proposes surveillance of the polymorph form during stability testing of the drug product in two instances, a) where the efficacy of the product is related to the API form present, and b) performance testing such as HPLC assays cannot reveal the presence of a polymorph conversion.(64) Detection of low levels of an undesired solid state form present in a formulation is required from a quality assurance point of view, given that bioavailability can be affected by polymorphism.

The aim of this chapter is to quantify binary mixtures of piracetam polymorphs using NIR, Raman and PXRD in combination with multivariate methods and demonstrate the efficacies of each technique for this challenge. A simple univariate model was developed by colleagues in the University of Limerick for quantification of binary polymorphs and this was compared to multivariate models developed in this thesis.*

*The author of this work discloses that all binary mixtures were prepared by colleagues in UL. These samples were analysed by PXRD in UL by the collaborator. All physical samples were couriered to NUI Galway for spectroscopic analysis. PXRD data was shared between the collaborators from which the multivariate models reported in this chapter were produced.

7.1.1 Data analysis and spectral regions of interest

A selection of pre-processing methods were used to enhance spectral signals of interest and these included Multiplicative Scatter Correction (MSC), standard normal variate (SNV), first and second derivatives and their combinations were applied for Raman and NIR data. Savitzky–Golay first and second order derivatives were performed using a window size of 15 points and a second order polynomial. Mean normalization was used for PXRD data. The PXRD and spectroscopic data were subjected to mean centring prior to partial least squares (PLS) analysis. The optimal number of PLS factors was then determined by using a leave–one–out cross validation procedure. Regions of interest as detailed in Table 22 were selected for model generation as they contained the majority of differences between the polymorphs.

Table 22 Regions of interest selected for model generation using PXRD, NIR and Raman data.

Technique	Name	Regions of interest
PXRD	Full	10.01–34.98 2θ
	A	15.14–26.07 2θ
	B	15.14–21.00 & 22.79–26.07 2 θ
NIR	Full	10000–4000 cm^{-1}
	Half	6000–4000 cm^{-1}
	A	6000–5600 cm^{-1}
	B	4314–4080 cm^{-1}
	A and B	6000–5600 & 4314–4080 cm^{-1}
Raman	Full	250–3310 cm^{-1}
	Half	250–1730 cm^{-1}
	A	454–1730 cm^{-1}
	B	454–1534 cm^{-1}
	C	1370–1730 cm^{-1}
	D	2770–3034 cm^{-1}
	E	250–402 cm^{-1}
	F	678–1518 cm^{-1}

7.1.2 Multivariate powder X-ray diffraction analysis

PLS regression was performed making use of discrete regions of interest including the 15.1–21.0 and 22.8–26.1 2θ ranges, excluding the reflection around 21.3 and 21.7 2θ which exhibited intensity variation due to preferred orientation effects due to FIII.

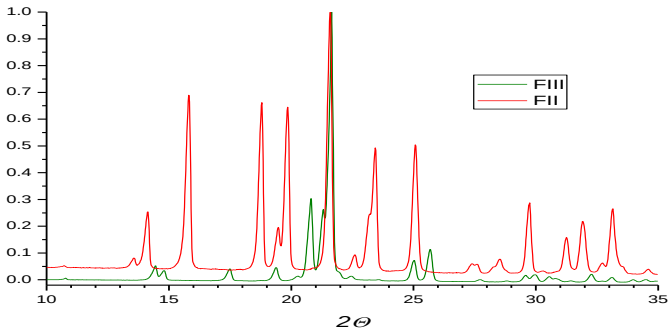

Figure 42 PXRD patterns of FII and FIII piracetam, normalised and partially offset.

During the PLS regression analysis, 45 PXRD scans were used from 15 calibration samples. Mean normalisation was used for pre-processing of the PXRD diffraction patterns.

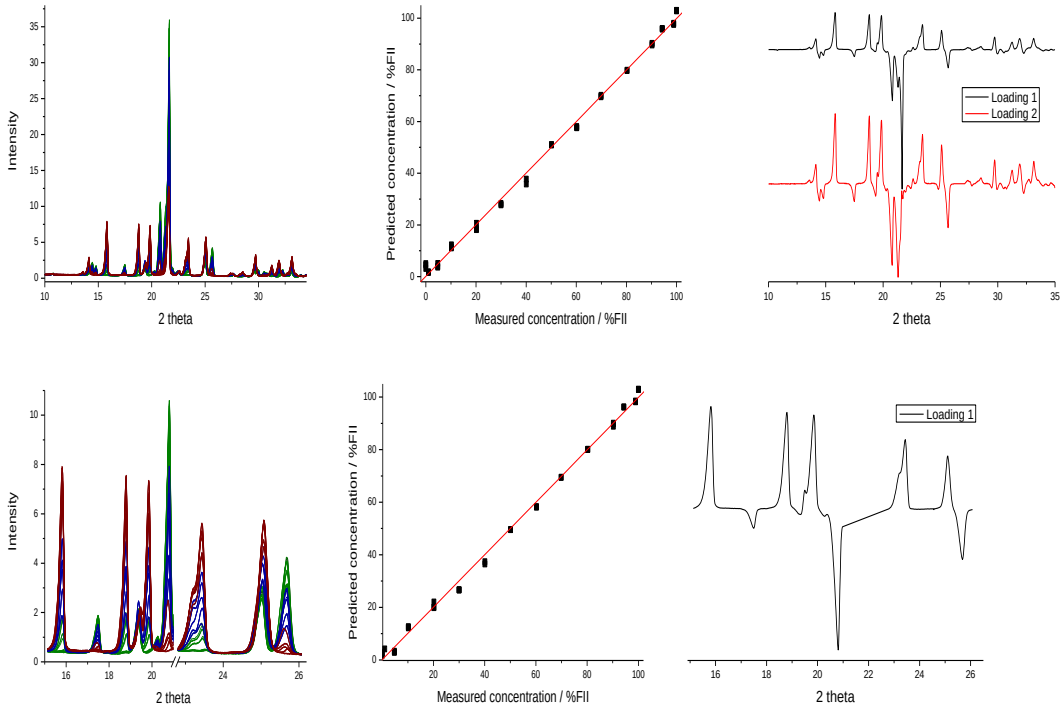

Figure 43 Top left, mean normalised PXRD pattern; top middle, measured vs. predicted FII piracetam concentration plot; top right, loadings of PLS model; bottom left, mean normalised pattern excluding peaks known to show preferred orientation effects; bottom middle, measured vs. predicted FII piracetam concentration plot; bottom right, loading of this PLS model.

The best calibration model was achieved for the quantification of FII by use of the aforementioned range in combination with mean normalisation. A correlation coefficient (R^2) of 0.997 was achieved by this model of one latent variable which

was due to the change in concentration to FII present in the samples, with RMSEC and RMSEP values of 2.07 and 1.81% FII respectively. These values, particularly the RMSEC and RMSEP values, are a marked improvement on those generated by the univariate data analysis using either peak height intensity or peak area. Since the majority of information pertaining to both polymorphs was contained within the 15.1–21.0 and 22.8–26.1 2θ ranges, utilising all the information from these areas of the diffractogram allows for any subtle changes due to either polymorph present to be taken account. This is a marked contrast to the univariate method which used only two peaks one of which was specific to each polymorph.

Table 23: Performance of the regression models using different pre-processing methods. This data was the NIR spectra collected from the 1 mm thick tablets. RMSE values in % FII.

Pre–processing	Region	LV	RMSEC	R^2	RMSECV	RMSEP
	Full	2	2.03	0.998	2.14	1.56
Mean normalisation	A	2	2.06	0.998	2.19	1.57
	B	1	2.06	0.998	2.17	1.81

7.1.3 Quantitative analysis by Raman spectroscopy

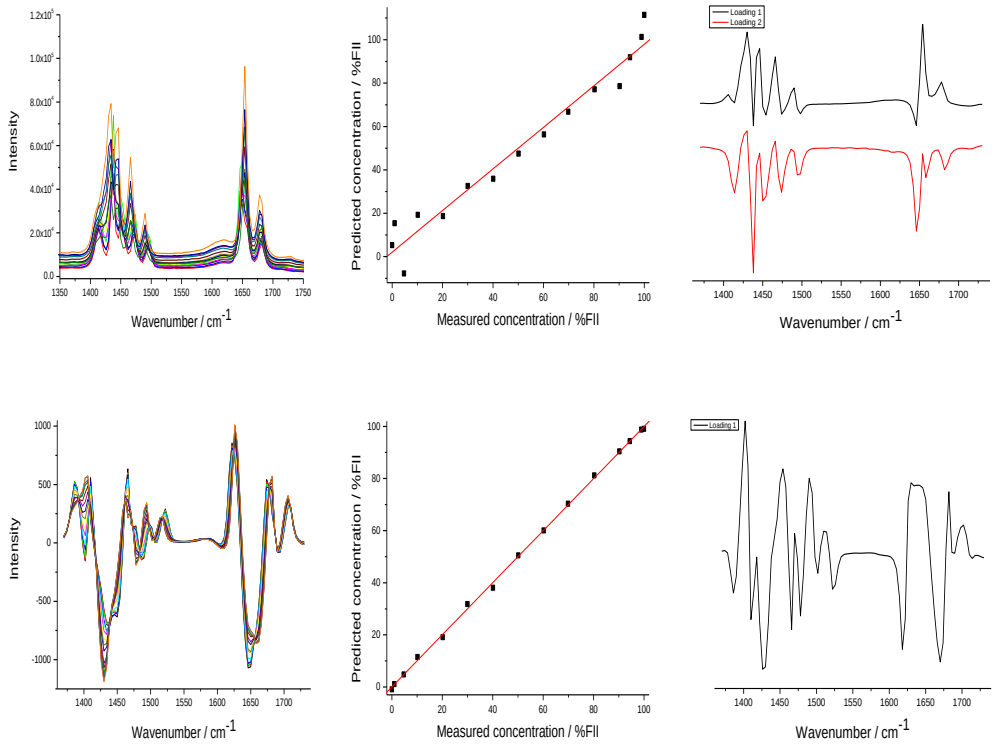

Figure 44 Top left, raw Raman spectra; top middle, measured vs. predicted FII piracetam concentration plot; top right, loadings of PLS model of raw spectra; bottom left, MSC and 2nd derivative pre-processed Raman spectra; bottom middle, measured vs. predicted FII piracetam concentration plot; and bottom right, PC1 loading plot of best performing PLS model.

BRS was used in the entirety of this study. PLS models were generated using full and several discrete spectral regions of interest in combination with a variety of pre-processing methods. These included MSC, SNV, derivatives and their combinations in an effort to reduce noise and information pertaining to instrumental effects and to enhance chemical information. Generation of PLS models based on the spectral region of 1730–1370 cm^{-1} and pre-processed using a combination of MSC and Savitzky-Golay 15 point second polynomial second derivative proved to be the best for quantification of FII in the binary polymorph mixtures. MSC helped eliminate effects of light scattering from the powder mixtures and use of the second derivative accentuated the spectral differences pertaining to each polymorph in the mixtures. The PLS loading of this model (Fig. 44) can be attributed to that of a pre-processed spectrum of FIII however with contributions from FII appearing from 1390–1450 cm^{-1}. The loadings associated with the raw unprocessed data (Fig. 44) suggests that the loadings correspond to FII and FIII separately. A high level of linearity was achieved with the calibration model built using this spectral region and the combination of pre-processing with a correlation coefficient of 0.999. RMSEC and RMSEP values of 0.94 and 1.21% FII were achieved with this model. Using a 95% FIII sample the limit of detection and quantification for Raman analysis was determined to be 1.48 and 4.47% FII respectively.

Table 24 Performance of the regression models using different pre-processing methods for Raman data. RMSE values in % FII.

Pre–processing	Region	PLS Factors	RMSEC	R^2	RMSECV	RMSEP
Raw	Full	2	7.63	0.9777	11.32	6.74
	Half	2	7.33	0.9795	11.36	9.07
	A	2	7.36	0.9793	11.43	9.07
	B	2	7.37	0.9792	11.42	9.04
	C	2	7.40	0.9791	11.39	8.84
	D	2	7.70	0.9773	11.98	8.21
	E	2	7.37	0.9792	11.10	8.82
	F	2	7.47	0.9787	11.49	8.73
MSC	Full	2	0.97	0.9996	1.30	1.64
	Half	1	1.29	0.9994	1.45	3.70
	A	1	1.29	0.9994	1.44	3.37
	B	1	1.32	0.9993	1.48	3.77
	C	1	1.16	0.9995	1.30	1.04
	D	1	1.59	0.9990	1.83	1.67
	E	1	1.36	0.9993	1.55	4.74
	F	1	1.26	0.9994	1.41	3.22
MSC & 2^{nd} deriv.	Full	1	1.31	0.9993	1.49	0.99
	Half	1	1.04	0.9996	1.17	1.36
	A	1	1.03	0.9996	1.16	1.27
	B	1	1.08	0.9996	1.22	1.37
	C	1	0.94	0.9997	1.06	1.12
	D	1	1.85	0.9987	2.09	0.91
	E	1	1.30	0.9994	1.50	2.19
	F	1	1.05	0.9996	1.19	1.47

7.1.4 Quantitative analysis by NIR spectroscopy

NIR spectra of the two polymorphs show strong differences in the 5870–5600 and 4314–4080 cm^{-1} spectral regions and these two spectral regions were combined to construct a PLS model. A combination of MSC and a second derivative pre-processing was applied to generate the best model for quantification of FII using NIR. A linear relationship with a correlation coefficient of 0.999 was observed between the calculated and actual FII content. RMSEC and RMSEP values of 0.99 and 0.64% FII were achieved with this model. Using a 95% FIII sample the limit of detection and quantification for Raman analysis was determined to be 0.84 and 2.56% FII respectively.

Table 25 Performance of the regression models using different pre-processing methods. This data was the NIR spectra collected from the 1 mm thick tablets. RMSE values in % FII.

Pre–processing	Region	LV	RMSEC	R^2	RMSECV	RMSEP
Raw data	Full	3	2.24	0.9981	3.27	6.51
	Half	3	1.57	0.9991	2.13	7.03
	A	2	1.62	0.9990	3.39	5.21
	B	2	1.75	0.9988	2.11	5.62
	A and B	3	1.50	0.9992	2.01	6.39
MSC	Full	1	1.75	0.9988	2.04	2.92
	Half	1	1.55	0.9991	1.79	2.49
	A	1	3.28	0.9959	3.86	4.26
	B	1	1.74	0.9989	1.99	0.61
	A and B	1	1.07	0.9996	1.20	1.13
MSC & 2^{nd} deriv.	Full	1	1.29	0.9994	1.46	1.25
	Half	1	1.41	0.9992	1.61	1.38
	A	1	0.86	0.9997	0.95	0.45
	B	1	1.50	0.9992	1.72	1.01
	A and B	1	0.99	0.9996	1.12	0.64

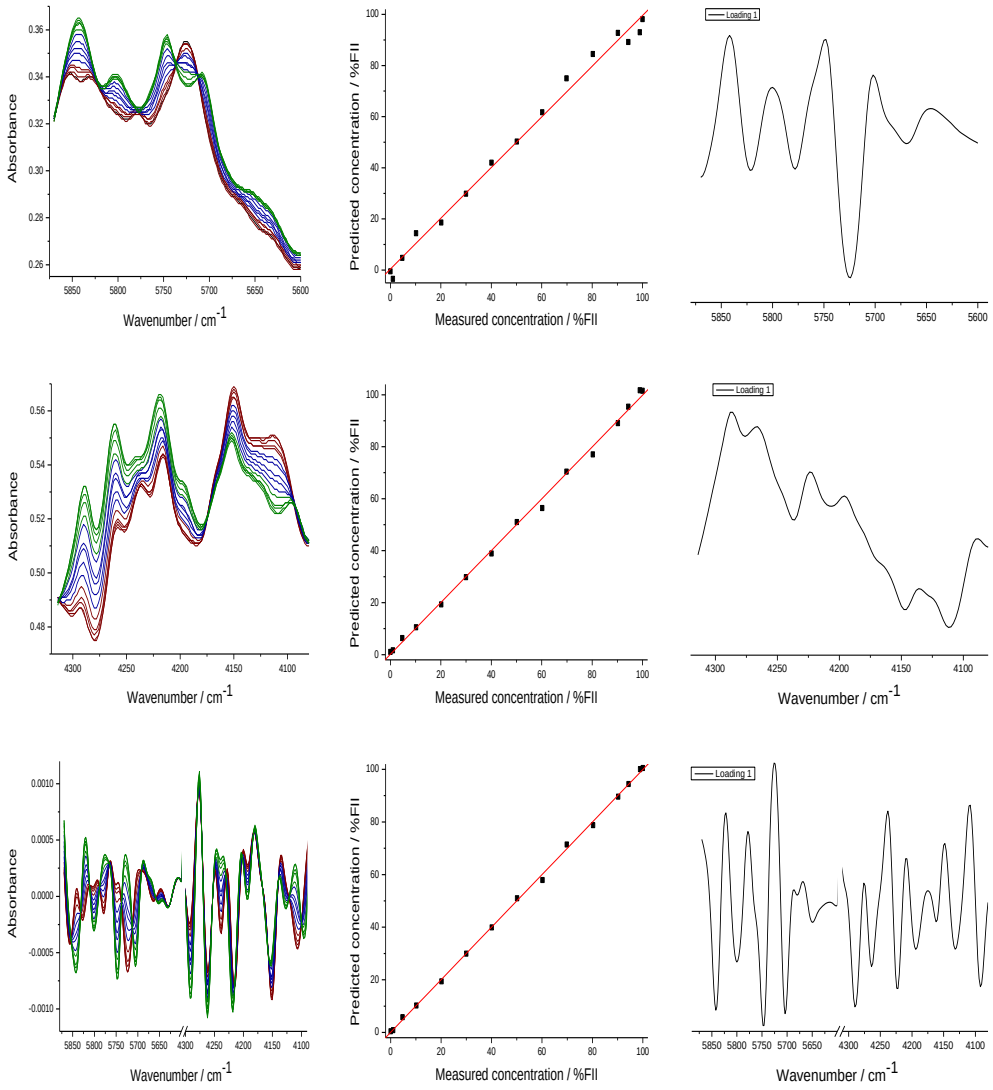

Figure 45 Top left, MSC treated NIR spectra of 6000–5600 cm^{-1}; top middle, measured vs. predicted FII piracetam concentration plot; top right, loading of PLS model for this spectral region; centre left, MSC treated NIR spectra of 4314–4080 cm^{-1}; centre middle, measured vs. predicted FII piracetam concentration plot; centre right, loading of PLS model for this spectral region; bottom left, MSC and second derivative treated NIR spectra of 6000–5600 and 4314–4080 cm^{-1} spectral regions; bottom middle, measured vs. predicted FII piracetam concentration plot; and bottom right, PC loading plots from best performing PLS model

7.2 Discussion

Quantification of binary polymorph mixtures of piracetam was easily achieved using both univariate and multivariate models however with different levels of accuracy. PXRD is considered to be the classical reference method for the characterisation of solids. While PXRD could readily detect both polymorphs, quantification of the binary mixtures was a challenge due to peak height intensity variation due to preferred orientation effects – most evident at peaks around 21.3 and 21.7 2θ on inspection of theoretical and actual diffraction patterns. Univariate data analysis by UL is presented in Table 26 and a full discussion is presented in the aforementioned published work which is included in an appendix at the back of this thesis.(236)

Table 26 Performance of the regression models for quantification of FII piracetam in binary polymorph mixtures using varying analytical techniques. (217)

Methods	Pre–processing	R^2	Latent Variables	RMSEC (%)	RMSECV (%)	RMSEP (%)
PXRD (Peak Area)	without K	0.9824	–	4.58	–	6.71
	with K	0.9892	–	3.57	–	8.13
PXRD (Peak Intensity)	without K	0.9774	–	5.20	–	4.64
	with K	0.9927	–	2.94	–	1.91
PXRD (PLS)	mean normalization	0.9968	1	2.07	2.17	1.81
Raman (PLS)	MSC and 2nd Derivative	0.9993	1	0.94	1.06	1.21
NIR (PLS)	MSC and 2nd Derivative	0.9993	1	0.99	1.11	0.64

Despite using a response factor K to account for differences in peak height intensity or areas, univariate models built using the response factor did not perform as well as a multivariate method built using a greatly increased portion of the diffraction pattern, from 15.1–21.0 and 22.8–26.1 2θ range. A higher degree of linearity was achieved using the multivariate model when the data was pre-processed using mean normalisation. Mean normalisation normalised the varying peak intensities which were partly due to preferred orientation effects associated with FIII.

The vibrational spectroscopic methods showed an improvement in accuracy in comparison to PXRD PLS models as highlighted by the increase in correlation coefficients to 0.9993 and the large decreases in RMSEC and RMSEP values. Raman spectroscopy easily distinguished both polymorphs, showcasing the many subtle differences between the polymorphs. NIR spectral data interpretation was not as straight–forward due to the fact that NIR is based on the combination and overtone modes of fundamental molecular vibrations which are difficult to assign. For both Raman and NIR models, the pre-processing combination of MSC and a second derivative gave the best quantitative models overall. The spectroscopic methods in combination with multivariate methods exhibit lower RMSE values than those associated with either PXRD models.

Table 27 Comparison of the three techniques for the quantification of % FII in validation samples. (217)

% FII in Sample	PXRD (Univariate)	PXRD (PLS)	Raman (PLS)	NIR (PLS)
15.12	18.02	16.95	14.53	14.59
24.58	25.74	25.57	25.10	24.79
49.95	52.01	47.69	51.26	49.14
74.95	74.20	76.86	76.59	74.13
LOD	0.88	0.75	1.48	0.84
LOQ	2.68	2.26	4.47	2.56

Validation of the different models generated for each technique was carried out by testing each model with the external test set and seeing how accurate each predicted result was to the known composition values. One sample was prepared at each of the stated % FII amounts in Table 27, analysed in triplicate and then placed into the appropriate models for quantitation. For lower content samples, Raman and NIR PLS models predict the most accurately with the multivariate PLS PXRD model next and the univariate PXRD model performing the worst. In the majority of cases the PXRD models overestimate the FII content and this may well be related to preferred orientation effects in the samples despite the great care taken in sample preparation to minimise this. Overall NIR gives the most accurate prediction of the validation samples with the lowest LOD and LOQ.(236)

For this type of quantitative work sample heterogeneity is of great importance. Colleagues in UL made use of a 90–125 μm sieve fraction and sample rotation throughout PXRD analysis was employed.(236) For Raman analyses a 3 × 3 mapping grid of 9 spectral points was employed. The Raman system had a sampling spot size of ~ 200 μm in diameter. All Raman spectra were then averaged before data analysis was performed. NIR analysis was performed in glass vials with a sampling area of 15 mm. Each sample was analysed in triplicate by NIR and Raman. Raman is particularly sensitive to sample inhomogeneity, the relative standard deviation values of quantification of the 95% FII sample obtained from the averaging of nine spectra and from individual spectra were 6.22 and 58.81% respectively. Increasing sampling volume by use of the 3 × 3 mapping grid reduced the errors associated with sub–sampling by a factor of 9.5.

7.3 Chapter conclusions

Binary polymorphic mixtures of piracetam were analysed quantitatively using Raman and NIR spectroscopy, coupled with multivariate analysis of the spectroscopic data and PXRD patterns. Multivariate analysis of PXRD diffraction patterns in this case proved more accurate and reliable than use of a simple univariate method based on peak height intensity or area ratios of unique peaks characteristic from either polymorph. Use of a wider range of data points by including more of the diffraction pattern pertaining to the chemical information in this system is useful and clearly demonstrated by the improved error values reported. However, despite the effects of preferred orientation attributed to the FIII polymorph being greatly reduced by pre-processing the diffraction patterns by mean normalization, the multivariate PXRD models did not have comparable accuracy or limits of detection or quantification that the multivariate spectroscopic models do.

Multivariate analysis of the Raman and NIR spectroscopic data in combination with pre-processing yielded models of higher linearity and accuracy of prediction of validation samples when compared to the PXRD models. In all cases the use of pre-processing greatly enhanced the spectral chemical information of the binary polymorph mixtures.

8 Quantitative polymorph contaminant analysis in piracetam loaded tablets using Raman and near infra-red spectroscopies

8.1 Introduction

Incidences of unwanted polymorphism in pharmaceutical products have been widely reported and can have major ramifications such as that of Ritonavir discussed in the introductory chapter.(26, 27, 248) Cases detailing the analysis of formulations where quantification of a polymorphic or alternate solid state form contaminant are few in the literature.(65, 249-251) This chapter concerns the determination of the efficacies of rapid spectroscopic methods for a model tablet formulation consisting of 10:10:90% w/w API: calcium carbonate: microcrystalline cellulose. The model API used here is piracetam and its polymorphism is discussed in Chapter 6 and 7. Piracetam FII and FIII, are used in varying ratios in this model formulation where FII is considered to be the polymorphic contaminant. The aim of this study is to quantify levels of polymorphic contaminant down to 0.1% of the tablet using NIR, backscattered Raman, and transmission Raman spectroscopies in combination with selected pre-processing methods and PLS regression models.

8.2 Solid state polymorphic transformation of FIII to FII monitored using Raman spectroscopy

FII was prepared by first heating FIII to 140°C, generating FI as determined by PXRD which once cooled to room temperature begins to rapidly transform into FII.(252, 253) The PXRD pattern of FI matched that already published and there are clear differences in its Raman spectrum when compared to the FII and FIII spectra however to our knowledge no Raman spectrum of FI has been presented previously.(35, 36, 207, 225, 226, 241, 244, 245, 254-256)

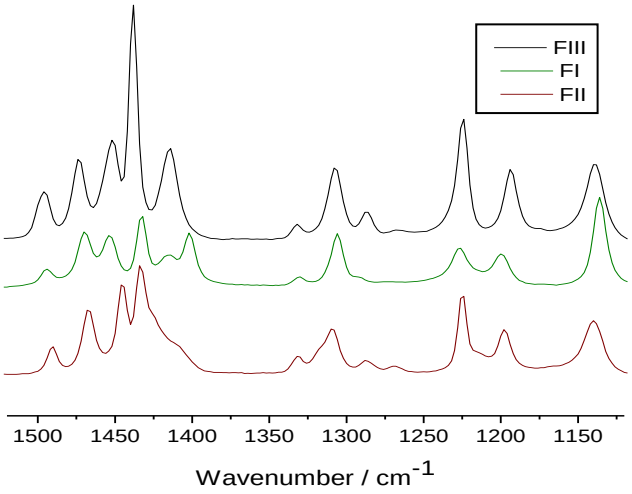

Figure 46 Raman spectra of FI, FII and FIII piracetam polymorphs.

BRS was used to monitor this transformation at 24 hour intervals starting before the FIII sample was heated. It appeared that the FIII to FI solid state transformation was complete after 24 hours of heating while the FI to FII transformation was complete 24 hours after removal of the FI form from the oven (Fig. 46 and 47). Significant differences between all three polymorphs are evident between 1390 and 1510 cm^{-1} arising from band shifting and a band shape change is noted at 1230 cm^{-1} in all polymorphs due to changes in the bond lengths and angles made by atoms adjacent to the carbonyl groups. See Table 21 and Section 6.2 for a fuller description of the band assignments for the various polymorphs.

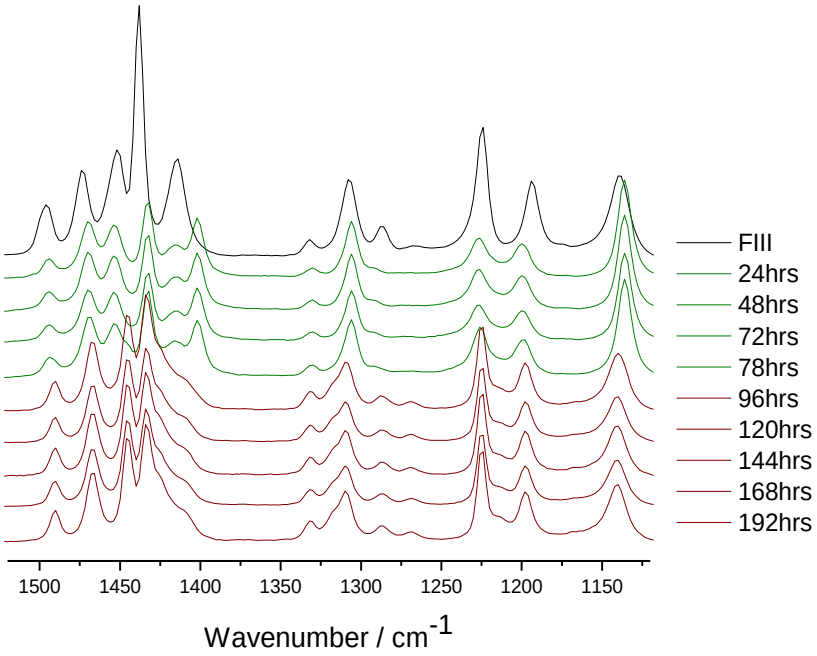

Figure 47 Raman spectra collected at different time points during the solid–state transformation of FIII to FII; Black represents starting material at room temperature, green represents samples that were heated in the oven at 140°C and red represents samples after removal from oven.

PCA scores plot of the Raman data (Fig. 48) showed very clear differences between all three polymorphs with no overlap of the sample cluster 95% ellipses. There is good separation of all samples pertaining to each polymorphic form which is as expected considering the spectral differences between the polymorphs evident in the Raman spectra as shown above. In the PCA plot there is variation within the samples corresponding to FII after removal from the oven. On inspection of the corresponding Raman spectra, it is noticed that the longer FII is removed from the oven, the sharper the bands become which may indicate increasing crystallinity of FII. FII samples were used for tablet incorporation after a week of storage at room temperature to ensure it was stable for inclusion.

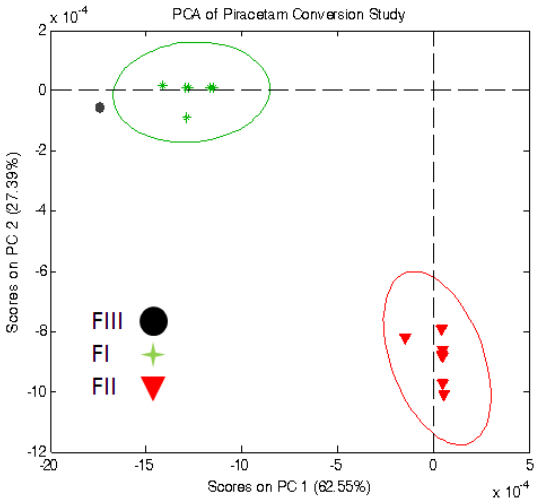

Figure 48 PCA scores plot of Raman spectra collected at different time points during the solid–state transformation of FIII to FII. Black represents starting material at room temperature, green represents samples that were heated in the oven at 140°C and red represents samples at room temperature after oven heating.

PXRD diffraction patterns and DSC thermograms of the FII and FIII polymorphs were compared to previously published data and confirmed that the pure forms of FII and FIII polymorphs had been generated with no impurities detectable, Fig. 49.(252, 257) As shown in the DSC thermograms the two polymorphs share an endothermic peak at 152°C due to the melting of Form I which is formed at 114 and 120°C as indicated by endothermic peaks for FII and FIII respectively.

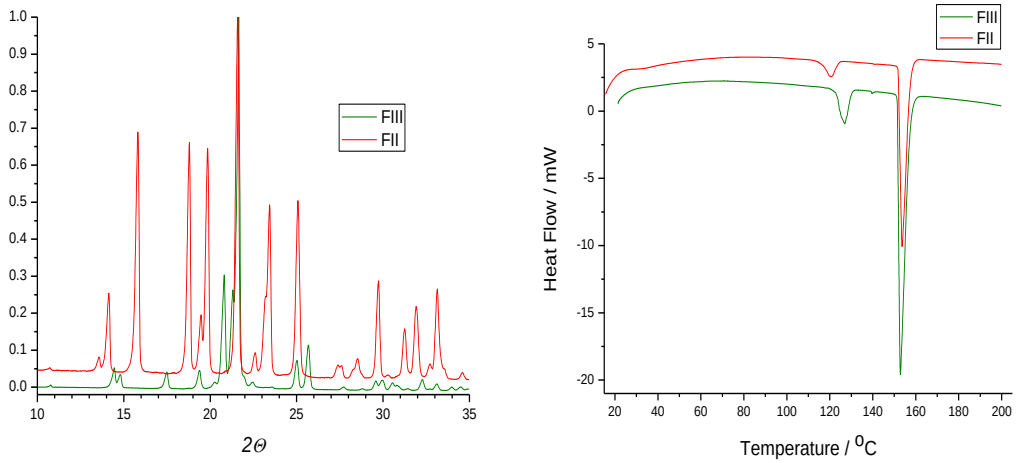

Figure 49 Left: Normalised (& slightly offset) PXRD patterns of the pure FIII(green) and FIII(red) piracetam polymorphs. Right: DSC thermograms of Piracetam Form III (green) and FII (red).

8.3 Qualitative analysis of polymorphs and excipients

8.3.1 Raman spectroscopy

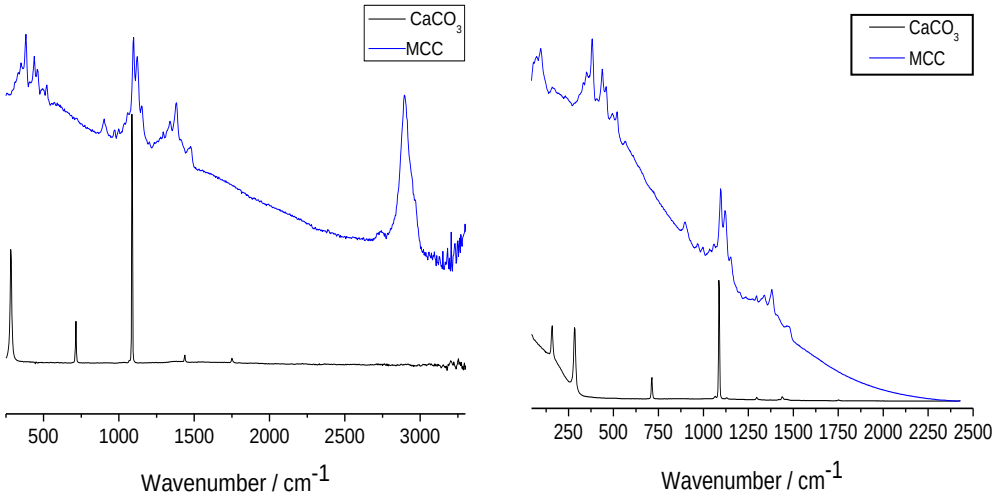

Figure 50 Raman spectra of excipients, left BRS, right TRS.

Fig. 50 shows the BRS and TRS spectra of the tablet components. Both sets of Raman spectra show sharp, well resolved bands which allow for facile observation of spectral differences between all components. MCC exhibits a sloping baseline with several bands in the 850–1500 cm^{-1} spectral region which are due to *v*(C–O) and *v*(C–C) stretching vibrations and δ(CH_2) deformations.(231-235) There are also peaks present at 380 and 460 cm^{-1} which are due to δ(CCC), δ(CO) and δ(CCO) bending vibrations and ring deformations.(236) A band at 1093 cm^{-1} is characteristic of unsubstituted cellulose rings which are found in MCC.(231) The most noticeable aspect of the MCC Raman spectra are the very large sloping baseline signal which is virtually the same for BRS (785 nm) and TRS (830 nm). We postulate that it may be related to diffuse or Mie scattering of the 20 μm MCC particles. Bonnier *et al.* have noted this that for small particles the diffusely scattered radiation is not collimated and this leads to the excitation signal dispersion across the spectrometer's CCD.(258)

The Raman spectrum of calcium carbonate has three strongly intense and sharp peaks in the BRS spectra at 281 cm^{-1} corresponding to the translational lattice mode, 711 cm^{-1} due to the v_4 – symmetric CO_3 bending deformation and 1084 cm^{-1} to the v_1 CO_3 symmetric stretch which are attributable to carbonate.(67)

8.3.2 Near infra-red spectroscopy

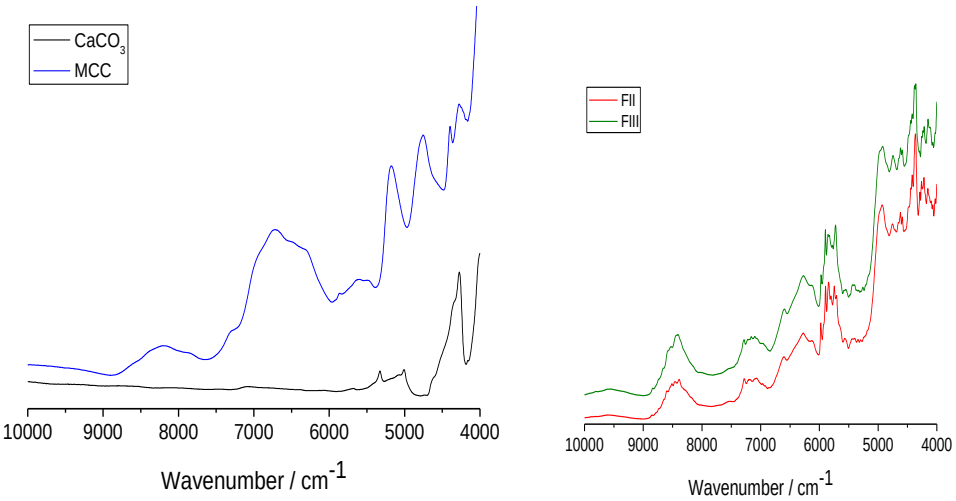

Figure 51 NIR spectra of pure tablet components. Left, excipients, right, piracetam polymorphs.

The NIR spectrum of calcium carbonate exhibits a relatively featureless spectrum with a peak at 4300 cm^{-1} whereas microcrystalline cellulose displays a large broad peak at 6800 cm^{-1} and several broad peaks in the 5300–4000 cm^{-1} region due to CH and CH_2 overtones.(230) NIR spectra of the two polymorphs show some differences in the 5870–5600 and 4314–4080 cm^{-1} spectral regions as can be seen in above and discussed previously in Chapter 6, Section 3.

8.4 Qualitative analysis of tablets

8.4.1 Raman spectroscopy

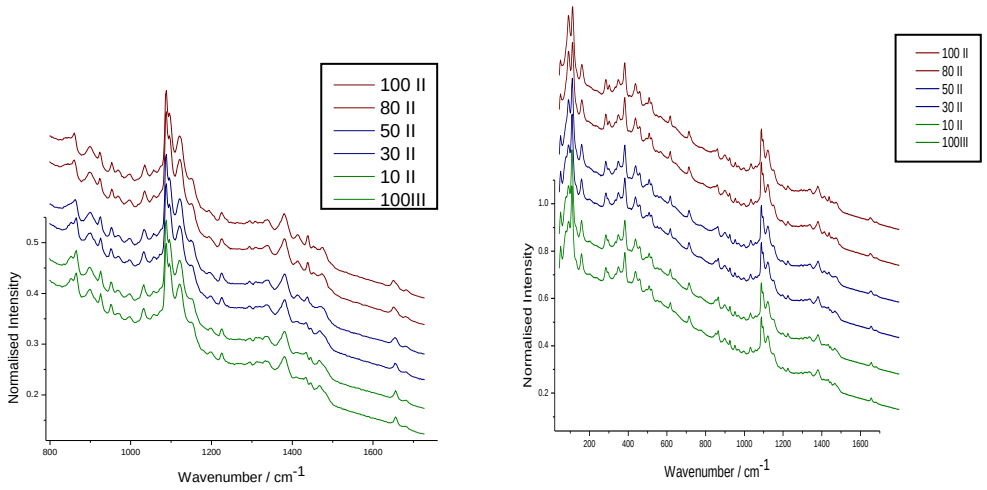

Figure 52 Raman spectra of 0, 10, 30, 50, 70, 90, 100 % FII tablets; Left, BRS; and right, TRS.

In the raw Raman spectra of tablets MCC dominates with a large sloping baseline in both the BRS and TRS spectra (Fig. 52). However despite this large contribution by MCC, much of the Raman band detail is clearly visible and it is comparatively easy to identify bands due to each of the polymorphs. The majority of polymorph characteristics are noticeable in the 800–1750 cm^{-1} region which contains unique features such as the Amide I band at 1650–1680 cm^{-1} which differ in the two polymorphs plus other band position differences as detailed in Section 6.2, Raman spectroscopy of piracetam.

8.4.2 Near infra-red spectroscopy

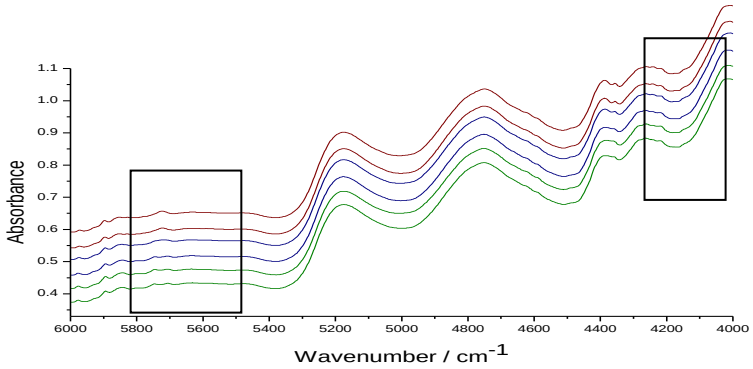

Figure 53 NIR spectra of 0, 10, 30, 50, 70, 90, 100 % FII tablets – from top to bottom

Microcrystalline cellulose displays several broad peaks in the 5300–4000 cm^{-1} region. NIR spectra of the tablets strongly feature MCC characteristics which is the main tablet constituent. The calcium carbonate is unidentifiable from the multi–component spectra. Differences in polymorphic mixture composition are rather subtle on initial inspection as they are obscured by the MCC. The polymorphic characteristics as mentioned previously are observable in the 6000–5600 and 4320–4080 cm^{-1} spectral regions due to CH and CH_2 overtones as discussed in Section 6.4, Near infra-red spectroscopy of piracetam.

8.5 Spectral regions of interest

Specific spectral regions of interest were selected for use in multivariate analysis. By doing so specific spectral regions where differences in polymorphic composition were known to occur in the raw component spectra could be utilised. Additionally regions where there was little to no information such as that above 1800 cm^{-1} in the TRS spectra could be eliminated from the multivariate analysis. This increased the speed of analysis.

Table 28 Regions of interest selected for chemometric modelling of the NIR and Raman spectra collected from the PiraTabs samples.

Technique	Name	Wavenumber region / cm^{-1}
NIR	Full	10000–4000
	Half	6000–4000
	A and B	6000–5600, 4314–4080
	A	6000–5600
	B	4314–4080
Backscattered Raman	Full	250–3300
	Half	250–1730
	A	1350–1730
	B	802–1730
Transmission Raman	Full	44–2450
	Half	44–678
	A	1370–1730
	B	801–1730
	C	44–250

8.6 Spectral pre-processing

The differences between the spectra pertaining to high and low levels of FII are subtle as is shown in the Fig. 54. To amplify the variations between the polymorph mixtures a second order derivative was used. Spectral differences and those regions pertaining to polymorph composition changes show large, sharp peaks meaning that there is a high level of change in this spectral region which is due to the changing FII concentration. Examples of this include the 6000–5600 cm^{-1} spectral region in NIR spectra and the 1400–1450 cm^{-1} spectral region in Raman spectra. This is to be expected as there are obvious differences between the polymorphs in their pure spectra at these regions and it would be expected that these changes would still be present in the tablets though they are less obvious and are more subtle due to the lower concentrations of polymorphs present. Normalisation by use of MSC was also utilised to account for baseline offsets.

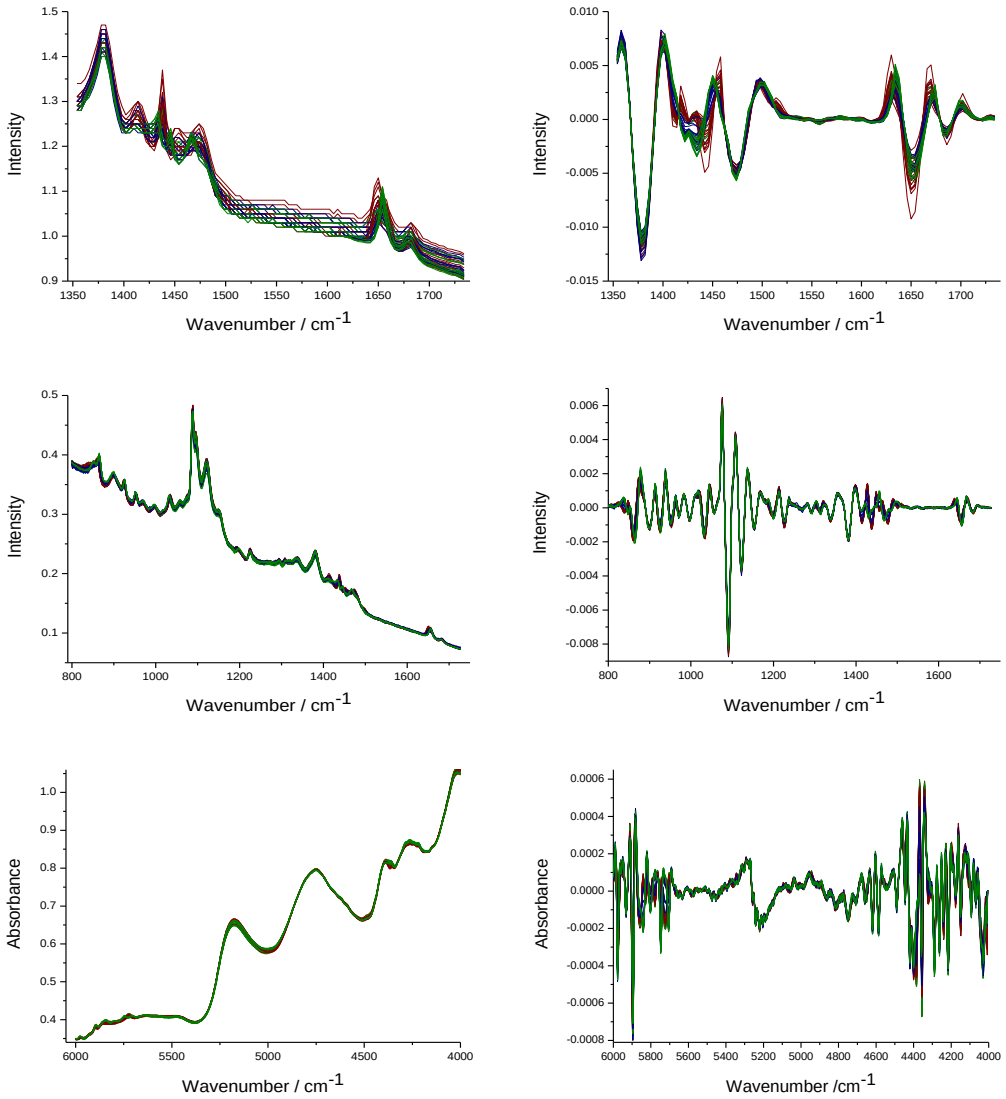

Figure 54 Effect of pre-processing of spectral data of PiraTabs. First column, MSC treated spectra; and second column, combination of MSC and a second derivative treated data. Top row, BRS spectra; middle row, TRS spectra; and final row, NIR spectra. Red spectra represent the tablets of low FII concentration and the green spectra represent tablets of high FII concentration.

8.7 Quantitative analysis

8.7.1 BRS PLS models of 1 mm PiraTabs

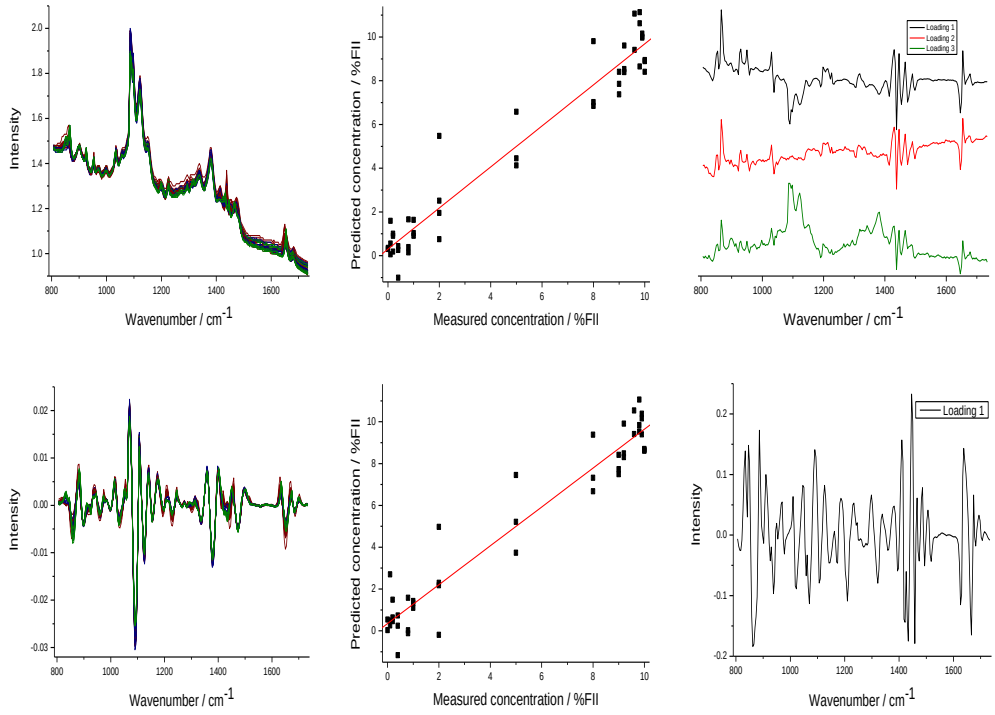

Figure 55 Top left, MSC pre-processed BRS spectra; center middle, measured vs. predicted FII piracetam concentration plot; center right, loadings of PLS model of MSC pre-processed data; bottom left, MSC and 2nd derivative pre-processed BRS spectra; bottom middle,

Table 29 Performance of the regression models using different pre-processing methods for 1 mm BRS spectra. RMSE values in % w/w.

Pre–processing	Region	LV	RMSEC	R^2	RMSECV	RMSEP
Raw data (*norm.*)	Full	4	1.04	0.969	1.29	2.50
	Half	3	1.01	0.970	1.20	2.75
	A	3	1.06	0.968	1.20	2.62
	B	3	1.04	0.969	1.21	2.37
MSC	Full	4	1.03	0.969	1.27	2.62
	Half	3	1.02	0.970	1.18	2.59
	A	3	1.07	0.967	1.21	2.75
	B	3	1.03	0.969	1.18	2.52
MSC & 2^{nd} deriv.	Full	1	1.08	0.967	1.17	2.40
	Half	1	1.14	0.963	1.19	1.92
	A	2	1.07	0.967	1.16	2.65
	B	**1**	**1.11**	**0.965**	**1.16**	**2.11**

Results of PLS models built using BRS spectral data are presented in Table 29. In all PLS models built using BRS data there was a large degree of scatter as can be seen in the low correlation coefficient values. PLS models generated using normalized BRS spectra which were then subsequently MSC pre-processed showed little differences in their RMSE values and number of latent variables. The three latent variables represent the MCC baseline as the primary loading with subsequent loadings due to the polymorphic forms. This can be seen in the raw loadings plot where the green loadings plot strongly features the band at 1093 cm^{-1} which is characteristic of the MCC unsubstituted cellulose rings.(231)

Combination of the MSC treated spectra with a second derivative results in highlighting the differences between the tablets of varying FII concentration levels as can be observed above in Fig. 55. PLS models generated utilising this combination of pre-processing results in PLS models of one latent variable, with similar correlation coefficients but slightly improved RMSE values. The best performing BRS model for quantitation made use of the 802–1750 cm^{-1} spectral region which encompasses the majority of spectral differences between the two polymorphs which include differences around 1410 cm^{-1}.

As can be seen in the Table 29 all models have relatively high RMSEP values indicating that the models poorly predicts the external prediction set as shown by the almost double in value number generated for RMSEP when compared to RMSEC. This is probably as a result of sub-sampling. A 200 µm spot size was employed by the BRS system and a 16 point mapping grid was utilized to collect spectra from the tablet surface. This would mean that if there was a high level of surface inhomogeneities where the laser hit the tablet surface this could result in increased errors associated with the PLS models. For illustration the spectra associated with the FII50 sample are plotted below in Fig. 56. One can see from the normalized and second derivative regression model plots above in Fig. 55 there is high variation between these spectra. When reviewing the raw spectral data as shown below one observes quite a difference in baseline amongst all three replicates. On normalization using MSC the spectra still show some evidence of baseline differences as well as a lack of band sharpness particularly from 1400–1500 cm^{-1} where all three show differences in terms of FII and FIII present. This carries through to the second

derivative spectra with other differences evident and highlights the lack of representativeness achieved with BRS despite use of a point mapping grid. Use of a more extensive mapping grid size giving a greater surface sampling area could be used in an attempt to improve the errors and the correlation factor of the PLS models however this would result in a greater time penalty.

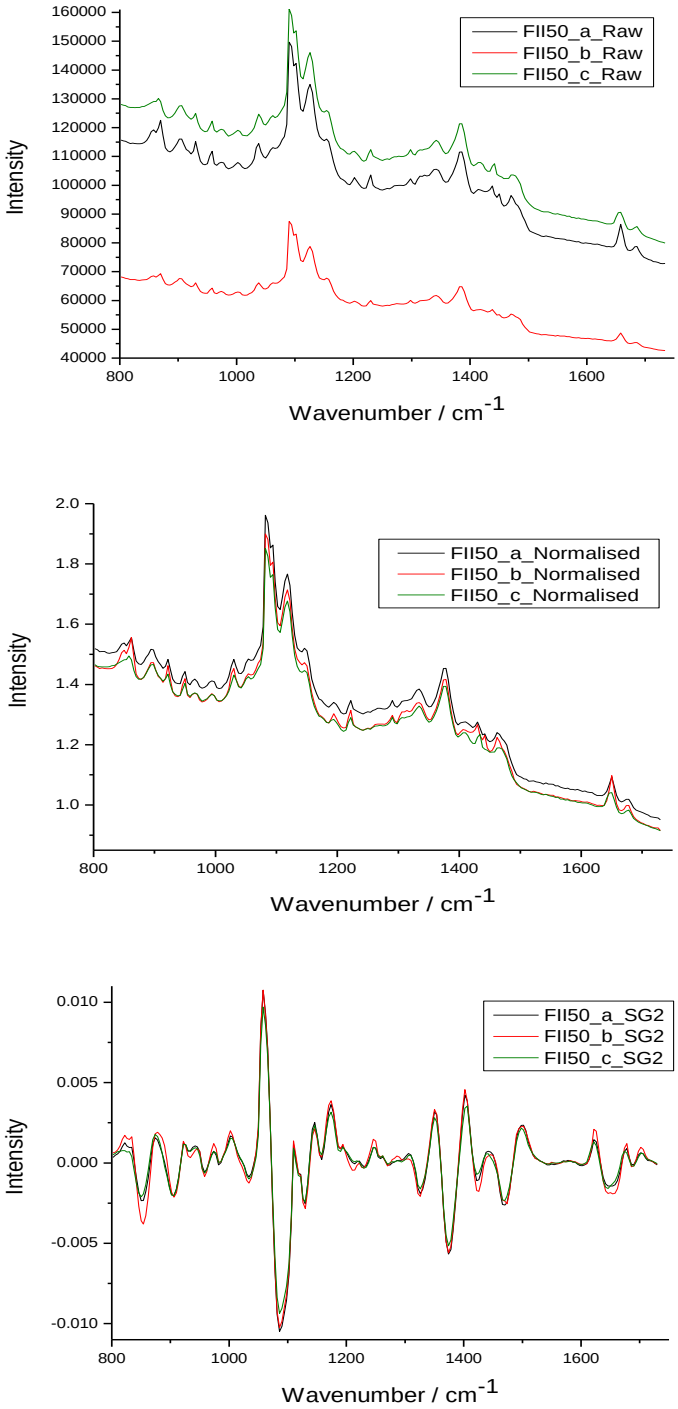

Figure 56 BRS spectra of FII 50 replicate samples. Top, raw spectra; middle, normalised spectra; and second derivative spectra on the bottom.

8.7.2 TRS PLS models of 1 mm Piratabs

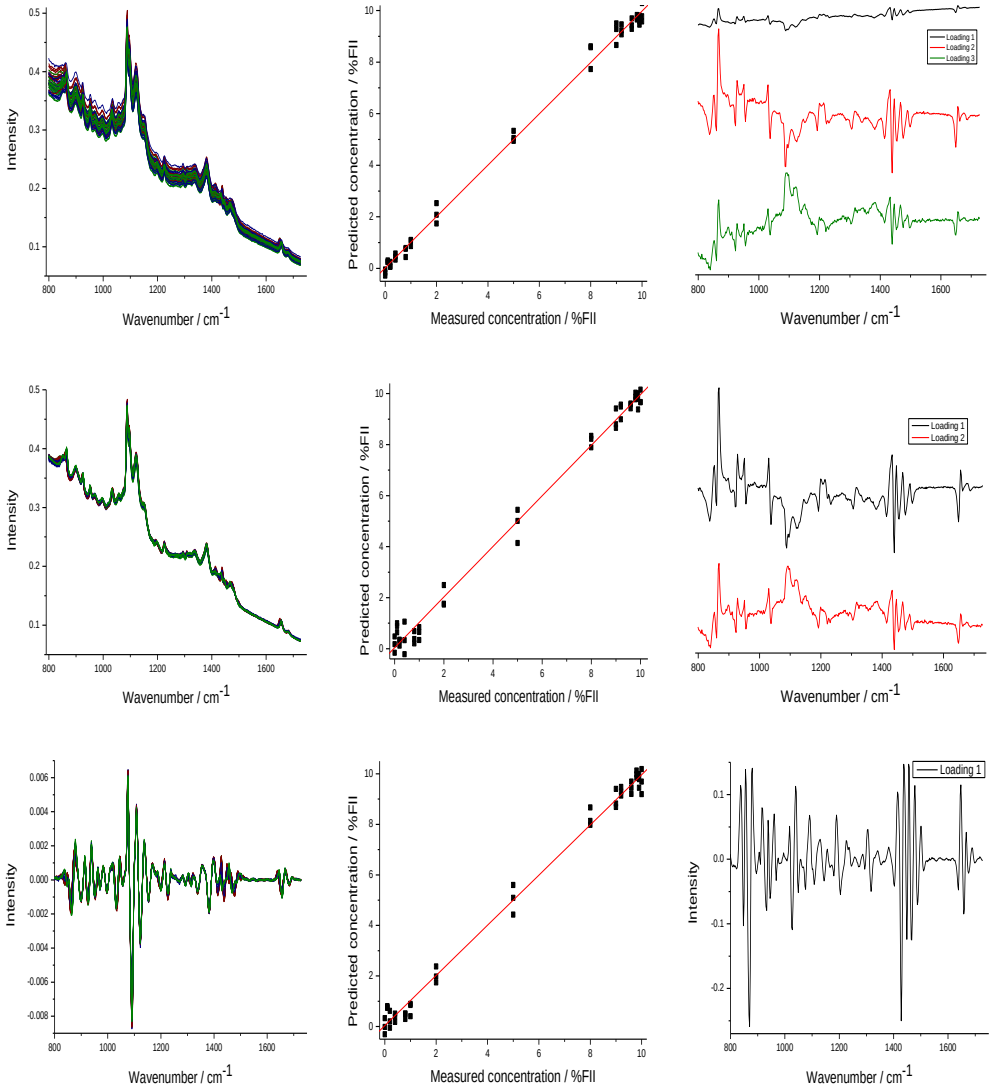

Figure 57 Top left, raw TRS spectra; top middle, measured vs. predicted FII piracetam concentration plot; top right, loadings of PLS model of raw spectra; center left, MSC pre-processed TRS spectra, center middle mea

In PLS models built using raw data there are three latent variables with loadings corresponding to the sloping MCC baseline which strongly features in all Raman spectra with the remaining loadings due to the polymorphic forms (Fig. 57). The high correlation coefficient of 0.998 with the raw models suggests that the data collected is intrinsically good (Table 30), particularly when compared directly to the raw BRS PLS models. Pre–processing the spectral data using MSC reduces baseline offsets due to the interaction of light with the tablets as shown above. Further pre-processing the TRS data with a second derivative highlights the polymorphic content differences

in the tablets. This is most noticeable in the 800–1750 cm^{-1} region presented above as this region contains the majority of obvious variances between the polymorphs as detailed in Section 6.2 Raman spectroscopy of piracetam.

Table 30 Performance of the regression models using different pre-processing methods. This data was the TRS spectra collected from the 1 mm thick tablets. RMSE values in % w/w.

Pre–processing	Region	LV	RMSEC	R^2	RMSECV	RMSEP
Norm data	Full	3	0.25	0.998	0.28	0.37
	Half	3	0.25	0.998	0.28	0.36
	A	2	0.42	0.952	0.46	0.25
	B	3	0.26	0.998	0.29	0.31
	C	2	0.36	0.997	0.40	0.39
MSC	Full	2	0.33	0.997	0.37	0.44
	Half	2	0.33	0.997	0.36	0.44
	A	2	0.30	0.998	0.35	0.39
	B	2	0.39	0.996	0.44	0.33
	C	2	0.44	0.995	0.51	0.37
MSC & 2^{nd} deriv.	Full	1	0.28	0.998	0.30	0.61
	Half	1	0.28	0.998	0.30	0.61
	A	1	0.38	0.996	0.41	0.30
	B	1	0.36	0.997	0.37	0.29
	C	1	0.29	0.998	0.30	0.64

All results of the quantitative models with varying pre-processing methods are presented in Table 30. All models share high correlation coefficients and low RMSE values. TRS models have lower errors of prediction RMSEP associated with them which is a vast improvement on the BRS PLS models. This can be attributed to the fact that TRS samples more of the tablet in comparison to BRS and the Raman signal generated is representative of the tablet bulk and relatively insensitive to surface inhomogeneities unlike BRS.

A model built using the low wavenumber spectral region (44–250 cm^{-1}) also generated similar results (referred to as data region C in Table 30 and depicted in Fig. 58). Access to the phonon mode region using TRS allowed for PLS models with practically equal performance to the best generated model from 801–1730 cm^{-1}. The model generated using normalised spectra was composed of two latent variables corresponding to either polymorph. Band intensity differences between the polymorphs are evident at 105 cm^{-1} and there is a splitting of the 91 cm^{-1} band in the FII polymorph where we see a reduction in the intensity at 91 cm^{-1} coupled with the appearance of a strong shoulder at 79 cm^{-1}. These spectral differences are amplified

by use of the MSC and second derivative pre-processing methods used as can be observed in the Fig. 58. The loadings plot of the MSC and second derivative pre-processed PLS model suggest that these regions have the largest influence on the model as there are a sharp changes at these positions in the loadings plot. The main difference in the region is due to the change in polymorph composition and the excipients exhibit very few bands which makes use of this phonon mode region straight–forward.

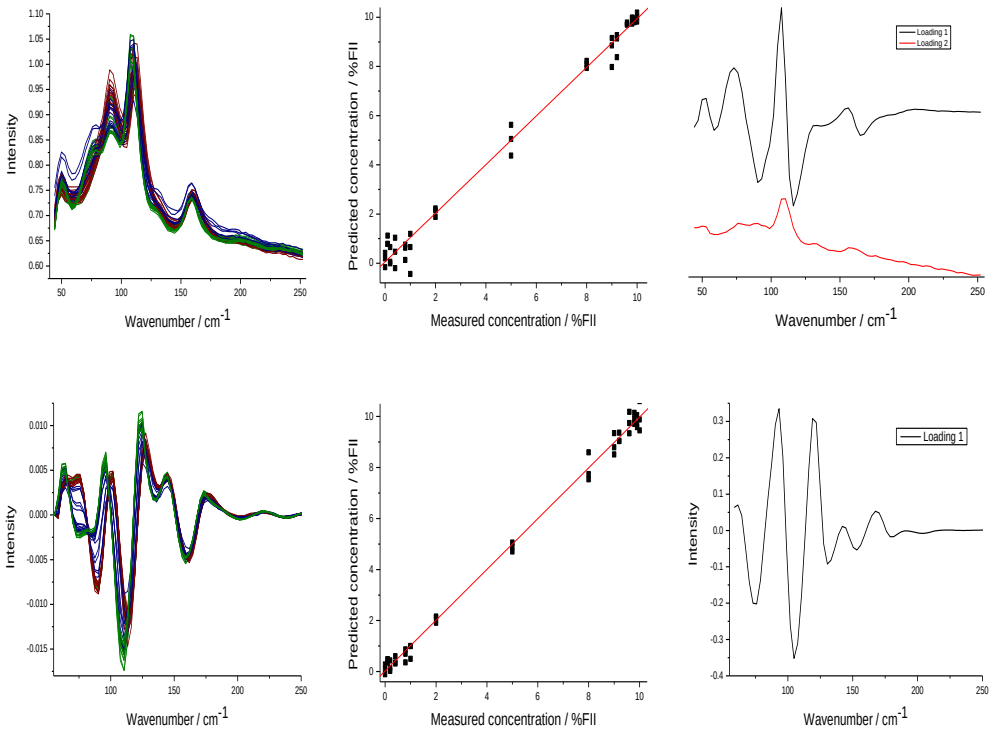

Figure 58 Top left, Normalised TRS spectra; middle, measured vs. predicted FII piracetam concentration plot; and right, loadings of PLS model. Bottom left, MSC and 2nd derivative pre-processed TRS spectra; middle, meas

8.7.3 NIR PLS models of 1 mm Piratabs

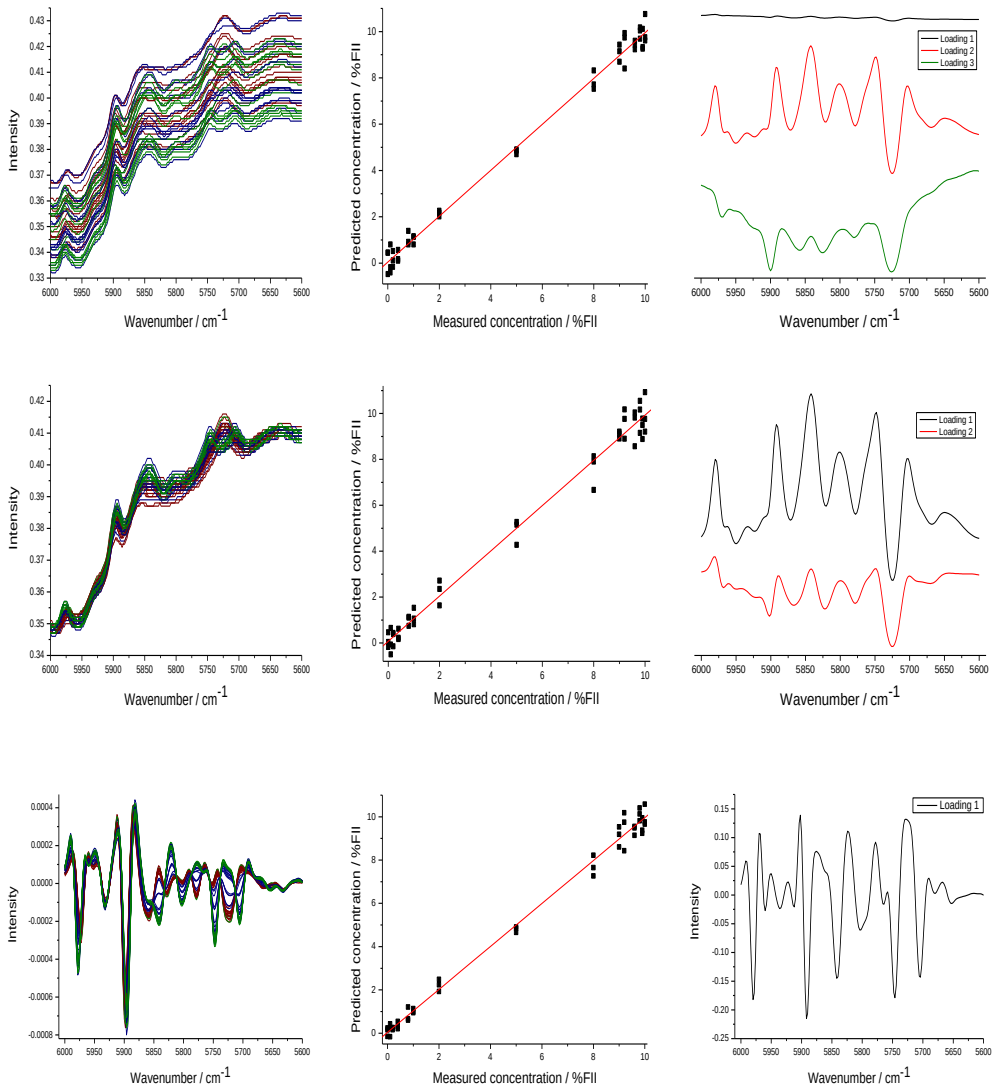

Figure 59 Top left, raw NIR spectra; top middle, measured vs. predicted FII piracetam concentration plot; top right, loadings of PLS model of raw spectra; center left, MSC pre-processed NIR spectra; center middle, measured vs. predicted FII piracetam concentration plot; and center right, loadings of this PLS model. bottom left, MSC and 2nd derivative pre-processed NIR spectra; bottom middle, measured vs. predicted FII piracetam concentration plot; and bottom right, loading 1 of best performing PLS model

A variety of discrete spectral regions of interest were selected to build PLS models and the models with the lowest error values typically involved selection of the spectral regions where the polymorph differences were most noticeable such as the 5870–5600 and 4314–4080 cm^{-1} spectral regions. Results of all PLS models built using NIR data is presented in Table 31. Raw spectral data of the same region show a high degree of scatter due to variations in the baseline signal which generates PLS

models with three latent variables. The loading 1 plot (Fig. 59) features what appears to be a baseline artefact and the remaining loadings consist of FII features which decrease in intensity with increasing loading number. Pre–processing the NIR spectra with MSC removes the baseline offsets and subtle differences between the spectra are more pronounced. Use of MSC pre-processed spectral data results in a reduction in the number of latent variables and associated RMSE errors of the PLS models generated. Combining the MSC pre-processed data with a second derivative results in a clear visual distinction between the tablets containing differing FII concentrations as shown in Fig. 59. PLS models built using this combination of pre-processing results in PLS models of one latent variable, which can be identified as the FII polymorph spectra once pre-processed in the same manner, with high correlation coefficients and low RMSE errors.

Table 31 Results of PLS models generated using 1 mm NIR pre-processed spectral data. RMSE in % w/w.

Pre–processing	Region	LV	RMSEC	R^2	RMSECV	RMSEP
Raw data	Full	5	0.42	0.995	0.52	0.96
	Half	5	0.37	0.996	0.44	1.19
	A and B	4	0.50	0.993	0.57	1.50
	A	3	0.38	0.996	0.43	0.87
	B	2	0.77	0.983	0.83	2.18
MSC	Full	4	0.44	0.995	0.51	0.94
	Half	3	0.39	0.996	0.52	1.01
	A and B	2	0.47	0.994	0.54	1.44
	A	2	0.51	0.993	0.56	0.72
	B	2	0.65	0.988	0.70	1.24
MSC & 2^{nd} deriv.	Full	1	0.34	0.997	0.36	0.55
	Half	1	0.34	0.997	0.36	0.56
	A and B	1	0.37	0.996	0.39	0.59
	A	1	0.37	0.996	0.38	0.54
	B	1	0.61	0.990	0.63	1.22

The best model, by definition of the model that produced the lowest error values based on the lowest number of latent variables, was the 6000–5600 cm^1 spectral region where values of 0.37 and 0.39% FII for RMSEC and RMSECV were obtained with a high linear relationship observed between the calculated and actual FII content with a R^2 value of 0.9963 for the 1 mm tablets. On testing this model using the external prediction set a RMSEP of 0.54% FII was produced representing a ~5.4% level of FII contamination in the FIII component. The model was composed of one

latent variable, which as shown by its loading in Fig. 59 is due to the change in FII content.

8.8 Discussion

8.8.1 Quantification of 1mm tablets

NIR and TRS gave comparable quantitative results with small differences in their error values. Limits of detection were calculated for both and TRS was marginally better than NIR with a LOD of 0.6% FII when compared to a LOD of 0.7% FII for NIR. This improvement may be due to the fact that the spectral differences between the polymorphs were more readily observable in the Raman data because Raman spectra by their nature consist of sharp, well defined bands and peaks. In contrast NIR spectra mostly comprise of broad, not readily assignable, bands and in the case of piracetam the NIR spectral differences were subtle in the tablets – please refer to Fig. 53.

The best models were selected on the basis of an appropriate combination of low error values and a low number of latent variables. For the NIR data, the best quantitative model used the 6000–5600 cm^{-1} and required only one latent variable (Table 32). On testing this model with the external prediction set a RMSEP of 0.54% FII was obtained which indicates that the FII contamination can be reasonably well quantified. This 0.54% RMSEP value represents a ~5.4% level of FII contamination in the FIII component. These results are comparable to that achieved when NIR was used previously for the determination of bromazepam and clonazepam concentrations in low dosage tablets. Standard errors of prediction (SEPs) of 0.59 and 0.57% w/w respectively were reported.(187)

TRS spectra were first normalised then a variety of pre-processing methods were applied including MSC and a 9 point second derivative Savitzky-Golay. These methods were used to try and maximise differences between the spectra as a result of changing FII polymorph concentration. The best quantitative models for the 1 mm

tablets (Table 32) used the 801–1730 cm^{-1} spectral region, and there is no real statistical difference between the use of the normalised raw data and the MSC/2nd derivative processed spectra, except that the normalised data required 3 LV's. This spectral region included the majority of the large spectral differences between the polymorphs such as the band shifts in the 1530–1370 cm^{-1} spectral region, the differences between the polymorphs in their respective carbonyl stretching vibrations around 1650 cm^{-1} and the peak specific to FIII at 1410 cm^{-1}. The relatively high degree of consistency in the PLS models built using the TRS data is testament to the intrinsically high quality of the data collected. A model built using the low wavenumber spectral region (44–250 cm^{-1}) also generated similar results. The data does not show too much scatter and the loadings plot indicates that the bands at 79 and 106 cm^{-1} have the largest influence. One significant advantage of using this spectral region is that there are very few interfering bands from the MCC and magnesium stearate excipients. So apart from the slightly increased noise/signal ratio due to the scattering background the bands changes due to each polymorphic form are very clear. It is also worth noting that there is very little difference in the quantitative modelling if one is looking for FII in FIII or visa–versa.

MSC and a Savitzky-Golay second derivative which maximised differences in the spectra between the differing ratios of polymorphs present particularly in the 1370–1730 cm^{-1} spectral region was employed for BRS spectra. The large degree of scatter and high RMS errors for the BR quantitative models is most likely due to the sampling factor. Overall, the results from our comparative TRS and BR study are similar to that reported by Johansson and co–workers for a simple binary tablet system.(75) They used a dedicated tablet press and mixtures of propranolol (16 to 24% w/w) and mannitol to produce ~3 mm thick tablets. They found that TRS outperformed the BR method by ~20% with RMSECV values of between 0.4 and 0.6% w/w being obtained. As in our case, the improved results from TRS are ascribed to better sampling statistics. It is also worth noting that the quantification accuracy was nearly as good here, despite the facts that our tablet system has a very significant baseline artefact induced by the MCC, that the BR spot size used here was 200 μm (compared to the 6 mm diameter in the Johansson study) and that we only used a small 4 × 4 mapping grid.

Table 32 Performance of the PLS models for quantification of piracetam FII in 1mm model tablet formulation using spectroscopic methods.

Methods	Pre–processing	R^2	Latent Variables	RMSEC (%)	RMSECV (%)	RMSEP (%)
NIR	Raw	0.996	3	0.38	0.43	0.87
	MSC and 2nd Derivative	0.996	1	0.37	0.38	0.54
BRS	Raw	0.969	3	1.04	1.21	2.37
	Normalised, MSC and 2nd Derivative	0.965	1	1.11	1.16	2.11
TRS	Raw	0.998	3	0.26	0.29	0.31
	Normalised, MSC and 2nd Derivative	0.997	1	0.36	0.37	0.29

In all cases MCC, the main excipient present had a large effect on the spectra. In the case of Raman it generated a baseline which may be related to diffuse or Mie scattering of the 20 μm MCC particles.(258) The NIR tablet spectra were fundamentally that of MCC as it is the main tablet constituent and although it does not swamp the signals due to the polymorphs, visually the polymorphic regions are more difficult to discern. However the combination of NIR with multivariate chemometric methods was able to use what little information pertaining to the two polymorphs was left in the NIR tablet spectra to build useful quantification models.

8.8.2 The effect of tablet thickness on quantification

The ability to analyse tablets of different thicknesses was also investigated. Overall TRS outperformed NIR and BRS in terms of model consistency for all thicknesses (1, 2 and 3 mm), Fig. 60 with legend detailed in Table 33 illustrates this trend. The TRS models are all very similar with only a small increase in RMSEC for the thicker tablets as might be expected due to the fact that the signal is collected from the majority of the sample in comparison to the other techniques.(250) Improving on these results might be achieved by a revised data collection method to reduce the intrinsic noise in the raw spectra (average ~128 or 256 acquisitions per sample). This could be achieved without an excessive time penalty and thus maintain the high throughput capability. The BRS RMSEC values are all much greater than those

presented for the NIR and TRS models. The RMSEC values do not vary much going from normalized to MSC and MSC and second derivative pre-processed models.

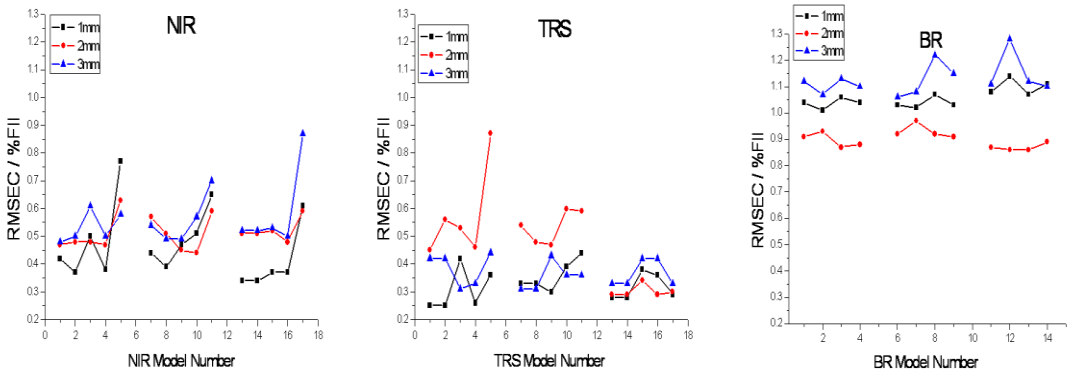

Figure 60 Plots of the effect of tablet thickness and pre-processing on PLS models. Left, NIR PLS models; middle, BRS PLS models; and right, TRS PLS models. Generated using RMSEC values from Tables 29, 30 and 31.

Table 33 Model numbers and corresponding spectral regions as legend for plots of the effect of tablet thickness and pre-processing on PLS models.

	NIR		TRS		BRS	
Model Number	Spectral Region	Pre–processing	Spectral Region	Pre–processing	Spectral Region	Pre–processing
1	Full		Full		Full	
2	Half		Half		Half	
3	A and B	Raw	A	Normalised	A	Normalised
4	A		B		B	
5	B		C			
6					Full	
7	Full		Full		Half	
8	Half	MSC	Half	MSC	A	MSC
9	A and B		A		B	
10	A		B			
11	B		C		Full	
12					Half	
13	Full		Full		A	
14	Half	MSC &	Half	MSC &	B	MSC &
15	A and B	2^{nd} Deriv.	A	2^{nd} Deriv.		2^{nd} Deriv.
16	A		B			
17	B		C			

#For the NIR based quantitative analysis, the thinner 1 mm tablets were found to provide the best quantitative models, as this is due to a more complete sampling of the whole tablet due to pathlength effects. To further investigate this PCA was performed on all NIR spectra collected from tablets of all thicknesses and using the

raw data we see a clear separation between the 1 mm samples and all other tablet sets (Fig. 61). This did not occur when PCA was performed on the Raman spectra. Combination of MSC with a second derivative shows no segregation of the 1 mm samples from the other samples and it can be seen that all the samples of different thicknesses separate into three distinct clusters representing those samples with a high concentration of FII, a low concentration of FII and then the 50:50 samples containing 50:50 FII:FIII in the centre of Fig. 61 right. This is the same for all techniques as pre-processing maximises chemical information which in this case is the concentration differences of the polymorph contaminant.

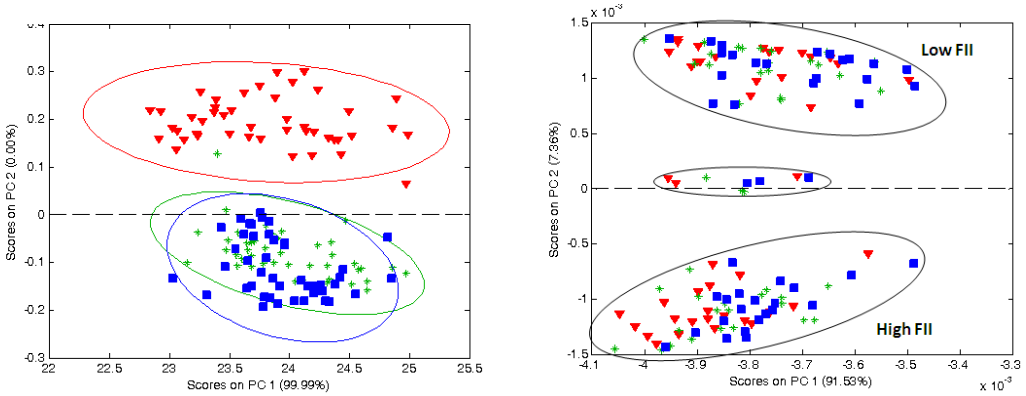

Figure 61 PCA analysis of tablets of all thicknesses analysed using NIR. Left, Raw NIR data; and right: MSC and second derivative treated NIR data. 1 (red triangles), 2 (blue blocks) and 3 mm (green asterisks) thick samples.

Transmission NIR, as shown in Fig. 62, of the different thickness samples show that a small fraction (0.1 to ~0.003%) of the NIR incident light passes through the 1 mm tablets but that the thicker tablets this is further reduced to 0.01 to 0.003%. This indicates that for the 2 and 3 mm tablets the effective sampled volume only comprises the top ~1 mm layer and that the rest of the sample is not analysed in the diffuse reflectance mode used. This lack of penetration of diffuse reflectance is noted in the literature (176-178) with Saeed *et al.* reporting a penetration depth of ~ 0.5 mm with diffuse reflectance NIR.(259) This confirms the PCA result obtained where there is a systematic variation according to tablet thickness with the 1 mm tablet data being very distinct from the 2 and 3 mm tablet data. For the BRS models, the sub–sampling issue tends to obscure any systematic variation and any thickness effect is less obvious.

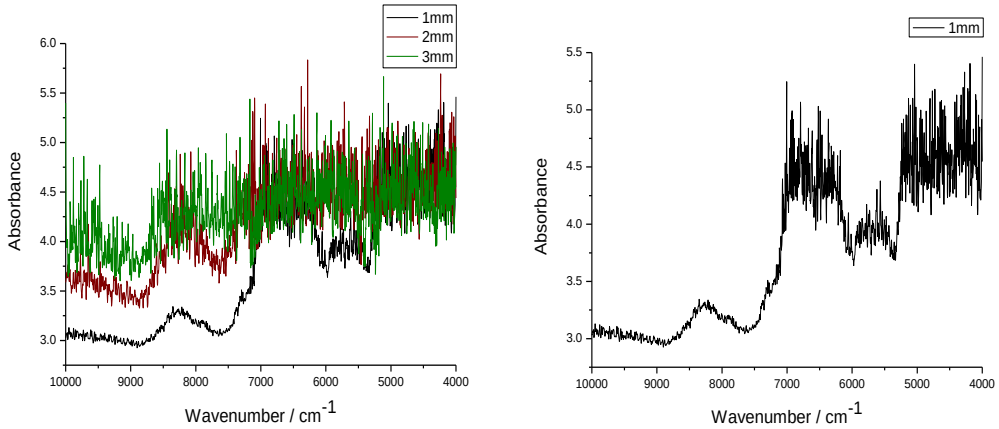

Figure 62 Left, Transmission NIR spectra of 1, 2 and 3 mm thick tablets; and right. Transmission NIR spectrum of 1 mm thick tablet.

8.8.3 Comparison of TRS and BRS

8.8.3.1 Tablet area sampled by Raman methods

TRS makes use of an 8 mm diameter spot size and when compared to the 200 μm of the BRS system, the surface area sampled by TRS is ~100 times greater. The effective sampled volume is even greater because BRS essentially samples the top surface (estimated depth of field for the BRS systems optics is ~400–600 μm) whereas in TRS an increased volume of the tablet is sampled.(260)

Table 34 Calculation of tablet surface area analysed using TRS and BRS.

Surface area of 13 mm tablet	1.33×10^{-4} m
Area of TRS 8 mm spot size	5.03×10^{-5} m
% of surface analysed using TRS	38%
Area of BRS 200μm spot size	3.14×10^{-8} m
Area of 16x16 200μm spot size	5.03×10^{-7} m
% of tablet analysed using BRS	0.4%

In comparing the two Raman methods the quantification accuracies are very different. This is due to the difference in sampling volumes associated with the two geometries. TRS is more representative of the bulk whereas BRS can be hindered by sub–sampling. Overall TRS samples ~38% of the tablet surface whereas BRS manages 0.38% (Table 34).

8.8.3.2 Assessment of Raman signal quality

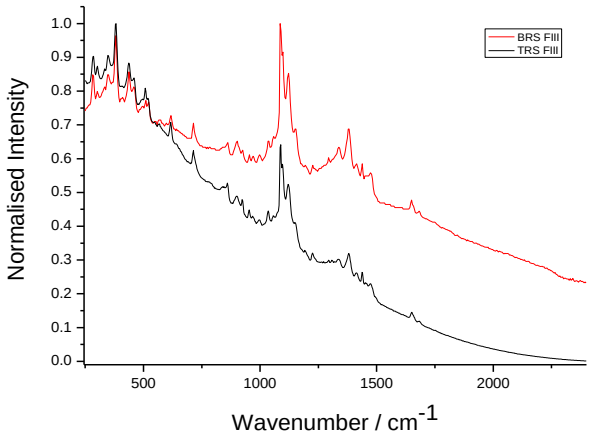

Figure 63 BRS and TRS spectra of 100:0 FII:FIII tablet.

In comparing the Raman signal quality from the two methods, it is clear that there is not a lot to choose between the two, particularly since we are dealing with non–fluorescent samples. Intrinsically on the excitation side, the 830 nm TRS will be ~80% as efficient (due to the 4^{th} power wavelength dependence) compared to 785 nm and thus requires a greater excitation power, likewise on the detection side the CCD detectors have lower quantum yields in the equivalent Raman spectral regions. It is evident from the above spectra that the same tablet analysed by the two different systems shows a difference in baseline slopes. This could potentially be attributed to the different scattering of the MCC particles by the two differing laser sources.

The signal to noise ratios of the averaged spectra used for chemometrics from BRS and TRS were found to be 0.93 and 7.63 respectively. The ratios were calculated by taking a spectral region free from any spectral features as a measurement of the level of noise and divided by the intensity of a peak characteristic of piracetam as a measurement of signal. As regards the number of acquisitions used for each method, the average TRS spectra were a result of using 32 acquisitions per sample while the BRS data was an average of 160 spectra (10 acquisitions per point using 4 × 4 mapping grid) led to the TRS data being ~8 times less noisy than the BRS data. Eliminating the noise issue for the BRS data can easily be achieved by the averaging of multiple spectra, although this would reduce the high throughput somewhat. Therefore the intrinsic advantage of a 785 nm excitation source was overcome by the better area sampling and much lower acquisition times in TRS mode.

8.8.3.3 Reproducibility of the Raman data

The variation in the raw TRS spectra compared to the BRS is much less when the replicate data was evaluated. PCA scores plots (Fig. 64) of raw Raman spectra (TRS and BRS) taken from the 3 mm samples of one concentration (seven replicate measurements) show that the BRS spectra exhibits much more variation than TRS spectra. The TRS spectra form a small cluster near the middle of the scores plot and when this area is zoomed in on it shows much less variation between samples analysed using TRS. This is due to the different volumes being sampled by the two techniques and the sensitivity of BRS to surface inhomogeneities.

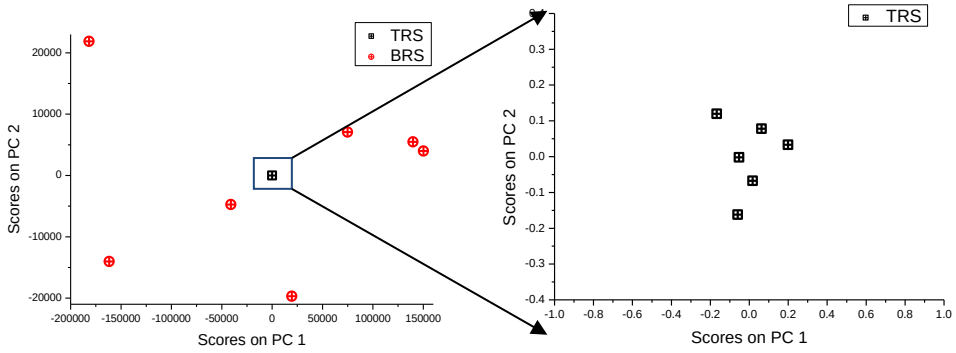

Figure 64 Left, PCA scores plot of raw spectra taken from six replicates of the 3 mm thick tablets at one concentration (10:90% FII:FIII) and analysed by TRS and BRS. Right: Zoomed in view of points corresponding to TRS spectra.

8.8.3.4 Analysis speed

Analysis times per tablet for BRS required a total analysis time of 3 minutes using a 4 × 4 grid of spectra, NIR required 2.5 minutes per tablet, while TRS just required 6.5 seconds per tablet. This dramatic reduction in acquisition time enables the high–throughput screening of large numbers of samples. A revised experimental design using a 12 × 12 grid with a single exposure of 2 seconds at each point would improve matters, and might generate a more accurate result. However, this increase in sampled area by a factor of 9 is still a long way from the 38% of the surface sampled by TRS. The simplest option for the BRS method would be to change the focusing optics to enable a large 1 or 2 mm diameter spot size to be used, or use a PhAT probe (Kaiser Optical Systems, Ann Arbor, Michigan, USA) with a much larger sample spot size.(233)

8.9 Chapter conclusions

Rapid spectroscopic methods were successfully employed for the analysis of a model pharmaceutical system containing low levels of polymorphic contaminant. These methods are non–destructive and are sensitive to the presence to low levels of polymorphic contaminant in a model tablet system, in this case low levels of FII piracetam in a 10% API loading of FIII piracetam. Quantitative PLS models generated were able to predict low content FII polymorph contaminant in tablets. In each case, spectral pre-processing was necessary for the development of robust quantitative models as it amplified the chemical information in the spectra. This was true for all techniques in particular NIR as the MCC signal masked information pertaining to the polymorphic composition of the tablets. Models built using Backscattering Raman were the poorest due to the inherent sub–sampling issue associated with this collection geometry despite use of a 4 × 4 mapping grid. Quantitative models built using TRS and NIR spectra were comparable in terms of limits of detection with TRS slightly better with a LOD of 0.6% FII with NIR having a LOD of 0.7% FII.

Two different Raman sampling geometries were employed through this study. TRS offered improved sampling of the tablets compared to BRS. TRS when compared to BRS sampled 100 times more of the tablet surface area, meaning that the effective sampling area would be much greater in the case of TRS as it samples through the tablet. Since the TRS Raman signal was more representative of the bulk tablet and insensitive to surface in–homogeneities as is an issue with BRS, spectral data was more reproducible showing much less variation than BRS spectral data.

TRS was by far the quickest means of analysis, taking approximately 5 seconds per tablet contrasting the 2.5 and 3 minutes per sample necessary for NIR and BRS respectively. TRS data was intrinsically good with very high correlation coefficients and of all the techniques did not suffer a decrease in RMSEs as a result of increasing tablet thickness. This study highlights the potential of TRS for the quantification of low levels of polymorphic contaminant in pharmaceutical formulations.

9 Thesis conclusions

We have demonstrated the utility of vibrational spectroscopic methods in particular Transmission Raman spectroscopy for the analysis of pharmaceutical systems. Transmission Raman though discovered in the 1960s is finding its place within pharmaceutical applications to which this work adds to the growing body of applications through quantification of active ingredients to that of polymorphic contaminants in tablet formulations.

Quantitative analysis of a model pharmaceutical tablet system consisting of an API–type molecule in a matrix of two excipients was feasible using NIR and Transmission Raman spectroscopies and PXRD. In each case, spectral pre-processing to remove instrumental and measurement artefacts were critical to the development of robust quantitative models.

PXRD based models could be generated with relatively high RMSEC and RMSEP accuracies, however, the method was more time consuming than vibrational spectroscopy based methods. NIR spectroscopy gave the best accuracy in terms of RMSEC and RMSEP and the method is rapid although spectral interpretation can be challenging due to the nature of the bands. Transmission Raman Spectroscopy for this compound was intermediate in performance. The main factor which degraded the TRS performance was the substantial fluorescence in the model system arising from the MCC and the ROY itself, this reduced the S/N and made the generation of more accurate models unfeasible. In terms of time, TRS was by far the quickest means of analysis, taking approximately 5 seconds per tablet which contrasts to the 2.5 and 16 minutes per sample necessary for NIR and PXRD respectively.

Rapid spectroscopic methods were successfully employed for the analysis of a model pharmaceutical system containing low levels of polymorphic contaminant. These methods are non–destructive and are sensitive to the presence to low levels of polymorphic contaminant in a model tablet system, in this case low levels of FII piracetam in a 10% API loading of FIII piracetam. Quantitative PLS models generated were able to predict low content FII polymorph contaminant in tablets. In each case, spectral pre-processing was necessary for the development of robust

quantitative models as it amplified the chemical information in the spectra. This was true for all techniques in particular NIR as the excipient signals masked information pertaining to the polymorphic composition of the tablets. Models built using Backscattering Raman were the poorest due to the inherent sub–sampling issue associated with this collection geometry despite use of a 4 × 4 mapping grid. Quantitative models built using TRS and NIR spectra were comparable in terms of limits of detection with TRS slightly better with a LOD of 0.6% FII with NIR having a LOD of 0.7% FII.

Two different Raman sampling geometries were employed through this study. TRS offered improved sampling of the tablets compared to BRS. TRS when compared to BRS sampled 100 times more of the tablet surface area, meaning that the effective sampling area would be much greater in the case of TRS as it samples through the tablet. Since the TRS Raman signal was more representative of the bulk tablet and insensitive to surface in–homogeneities as is an issue with BRS, spectral data was more reproducible showing much less variation than BRS spectral data.

TRS was by far the quickest means of analysis, taking approximately 5 seconds per tablet contrasting the 2.5 and 3 minutes per sample necessary for NIR and BRS respectively. TRS data was intrinsically good with very high correlation coefficients and of all the techniques did not suffer a decrease in RMSEs as a result of increasing tablet thickness. This study highlights the potential of TRS for the quantification of low levels of polymorphic contaminant in pharmaceutical formulations.

Binary polymorphic mixtures of piracetam were analysed quantitatively using Raman and NIR spectroscopy, coupled with multivariate analysis of the spectroscopic data and PXRD patterns. Multivariate analysis of PXRD diffraction patterns in this case proved more accurate and reliable than use of a simple univariate method based on peak height intensity or area ratios of unique peaks characteristic from either polymorph. Use of a wider range of data points by including more of the diffraction pattern pertaining to the chemical information in this system is useful however, despite the effects of preferred orientation attributed to the FIII polymorph being greatly reduced by pre-processing the diffraction patterns by mean

normalization, the multivariate PXRD models did not have comparable accuracy or limits of detection or quantification that the multivariate spectroscopic models do.

Multivariate analysis of the Raman and NIR spectroscopic data in combination with pre-processing yielded models of higher linearity and accuracy of prediction of validation samples when compared to the PXRD models. In all cases the use of pre-processing greatly enhanced the spectral chemical information of the binary polymorph mixtures.

10 References

(1) Byrn S, Pfeiffer R, Ganey M, Hoiberg C, Poochikian G. Pharmaceutical Solids: A Strategic Approach to Regulatory Considerations. *Pharmaceutical Research* 1995; **12**.

(2) Rodríguez-Spong B, Price CP, Jayasankar A, Matzger AJ, Rodríguez-Hornedo N. General principles of pharmaceutical solid polymorphism: A supramolecular perspective. *Advanced drug delivery reviews* 2004; **56**: 241-274.

(3) Vippagunta SR, Brittain HG, Grant DJW. Crystalline solids. *Advanced Drug Delivery Reviews* 2001; **48**: 3-26.

(4) Bermajo M, Gonzalez-Alvarez I. How and where are drugs absorbed?, *Preclinical Development Handbook*. Hoboken: John Wiley and Sons: Hoboken, 2008: 249-280.

(5) Blagden N, Davey RJ. Polymorph Selection: Challenges for the Future? *Crystal Growth & Design* 2003; **3**: 873.

(6) Bond AD. Polymorphism in molecular crystals. *Current Opinion in Solid State and Materials Science* 2009; **13**: 91-97.

(7) Braga D, Grepioni F, Maini L. The growing world of crystal forms. *Chemical Communications* 2010; **46**: 6232-6242.

(8) Brittain HG. Polymorphism and solvatomorphism 2009. *Journal of pharmaceutical sciences* 2010; **101**: 464-484.

(9) Desiraju GR. Crystal and co-crystal. *CrystEngComm* 2003; **5**: 466-467.

(10) Desiraju GR. Polymorphism: The Same and Not Quite the Same. *Crystal Growth & Design* 2008; **8**: 3-5.

(11) Giron D, Goldbronn C, Mutz M, Pfeffer S, Piechon P, Schwab P. Solid state characterizations of pharmaceutical hydrates. *Journal of Thermal Analysis and Calorimetry* 2002; **68**: 453-465.

(12) Good DJ, Rodríguez-Hornedo N. Solubility Advantage of Pharmaceutical Cocrystals. *Crystal Growth & Design* 2009; **9**: 2252-2264.

(13) Herbstein FH. Diversity Amidst Similarity: A Multidisciplinary Approach to Phase Relationships, Solvates, and Polymorphs. *Crystal Growth & Design* 2004; **4**: 1419-1429.

(14) Karpinski P. Polymorphism of active pharmaceutical ingredients. *Chemical Engineering Technology* 2006; **29**: 233-237.

(15) Llinas A, Goodman JM. Polymorph control: past, present and future. *Drug Discovery Today* 2008; **13**: 198-210.

(16) Lu J, Rohani S. Polymorphism and Crystallisation of Active Pharmaceutical Ingredients (APIs). *Current Medicinal Chemistry* 2009; **16**: 884-905.

(17) Mangin D, Puel F, Veesler S. Polymorphism in Processes of Crystallization in Solution: A Practical Review. *Organic Process Research & Development* 2009; **13**: 1241-1253.

(18) Morissette SL, Almarsson O, Peterson ML, et al. High-throughput crystallization: polymorphs, salts, co-crystals and solvates of pharmaceutical solids. *Advanced drug delivery reviews* 2004; **56**: 275-300.

(19) Rodriguez-Spong B, Price CP, Jayasankar A, Matzger AJ, Rodriguez-Hornedo N. General principles of pharmaceutical solid polymorphism: a supramolecular perspective. *Advanced drug delivery reviews* 2004; **56**: 241-274.

(20) Vishweshwar P, McMahon JA, Bis JA, Zaworotko MJ. Pharmaceutical co-crystals. *Journal of pharmaceutical sciences* 2006; **95**: 499-516.
(21) Shan N, Zaworotko MJ. The role of cocrystals in pharmaceutical science. *Drug Discovery Today* 2008; **13**: 440-446.
(22) Aaltonen J, Alleso M, Mirza S, Koradia V, Gordon KC, Rantanen J. Solid form screening--a review. *European Journal of Pharmaceutics and Biopharmaceutics* 2009; **71**: 23-37.
(23) Schultheiss N, Newman A. Pharmaceutical Cocrystals and Their Physicochemical Properties. *Crystal Growth & Design* 2009; **9**: 2950-2967.
(24) McCrone W, Haleblian J. Pharmaceutical Applications of Polymorphism. *Journal of Pharmaceutical Sciences* 1969; **58**: 911-929.
(25) Nangia A. Conformational polymorphism in organic crystals. *Accounts of Chemical Research* 2008; **41**: 595-604.
(26) Bauer J, Spanton S, Henry R, et al. Ritonavir: An Extraordinary Example of Conformational Polymorphism. *Pharmaceutical research* 2001; **18**: 859-866.
(27) Chemburkar SR, Bauer J, Deming K, et al. Dealing with the Impact of Ritonavir Polymorphs on the Late Stages of Bulk Drug Process Development. *Organic Process Research & Development* 2000; **4**: 413-417.
(28) Pudipeddi M, Serajuddin ATM. Trends in solubility of polymorphs. *Journal of pharmaceutical sciences* 2005; **94**: 929 - 939.
(29) Singhal D, Curatolo W. Drug polymorphism and dosage form design: a practical perspective. *Advanced drug delivery reviews* 2004; **56**: 335-347.
(30) Ostwald WF. Translation: Studies on Formation and transformation of solid materials. *Z Phys Chem* 1897; **22**: 289-330.
(31) Threlfall T. Structural and Thermodynamic explanations of ostwald's rule. *Organic Process Research & Development* 2003; **7**: 1017-1027.
(32) Parmar MM, Khan O, Seton L, Ford J. Polymorph Selection with morphology control using solvents. *Crystal Growth & Design* 2007; **7**: 1635.
(33) USP-36-NF-31. <776> Optical Microscopy, 2013.
(34) Kato F, Otsuka M, Matsuda Y. Kinetic study of the transformation of mefenamic acid polymorphs in various solvents and under high humidity conditions. *International journal of pharmaceutics* 2006; **321**: 18-26.
(35) Fabbiani FPA, Allan DR, David WIF, et al. High-Pressure Studies of Pharmaceuticals: An Exploration of the Behavior of Piracetam. *Crystal Growth and Design* 2007; **7**: 1115-1124.
(36) Fabbiani FPA, Allan DR, Parsons S, Pulham CR. An exploration of the polymorphism of piracetam using high pressure. *CrystEngComm* 2005; **7**: 179-186.
(37) Oswald IDH, Chataigner I, Elphick S, et al. Putting pressure on elusive polymorphs and solvates. *CrystEngComm* 2009; **11**: 359-366.
(38) Cashell C, Corcoran D, Hodnett BK. Effect of amino acid additives on the crystallisation of L-Glutamic Acid. *Crystal Growth & Design* 2004; **5**: 593.
(39) Singh A, Lee IS, Myerson AS. Concomitant Crystallization of ROY on Patterned Substrates: Using a High Throughput Method to Improve the Chances of Crystallization of Different Polymorphs. *Crystal Growth and Design* 2009; **9**: 1182-1185.
(40) Zhang GG, Law D, Schmitt EA, Qiu Y. Phase transformation considerations during process development and manufacture of solid oral dosage forms. *Advanced drug delivery reviews* 2004; **56**: 371-390.

(41) Sharma P, Zujovic ZD, Bowmaker GA, Denny WA, Garg S. Evaluation of a crystalline nanosuspension: Polymorphism, process induced transformation and in vivo studies. *International journal of pharmaceutics* 2011; **408**: 138-151.
(42) Hubert S, Briancon S, Hedoux A, et al. Process induced transformations during tablet manufacturing: Phase transition analysis of caffeine using DSC and low frequency micro-Raman spectroscopy. *International journal of pharmaceutics* 2011; **420**: 76-83.
(43) Yu L, Stephenson GA, Mitchell CA, et al. Thermochemistry and Conformational Polymorphism of a Hexamorphic Crystal System. *Journal of the American Chemical Society* 2000; **122**: 585-591.
(44) Yu L. Polymorphism in Molecular Solids: An Extraordinary System of Red, Orange, and Yellow Crystals. *Accounts of Chemical Research* 2010; **43**: 1257-1266.
(45) Lilly Industries Limited. Kingsclare Road BHRXG. In: Patent E, ed., 1991.
(46) Bernstein J, Davey RJ, Henck J-O. Concomitant polymorphs. *Angewandte Chemie, Int Ed* 1999; **38**: 3441-3461.
(47) Yu L. Color Changes Caused by Conformational Polymorphism ROY: Optical-Crystallography, Single-Crystal Spectroscopy, and Computational Chemistry. *Journal of Physical Chemistry A* 2002; **106**: 544-550.
(48) Mitchell CA, Yu L, Ward MD. Selective Nucleation and Discovery of Organic Polymorphs through Epitaxy with Single Crystal Substrates. *Journal of the American Chemical Society* 2001; **123**: 10830-10839.
(49) Chen S, Guzei IA, Yu L. New Polymorphs of ROY and New Record for Coexisting Polymorphs of Solved Structures. *Journal of the American Chemical Society* 2005; **127**: 9881-9885.
(50) Chen S, Xi H, Yu L. Cross-nucleation between ROY polymorphs. *Journal of the American Chemical Society* 2005; **127**: 17439-17444.
(51) Price CP, Grzesiak AL, Matzger AJ. Crystalline polymorph selection and discovery with polymer heteronuclei. *Journal of the American Chemical Society* 2005; **127**: 5512-5517.
(52) Hilden JL, Reyes CE, Kelm MJ, Tan JS, Stowell JG, Morris KR. Capillary Precipitation of a Highly Polymorphic Organic Compound. *Crystal Growth & Design* 2003; **3**: 921-926.
(53) Ha J-M, Wolf JH, Hillmyer MA, Ward MD. Polymorph Selectivity under Nanoscopic Confinement. *Journal of the American Chemical Society* 2004; **126**: 3382-3383.
(54) Yu L. Amorphous pharmaceutical solids: preparation, characterization and stabilization. *Advanced drug delivery reviews* 2001; **48**: 27-42.
(55) Bhugra C, Pikal MJ. Role of thermodynamic, molecular, and kinetic factors in crystallization from the amorphous state. *Journal of pharmaceutical sciences* 2008; **97**: 1329-1349.
(56) Leuner C, Dressman J. Improving drug solubility for oral delivery using solid dispersions. *European Journal of Pharmaceutics and Biopharmaceutics* 2000; **50**: 47-60.
(57) Sotthivirat S, McKelvey C, Moser J, Rege B, Xu W, Zhang D. Development of Amorphous Solid Dispersion Formulations of a Poorly Water-Soluble Drug, MK-0364. *International journal of pharmaceutics* 2013; **452**: 73-81.
(58) Aakeroy CB, Salmon DJ. Building co-crystals with molecular sense and supramolecular sensibility. *CrystEngComm* 2005; **7**: 439-448.

(59) Blagden N, de Matas M, Gavan PT, York P. Crystal engineering of active pharmaceutical ingredients to improve solubility and dissolution rates. *Advanced drug delivery reviews* 2007; **59**: 617-630.
(60) Shan N, Zaworotko MJ. The role of cocrystals in pharmaceutical science. *Drug Discovery Today* 2008; **13**: 440-446.
(61) Byrn SR, Pfeffer S, Ganey M, Hoiberg C, Poochikian G. Pharma Solids: a strategic approach to regulatory considerations.pdf>. *Pharmaceutical research* 1995; **12**: 945-954.
(62) Raw AS, Furness MS, Gill DS, Adams RC, Holcombe FOJ, Yu LX. Regulatory considerations of pharmaceutical solid polymorphism in Abbreviated New Drug Applications (ANDAs). *Advanced drug delivery reviews* 2004; **56**: 397-414.
(63) CDER. ANDAs Pharmaceutical Solid Polymorphism: Chemistry, Manufacturing and Controls Information In: FDA, ed. http://www.fda.gov/cder/guidance/index.htm, 2007.
(64) FDA. International Conference on Harmonization Q6A Guideline; Specifications for New Drug Substances and Products: Chemical Substances: International Conference on Harmonization Q6A Guideline; Specifications for New Drug Substances and Products: Chemical Substances, 2000.
(65) Auer ME, Griesser UJ, Sawatzki J. Qualitative and quantitative study of polymorphic forms in drug formulations by near infrared FT-Raman spectroscopy. *Journal of Molecular Structure* 2003; **661-662**: 307-317.
(66) Pasquini C. Near Infrared Spectroscopy: Fundamentals, Practical Aspects and Analytical Applications. *Journal of the Brazilian Chemical Society* 2003; **14**: 198-219.
(67) Hendra PJ, Tudor AM, Melia CD, Binns JS, Church S, Davies MC. The application of Fourier-transform Raman spectroscopy to the analysis of pharmaceuticals and biomaterials. *Journal of pharmaceutical and biomedical analysis* 1990; **8**: 717-720.
(68) Raman CV, Krishnan KS. A New Type of Secondary Radiation. *Nature* 1928: 501-502.
(69) McCreery RL. *Raman Spectroscopy for Chemical Analysis* New York: Wiley Interscience, 2000.
(70) Strachan CJ, Rades T, Gordon KC, Rantanen J. Raman Spectroscopy for Quantitative Analysis of Pharmaceutical Solids. *Journal of Pharmacy and Pharmacology* 2007; **59**: 179-192.
(71) Lakowicz JR. *Principles of Fluoresence Spectroscopy*, Third edn.: Springer, 2009.
(72) Bocklitz T, Walter A, Hartmann K, Roesch P, Popp J. How to pre-process Raman spectra for reliable and stable models? *Analytical Chimica Acta* 2011; **704**: 47-56.
(73) Matousek P, Parker AW. Bulk Raman Analysis of Pharmaceutical Tablets. *Applied spectroscopy* 2006; **60**: 1353-1357.
(74) Matousek P. Raman Signal Enhancement in Deep Spectroscopy of Turbid Media. *Applied Spectrosopy* 2007; **61**: 845-854.
(75) Johansson J, Pettersson S, Folestad S. Characterization of different laser irradiation methods for quantitative Raman tablet assessment. *Journal of pharmaceutical and biomedical analysis* 2005; **39**: 510-516.

(76) Wikstrom H, Lewis IR, Taylor LS. Comparison of Sampling Techniques for In-Line Monitoring Using Raman Spectroscopy. *Applied spectroscopy* 2005; **59**: 934-941.
(77) Shin K, Chung H. Wide area coverage Raman spectroscopy for reliable quantitative analysis and its applications. *Analyst* 2013; **138**: 3335-3346.
(78) Allan P, Bellamy LJ, Nordon A, Littlejohn D, Andrews J, Dallin P. In situ monitoring of powder blending by non-invasive Raman spectrometry with wide area illumination. *Journal of pharmaceutical and biomedical analysis* 2013; **76**: 28-35.
(79) Schrader B, Bergmann G. Die Intensität des Ramanspektrums polykristalliner Substanzen. *Z Anal Chem* 1967; **225**: 230-247.
(80) Macleod NA, Matousek P. Deep Noninvasive Raman Spectroscopy of Turbid Media. *Applied Spectrosopy* 2008; **62**: 291A-304A.
(81) Eliasson C, Claybourn M, Matousek P. Deep Subsurface Raman Spectroscopy of Turbid Media by a Defocused Collection System. *Applied spectroscopy* 2007; **61**: 1123-1127.
(82) Macleod NA, Matousek P. Emerging non-invasive Raman methods in process control and forensic applications. *Pharmaceutical research* 2008; **25**: 2205-2215.
(83) Bloomfield M, Andrews D, Loeffen P, Tombling C, York T, Matousek P. Non-invasive identification of incoming raw pharmaceutical materials using Spatially Offset Raman Spectroscopy. *Journal of pharmaceutical and biomedical analysis* 2013; **76**: 65-69.
(84) Johansson J, Sparén A, Svensson O, Folestad S, Claybourn M. Quantitative Transmission Raman Spectroscopy of Pharmaceutical Tablets and Capsules. *Applied spectroscopy* 2007; **61**: 1211-1218.
(85) Hargreaves MD, Macleod NA, Smith MR, Andrews D, Hammond SV, Matousek P. Characterisation of transmission Raman spectroscopy for rapid quantitative analysis of intact multi-component pharmaceutical capsules. *Journal of pharmaceutical and biomedical analysis* 2011; **54**: 463-468.
(86) Eliasson C, Macleod NA, Jayes LC, et al. Non-invasive quantitative assessment of the content of pharmaceutical capsules using transmission Raman spectroscopy. *Journal of pharmaceutical and biomedical analysis* 2008; **47**: 221-229.
(87) Aina A, Hargreaves MD, Matousek P, Burley JC. Transmission Raman spectroscopy as a tool for quantifying polymorphic content of pharmaceutical formulations. *Analyst* 2010; **135**: 2328-2333.
(88) Elbagerma MA, Edwards HGM, Munshi T, Hargreaves MD, Matousek P, Scowen IJ. Characterization of New Cocrystals by Raman Spectroscopy, Powder X-ray Diffraction, Differential Scanning Calorimetry, and Transmission Raman Spectroscopy. *Crystal Growth & Design* 2010; **10**: 2360-2371.
(89) Fransson M, Johansson J, Sparén A, Svensson O. Comparison of multivariate methods for quantitative determination with transmission Raman spectroscopy in pharmaceutical formulations. *Journal of Chemometrics* 2010; **24**: 674-680.
(90) McGoverin CM, Hargreaves MD, Matousek P, Gordon KC. Pharmaceutical polymorphs quantified with transmission Raman spectroscopy. *Journal of Raman Spectroscopy* 2012; **43**: 280-285.

(91) Burley JC, Alkhalil A, Bloomfield M, Matousek P. Transmission Raman spectrscopy for quality control in model cocrystal tablets. *Analyst* 2012; **137**: 3052-3057.
(92) Townshend N, Nordon A, Littlejohn D, Andrews J, Dallin P. Effect of particle properties of powders on the generation and transmission of Raman scattering. *Analytical chemistry* 2012; **84**: 4665-4670.
(93) Townshend N, Nordon A, Littlejohn D, Myrick M, Andrews J, Dallin P. Comparison of the determination of a low-concentration active ingredient in pharmaceutical tablets by backscatter and transmission Raman spectrometry. *Analytical chemistry* 2012; **84**: 4671-4676.
(94) Lee Y, Kim J, Lee S, Woo YA, Chung H. Simple transmission Raman measurements using a single multivariate model for analysis of pharmaceutical samples contained in capsules of different colors. *Talanta* 2012; **89**: 109-116.
(95) J.M Chalmers, Griffiths PR. *Handbook of Vibrational Spectroscopy*: John Wiley and Sons Ltd., 2002.
(96) Roggo Y, Chalus P, Maurer L, Lema-Martinez C, Edmond A, Jent N. A review of near infrared spectroscopy and chemometrics in pharmaceutical technologies. *Journal of Pharmaceutical and Biomedical Analysis* 2007; **44**: 683-700.
(97) Kubelka P, Munk F. Ein Beitrag zur Optik der Farbanstriche. *Zeit Tech Physik* 1931; **12**: 593-601.
(98) Bakeev KA. *Process Analytical Technology*: Blackwell Publishing Ltd., 2005.
(99) Blanco M, Alcala M. Content uniformity and tablet hardness testing of intact pharmaceutical tablets by near infrared spectroscopyA contribution to process analytical technologies. *Analytica Chimica Acta* 2006; **557**: 353-359.
(100) J. O'Neil A, D. Jee R, C. Moffat A. Measurement of the cumulative particle size distribution of microcrystalline cellulose using near infrared reflectance spectroscopy. *Analyst* 1999; **124**: 33-36.
(101) Blanco M, Romero MA, Alcalà M. Strategies for constructing the calibration set for a near infrared spectroscopic quantitation method. *Talanta* 2004; **64**: 597-602.
(102) Cullity BD, Stock SR. *Elements of X-ray Diffraction*, 3rd edn.: Prentice-Hall, 2001.
(103) Campbell Roberts SN, Williams AC, Grimsey IM, Booth SW. Quantitative analysis of mannitol polymorphs. X-ray powder diffractometry--exploring preferred orientation effects. *Journal of pharmaceutical and biomedical analysis* 2002; **28**: 1149-1159.
(104) Chieng N, Rades T, Saville D. Formation and physical stability of the amorphous phase of ranitidine hydrochloride polymorphs prepared by cryo-milling. *European Journal of Pharmaceutics and Biopharmaceutics* 2008; **68**: 771-780.
(105) McArdle P, Gilligan K, Cunningham D, Ryder A. Determination of the polymorphic forms of bicifadine hydrochloride by differential scanning calorimetry-thermogravimetric analysis, X-ray powder diffraction, attenuated total reflectance-infrared spectroscopy, and attenuated total reflectance-near-infrared spectroscopy. *Applied spectroscopy* 2005; **59**: 1365-1371.

(106) Tiwari M, Chawla G, Bansal AK. Quantification of olanzapine polymorphs using powder X-ray diffraction technique. *Journal of pharmaceutical and biomedical analysis* 2007; **43**: 865-872.
(107) Hu Y, Erxleben A, Ryder AG, McArdle P. Quantitative analysis of sulfathiazole polymorphs in ternary mixtures by attenuated total reflectance infrared, near-infrared and Raman spectroscopy. *Journal of pharmaceutical and biomedical analysis*; **53**: 412-420.
(108) Agatonovic-Kustrin S, Rades T, Wu V, Saville D, Tucker IG. Determination of polymorphic forms of ranitidine-HCl by DRIFTS and XRPD. *Journal of pharmaceutical and biomedical analysis* 2001; **25**: 741-750.
(109) Uvarov V, Popov I. Development and metrological characterization of quantitative X-ray diffraction phase analysis for the mixtures of clopidogrel bisulphate polymorphs. *Journal of pharmaceutical and biomedical analysis* 2008; **46**: 676-682.
(110) Gamberini MC, Baraldi C, Tinti A, Rustichelli C, Ferioli V, Gamberini G. Solid state characterization of chloramphenicol palmitate. Raman spectroscopy applied to pharmaceutical polymorphs. *Journal of Molecular Structure* 2006; **785**: 216-224.
(111) Kachrimanis K, Braun DE, Griesser UJ. Quantitative analysis of paracetamol polymorphs in powder mixtures by FT-Raman spectroscopy and PLS regression. *Journal of pharmaceutical and biomedical analysis* 2007; **43**: 407-412.
(112) Mazurek S, Szostak R. Quantification of atorvastatin calcium in tablets by FT-Raman spectroscopy. *Journal of Pharmaceutical and Biomedical Analysis* 2009; **49**: 168-172.
(113) Fevotte G. In Situ Raman Spectroscopy for In-Line Control of Pharmaceutical Crystallization and Solids Elaboration Processes: A Review. *Chemical Engineering Research and Design* 2007; **85**: 906-920.
(114) Wartewig S, Neubert RH. Pharmaceutical applications of Mid-IR and Raman spectroscopy. *Advanced drug delivery reviews* 2005; **57**: 1144-1170.
(115) McGoverin CM, Rades T, Gordon KC. Recent Pharmaceutical Applications of Raman and Terahertz Spectroscopies. *Journal of pharmaceutical sciences* 2008; **97**: 4598-4621.
(116) Sasic S. *Pharmaceutical Applications of Raman Spectroscopy*: Wiley Interscience, 2008.
(117) Buckley K, Matousek P. Recent advances in the application of transmission Raman spectroscopy to pharmaceutical analysis. *Journal of pharmaceutical and biomedical analysis* 2011; **55**: 645-652.
(118) Gordon KC, McGoverin CM. Raman mapping of pharmaceuticals. *International journal of pharmaceutics* 2011; **417**: 151-162.
(119) Moros J, Garrigues S, Guardia Mdl. Vibrational spectroscopy provides a green tool for multi-component analysis. *TRaC Trends in Analytical Chemistry* 2010; **29**: 578-591.
(120) Hu Y, Erxleben A, Ryder AG, McArdle P. Quantitative analysis of sulfathiazole polymorphs in ternary mixtures by attenuated total reflectance infrared, near-infrared and Raman spectroscopy. *Journal of pharmaceutical and biomedical analysis* 2010; **53**: 412-420.
(121) Chieng N, Rehder S, Saville D, Rades T, Aaltonen J. Quantitative solid-state analysis of three solid forms of ranitidine hydrochloride in ternary mixtures

using Raman spectroscopy and X-ray powder diffraction. *Journal of Pharmaceutical and Biomedical Analysis* 2009; **49**: 18-25.
(122) de Peinder P, Vredenbregt MJ, Visser T, de Kaste D. Detection of Lipitor® counterfeits: A comparison of NIR and Raman spectroscopy in combination with chemometrics. *Journal of pharmaceutical and biomedical analysis* 2008; **47**: 688-694.
(123) Chen ZP, Fevotte G, Caillet A, Littlejohn D, Morris J. Advanced calibration strategy for in situ quantitative monitoring of phase transition processes in suspensions using FT-Raman spectroscopy. *Analytical chemistry* 2008; **80**: 6658-6665.
(124) Hwang M-S, Cho S, Chung H, Woo Y-A. Nondestructive determination of the ambroxol content in tablets by Raman spectroscopy. *Journal of pharmaceutical and biomedical analysis* 2005; **38**: 210-215.
(125) Heinz A, Strachan CJ, Gordon KC, Rades T. Analysis of solid-state transformations of pharmaceutical compounds using vibrational spectroscopy. *Journal of Pharmacy and Pharmacology* 2009; **61**: 971-988.
(126) Chieng N, Rades T, Aaltonen J. An overview of recent studies on the analysis of pharmaceutical polymorphs. *Journal of pharmaceutical and biomedical analysis* 2011; **55**: 618-644.
(127) Hédoux A, Guinet Y, Descamps M. The contribution of Raman spectroscopy to the analysis of phase transformations in pharmaceutical compounds. *International journal of pharmaceutics* 2011; **417**: 17-31.
(128) Alkhalil A, Babu Nanubolu J, Burley JC. Analysis of phase transitions in molecular solids: quantitative assessment of phonon-mode vs intra-molecular spectral data. *RSC Advances* 2012; **2**: 209-216.
(129) Cimarosti Z, Castagnoli C, Rossetti M, et al. Development of Drug Substances as Mixture of Polymorphs: Studies to Control Form 3 in Casopitant Mesylate. *Organic Process Research & Development* 2011; **14**: 1337-1346.
(130) Li Y, Chow PS, Tan RB. Quantification of polymorphic impurity in an enantiotropic polymorph system using differential scanning calorimetry, X-ray powder diffraction and Raman spectroscopy. *International journal of pharmaceutics* 2011; **415**: 110- 118.
(131) Virtanen T, Maunu SL. Quantitation of a polymorphic mixture of an active pharmaceutical ingredient with solid state 13C CPMAS NMR spectroscopy. *International Journal of Pharmaceutics* 2010; **394**: 18-25.
(132) Agatonovic-Kustrin S, Wu V, Rades T, Saville D, Tucker IG. Powder diffractometric assay of two polymorphic forms of ranitidine hydrochloride. *International Journal of Pharmaceutics* 1999; **184**: 107-114.
(133) Bugay DE, Newman AW, Findlay WP. Quantitation of cefepime · 2HCl dihydrate in cefepime · 2HCl monohydrate by diffuse reflectance IR and powder X-ray diffraction techniques. *Journal of Pharmaceutical and Biomedical Analysis* 1996; **15**: 49-61.
(134) Campbell Roberts SN, Williams AC, Grimsey IM, Booth SW. Quantitative analysis of mannitol polymorphs. X-ray powder diffractometry - exploring preferred orientation effects. *Journal of Pharmaceutical & Biomedical Analysis* 2002; **28**: 1149-1159.
(135) Dong W, Gilmore C, Barr G, Dallman C, Feeder N, Terry S. A quick method for the quantitative analysis of mixtures.1.Powder X-ray diffraction. *Pharmaceutical Technology* 2008; **97**: 2260-2276.

(136) Nemet Z, Kis GC, Pokol G, Demeter A. Quantitative determination of famotidine polymorphs: X-ray powder diffractometric and Raman spectrometric study. *Journal of Pharmaceutical & Biomedical Analysis* 2009; **49**: 338-346.
(137) Suryanarayanan R. Determination of the Relative Amounts of Anhydrous Carbamazepine and Carbamazepine Dihydrate in a Mixture by Powder X-ray Diffractometry. *Pharmaceutical Research* 1989; **6**: 1017-1024.
(138) Tian F, Zhang F, Sandler N, et al. Influence of sample characteristics on quantification of carbamazepine hydrate formation by X-ray powder diffraction and Raman spectroscopy. *European Journal of Pharmaceutics and Biopharmaceutics* 2007; **66**: 466-474.
(139) Tiwari M, Chawla G, Bansal AK. Quantification of olanzapine polymorphs using powder X0-ray diffraction technique. *Journal of Pharmaceutical & Biomedical Analysis* 2007; **43**: 865-872.
(140) Li Y, Shan Cow P, Tan RBH. Quantification of polymorphic impurity in an enantiotropic polymorph system using differential scanning calorimetry, X-ray powder diffraction and Raman spectroscopy. *International Journal of Pharmaceutics* 2011.
(141) Pöllänen K, Häkkinen A, Huhtanen M, et al. DRIFT-IR for quantitative characterization of polymorphic composition of sulfathiazole. *Analytica Chimica Acta* 2005; **544**: 108-117.
(142) McGoverin CM, Ho LCH, Zeitler JA, Strachan CJ, Gordon KC, Rades T. Quantification of binary polymorphic mixtures of ranitidine hydrochloride using NIR spectroscopy. *Vibrational Spectroscopy* 2006; **41**: 225-231.
(143) Ziémons E, Bourichi H, Mantanus J, et al. Determination of binary polymorphic mixtures of fluconazole using near infrared spectroscopy and X-ray powder diffraction: A comparative study based on the pre-validation stage results. *Journal of Pharmaceutical and Biomedical Analysis* 2011; **55**, 1208-1212.
(144) Patel AD, Luner PE, Kemper MS. Quantitative analysis of polymorphs in binary and multi-component powder mixtures by near-infrared reflectance spectroscopy. *International Journal of Pharmaceutics* 2000; **206**: 63-74.
(145) Xie Y, Tao W, Morrison H, et al. Quantitative determination of solid-state forms of a pharmaceutical development compound in drug substance and tablets. *International Journal of Pharmaceutics* 2008; **362**: 29-36.
(146) Pratiwi D, Fawcett JP, Gordon KC, Rades T. Quantitative analysis of polymorphic mixtures of ranitidine hydrochloride by Raman spectroscopy and principal components analysis. *European Journal of Pharmaceutics and Biopharmaceutics* 2002; **54**: 337-341.
(147) De Spiegeleer B, Seghers D, Wieme R, et al. Determination of the relative amounts of three crystal forms of a benzimidazole drug in complex finished formulations by FT-Raman spectroscopy. *Journal of pharmaceutical and biomedical analysis* 2005; **39**: 275-280.
(148) Al-Zoubi N, Koundourellis JE, Malamataris S. FT-IR and Raman spectroscopic methods for identification and quantitation of orthorhombic and monoclinic paracetamol in powder mixes. *Journal of pharmaceutical and biomedical analysis* 2002; **29**: 459-467.
(149) Roberts SNC, Williams AC, Grimsey IM, Booth SW. Quantitative analysis of mannitol polymorphs. X-ray powder diffractometry - exploring preferred

orientation effects. *Journal of pharmaceutical and biomedical analysis* 2002; **28**: 1149-1159.
(150) Wang H, Mann CK, Vickers TJ. Effect of Powder Properties on the Intensity of Raman Scattering by Crystalline Solids. *Applied Spectrosopy* 2002; **56**: 1538-1544.
(151) Nemet Z, Demeter A, Pokol G. Quantifying low levels of polymorphic impurity in clopidogrel bisulphate by vibrational spectroscopy and chemometrics. *Journal of pharmaceutical and biomedical analysis* 2009; **49**: 32-41.
(152) Tian F, Zhang F, Sandler N, et al. Influence of sample characteristics on quantification of carbamazepine hydrate formation by X-ray powder diffraction and Raman spectroscopy. *European Journal of Pharmaceutical Sciences* 2007; **66**: 466-474.
(153) McGoverin C, Ho L, Zeitler J, Strachan C, Gordon K, Rades T. Quantification of binary polymorphic mixtures of ranitidine hydrochloride using NIR spectroscopy. *Vibrational Spectroscopy* 2006; **41**: 225-231.
(154) Sheikhzadeh M, Rohani S, Jutan A, Manifar T, Murthy K, Horne S. Solid-state characterization of buspirone hydrochloride polymorphs. *Pharmaceutical research* 2006; **23**: 1043-1050.
(155) Strachan CJ, Pratiwi D, Gordon KC, Rades T. Quantitative analysis of polymorphic mixtures of carbamazepine by Raman spectroscopy and principal components analysis. *Journal of Raman Spectroscopy* 2004; **35**: 347-352.
(156) Nemet Z, Kis GC, Pokol G, Demeter A. Quantitative determination of famotidine polymorphs: X-ray powder diffractometric and Raman spectrometric study. *Journal of pharmaceutical and biomedical analysis* 2009; **49**: 338-346.
(157) Ziemons E, Bourichi H, Mantanus J, et al. Determination of binary polymorphic mixtures of fluconazole using near infrared spectroscopy and X-ray powder diffraction: a comparative study based on the pre-validation stage results. *Journal of pharmaceutical and biomedical analysis* 2011; **55**: 1208-1212.
(158) Otsuka M, Kato F, Matsuda Y, Ozaki Y. Comparative determination of polymorphs of indomethacin in powders and tablets by chemometrical near-infrared spectroscopy and X-ray powder diffraction. *AAPS PharmSciTech* 2003; **4**: 58-64.
(159) Heinz A, Savolainen M, Rades T, Strachan CJ. Quantifying ternary mixtures of different solid-state forms of indomethacin by Raman and near-infrared spectroscopy. *European Journal of Pharmaceutical Sciences* 2007; **32**: 182-192.
(160) Roberts SNC, Williams AC, Grimsey IM, Booth SW. Quantitative analysis of mannitol polymorphs. FT-Raman spectroscopy. *Journal of pharmaceutical and biomedical analysis* 2002; **28**: 1135-1147.
(161) Kachrimanis K, Rontogianni M, Malamataris S. Simultaneous quantitative analysis of mebendazole polymorphs A-C in powder mixtures by DRIFTS spectroscopy and ANN modeling. *Journal of pharmaceutical and biomedical analysis* 2010; **51**: 512-520.
(162) Kachrimanis K, Braun DE, Griesser UJ. Quantitative analysis of paracetamol polymorphs in powder mixtures by FT-Raman spectroscopy and PLS

regression. *Journal of pharmaceutical and biomedical analysis* 2007; **43**: 407-412.
(163) Taylor LS, Langkilde FW. Evaluation of solid-state forms present in tablets by Raman spectroscopy. *Journal of pharmaceutical sciences* 2000; **89**: 1342-1353.
(164) Karabas I, Orkoula MG, Kontoyannis CG. Analysis and stability of polymorphs in tablets: The case of Risperidone. *Talanta* 2007; **71**: 1382-1386.
(165) Luner PE, Majuru S, Seyer JJ, Kemper MS. Quantifying crystalline form composition in binary powder mixtures using near-infrared reflectance spectroscopy. *Pharmaceutical Development and Technology* 2000; **5**: 231-246.
(166) Patel AD, Luner PE, Kemper MS. Low-level determination of polymorph composition in physical mixtures using near-infrared reflectance spectroscopy. *Journal of Pharmaceutical Science* 2001; **90**: 360-370.
(167) Šašić S, Whitlock M. Raman Mapping of Low-Content Active-Ingredient Pharmaceutical Formulations. Part II: Statistically Optimized Sampling for Detection of Less Than 1% of an Active Pharmaceutical Ingredient. *Applied spectroscopy* 2008; **62**: 916-921.
(168) Xie Y, Tao W, Morrison H, et al. Quantitative determination of solid-state forms of a pharmaceutical development compound in drug substance and tablets. *International journal of pharmaceutics* 2008; **362**: 29-36.
(169) Šašić S, Mehrens S. Raman chemical mapping of low-content active pharmaceutical ingredient formulations. III. Statistically optimized sampling and detection of polymorphic forms in tablets on stability. *Analytical chemistry* 2012; **84**: 1019-1025.
(170) Vergote GJ, Vervaet C, Remon JP, Haemers T, Verpoort F. Near-infrared FT-Raman spectroscopy as a rapid analytical tool for the determination of diltiazem hydrochloride in tablets. *European Journal of Pharmaceutical Sciences* 2002; **16**: 63-67.
(171) Mazurek S, Szostak R. Quantitative determination of captopril and prednisolone in tablets by FT-Raman spectroscopy. *Journal of pharmaceutical and biomedical analysis* 2006; **40**: 1225-1230.
(172) Mazurek S, Szostak R. Quantification of atorvastatin calcium in tablets by FT-Raman spectroscopy. *Journal of pharmaceutical and biomedical analysis* 2009; **49**: 168-172.
(173) Li W, Bagnol L, Berman M, Chiarella RA, Gerber M. Applications of NIR in early stage formulation development. Part II. Content uniformity evaluation of low dose tablets by principal component analysis. *International journal of pharmaceutics* 2009; **380**: 49-54.
(174) Blanco M, Peguero A. Analysis of pharmaceuticals by NIR spectroscopy without a reference method. *TrAC Trends in Analytical Chemistry* 2010; **29**: 1127-1136.
(175) Blanco M, Cueva-Mestanza R, Peguero A. NIR analysis of pharmaceutical samples without reference data: Improving the calibration. *Talanta* 2011; **85**: 2218-2225.
(176) Ito M, Suzuki T, Yada S, et al. Development of a method for the determination of caffeine anhydrate in various designed intact tablets by near-infrared spectroscopy: a comparison between reflectance and transmittance technique. *Journal of pharmaceutical and biomedical analysis* 2008; **47**: 819-827.

(177) Xiang D, Konigsberger M, Wabuyele B, Hornung K, Cheney J. Development of robust quantitative methods by near-infrared spectroscopy for rapid pharmaceutical determination of content uniformity in complex tablet matrix. *Analyst* 2009; **134**: 1405-1415.
(178) Ito M, Suzuki T, Yada S, et al. Development of a method for nondestructive NIR transmittance spectroscopic analysis of acetaminophen and caffeine anhydrate in intact bilayer tablets. *Journal of pharmaceutical and biomedical analysis* 2010; **53**: 396-402.
(179) Šašić S. Raman mapping of low-content API pharmaceutical formulations. I. Mapping of alprazolam in Alprazolam/Xanax tablets. *Pharmaceutical research* 2007; **24**: 58-65.
(180) Hargreaves MD, Macleod NA, Smith MR, Andrews D, Hammond SV, Matousek P. Characterisation of transmission Raman spectroscopy for rapid quantitative analysis of intact multi-component pharmaceutical capsules. *Journal of pharmaceutical and biomedical analysis* 2011; **54**: 463-468.
(181) Fransson M, Johansson J, Sparén A, Svensson O. Comparison of multivariate methods for quantitative determination with transmission Raman spectroscopy in pharmaceutical formulations: John Wiley & Sons, Ltd., 2010: 674-680.
(182) Eliasson C, Macleod NA, Jayes LC, et al. Non-invasive quantitative assessment of the content of pharmaceutical capsules using transmission Raman spectroscopy. *Journal of pharmaceutical and biomedical analysis* 2008; **47**: 221-229.
(183) Pelletier MJ, Larkin P, Santangelo M. Transmission Fourier transform Raman spectroscopy of pharmaceutical tablet cores. *Applied Spectrosopy* 2012; **66**: 451-457.
(184) Szostak R, Mazurek S. FT-Raman quantitative determination of ambroxol in tablets. *Journal of Molecular Structure* 2004; **704**: 229-233.
(185) Mazurek S, Szostak R. Quantitative determination of diclofenac sodium and aminophylline in injection solutions by FT-Raman spectroscopy. *Journal of pharmaceutical and biomedical analysis* 2006; **40**: 1235-1242.
(186) Skorda D, Kontoyannis CG. Identification and quantitative determination of atorvastatin calcium polymorph in tablets using FT-Raman spectroscopy. *Talanta* 2008; **74**: 1066-1070.
(187) Chalus P, Roggo Y, Walter S, Ulmschneider M. Near-infrared determination of active substance content in intact low-dosage tablets. *Talanta* 2005; **66**: 1294-1302.
(188) Mazurek S, Szostak R. Quantitative determination of diclofenac sodium in solid dosage forms by FT-Raman spectroscopy. *Journal of pharmaceutical and biomedical analysis* 2008; **48**: 814-821.
(189) Orkoula MG, Kontoyannis CG, Markopoulou CK, Koundourellis JE. Quantitative analysis of liquid formulations using FT-Raman spectroscopy and HPLC: The case of diphenhydramine hydrochloride in Benadryl®. *Journal of pharmaceutical and biomedical analysis* 2006; **41**: 1406-1411.
(190) Alcalà M, León J, Ropero J, Blanco M, Romañach RJ. Analysis of low content drug tablets by transmission near infrared spectroscopy: Selection of calibration ranges according to multivariate detection and quantitation limits of PLS models. *Journal of pharmaceutical sciences* 2008; **97**: 5318-5327.
(191) Porfire A, Rus L, Vonica AL, Tomuta I. High-throughput NIR-chemometric methods for determination of drug content and pharmaceutical properties of

indapamide powder blends for tabletting. *Journal of pharmaceutical and biomedical analysis* 2012; **70**: 301-309.
(192) Ferreira MH, Braga JWB, Sena MM. Development and validation of a chemometric method for direct determination of hydrochlorothiazide in pharmaceutical samples by diffuse reflectance near infrared spectroscopy. *Microchemical Journal* 2012; **109**: 158-164.
(193) Blanco M, Peguero A. A new and simple PLS calibration method for NIR spectroscopy. API determination in intact solid formulations. *Analytical Methods* 2012; **4**: 1507-1512.
(194) Li Y, Fan Q, Liu S, Wang L. Simultaneous analysis of moisture, active component and cake structure of lyophilized powder for injection with diffuse reflectance FT-NIR chemometrics. *Journal of pharmaceutical and biomedical analysis* 2011; **55**: 216-219.
(195) Rosa SS, Barata PA, Martins JM, Menezes JC. Development and validation of a method for active drug identification and content determination of ranitidine in pharmaceutical products using near-infrared reflectance spectroscopy: a parametric release approach. *Talanta* 2008; **75**: 725-733.
(196) Orkoula MG, Kontoyannis CG. Non-destructive quantitative analysis of risperidone in film-coated tablets. *Journal of pharmaceutical and biomedical analysis* 2008; **47**: 631-635.
(197) Lopez-Sanchez M, Ruedas-Rama MJ, Ruiz-Medina A, Molina-Diaz A, Ayora-Canada MJ. Pharmaceutical powders analysis using FT-Raman spectrometry: simultaneous determination of sulfathiazole and sulfanilamide. *Talanta* 2008; **74**: 1603-1607.
(198) Mazurek S, Szostak R. Quantitative analysis of thiamine hydrochloride in tablets—Comparison of infrared attenuated total reflection, diffuse reflectance infrared and Raman spectroscopy. *Vibrational Spectroscopy* 2012; **62**: 10-16.
(199) Boiret M, Meunier L, Ginot YM. Tablet potency of Tianeptine in coated tablets by near infrared spectroscopy: Model optimisation, calibration transfer and confidence intervals. *Journal of pharmaceutical and biomedical analysis* 2011; **54**: 510-516.
(200) Sulub Y, LoBrutto R, Vivilecchia R, Wabuyele B. Near-infrared multivariate calibration updating using placebo: A content uniformity determination of pharmaceutical tablets. *Vibrational Spectroscopy* 2008; **46**: 128-134.
(201) Mantanus J, Ziémons E, Lebrun P, et al. Active content determination of non-coated pharmaceutical pellets by near infrared spectroscopy: Method development, validation and reliability evaluation. *Talanta* 2010; **80**: 1750-1757.
(202) Roggo Y, Degardin K, Margot P. Identification of pharmaceutical tablets by Raman spectroscopy and chemometrics. *Talanta* 2010; **81**: 988-995.
(203) Wold S, Sjöström M. Chemometrics, present and future success. *Chemometrics and Intelligent Laboratory Systems* 1998; **44**: 3-14.
(204) FDA. Guidance for industry PAT – A framework for innovative pharmaceutical manufacturing and quality assurance.: Guidance for industry PAT – A framework for innovative pharmaceutical manufacturing and quality assurance., 2004.
(205) Kourti T. Process Analytical Technology Beyond Real-Time Analyzers: The Role of Multivariate Analysis. *Critical Reviews in Analytical Chemistry* 2006; **36**: 257-278.

(206) Yu L. Pharmaceutical Quality by Design: Product and Process Development, Understanding, and Control. *Pharmaceutical research* 2008; **25**: 781-791.
(207) Barrett M, Hao H, Maher A, Hodnett K, Glennon B, Croker D. In Situ Monitoring of Supersaturation and Polymorphic Form of Piracetam during Batch Cooling Crystallization. *Organic Process Research & Development* 2011; **15**: 681-687.
(208) Pelletier MJ. Quantitaive Analysis using Raman Spectrometry. *Applied Spectrosopy* 2003; **57**: 20A-42A.
(209) Geladi P, McDougall D, Martens H. Linearization and Scatter-Correction for Near-Infrared Reflectance Spectra of Meat. *Applied spectroscopy* 1985; **39**: 491.
(210) Thennadil SN, Martin EB. Empirical preprocessing methods and their impact on NIR calibrations: a simulation study. *Journal of Chemometrics* 2005; **19**: 77-89.
(211) Gemperline P. *Practical Guide to Chemometrics*, Second edn.: Taylor and Francis, 2006.
(212) Savitzky A, Golay MJE. Smoothing and Differentiation of Data by Simplified Least Squares Procedures. *Analytical chemistry* 1964; **36**: 1627-1639.
(213) Mark H, Workman J, Jr. Derivatives in spectroscopy. Part I- the behavior of the derivative. *Spectroscopy* 2003; **18**: 32-37.
(214) Mark H, Workman J, Jr. Derivatives in spectroscopy. Part II- the true derivative. *Spectroscopy* 2003; **18**: 25-28.
(215) Mark H, Workman J, Jr. Derivatives in spectroscopy. Part III - computing the derivative. *Spectroscopy* 2003; **18**: 106-111.
(216) Martens H, Naes T. *Multivariate Calibration*, 2nd Edition edn. New Yord: Wiley, 1991.
(217) Wold S, Esbensen KH, Geladi P. *Chemometrics and Intelligent Laboratory Systems* 1987; **2**: 37.
(218) Assi S, Watt RA, Moffat AC. Identification of counterfeit medicines from the Internet and the World market using near-infrared spectroscopy. *Analytical Methods* 2011; **3**: 2231-2236.
(219) Yoon WL, Jee RD, Charvill A, Lee G, Moffat AC. Application of near-infrared spectroscopy to the determination of the sites of manufacture of proprietary products. *Journal of pharmaceutical and biomedical analysis* 2004; **34**: 933-944.
(220) Hu Y, Erxleben A, Hodnett BK, et al. Solid-state Transformations of Sulfathiazole Polymorphs: The Effects of Millling and Humidity. *Journal of Crystal Growth and Design* 2013; **13**: 3404-3413.
(221) Wold S, Martens H, Wold H. *The multivariate calibration problem in chemistry solved by the PLS method.* Heidelberg: Springer Verlag,, 1983.
(222) Wold S, Sjöström M, Eriksson L. PLS-regression: a basic tool of chemometrics. *Chemometrics and Intelligent Laboratory Systems* 2001; **58**: 109-130.
(223) ICH. Guidance for Industry Q2B Validation of Analytical Procedures: Methodology. http://www.fda.gov/downloads/Drugs/GuidanceComplianceRegulatoryInformation/Guidances/UCM073384.pdf, 1996.

(224) Blanco M, González Bañó R, Bertran E. Monitoring powder blending in pharmaceutical processes by use of near infrared spectroscopy. *Talanta* 2002; **56**: 203-212.
(225) Pavlova A, Konstantinova K, Daskalov H, Georgiev A. A study of crystalline forms of piracetam. *Pharmazie* 1983; **38**: 634.
(226) Ceolin R, Agafonov V, Louer D, Dzyabchenko VA, Toscani S, Cense JM. Phenomenology of polymorphism. III. The p,T diagram and stability of piracetam polymorphs. *Journal of Solid State Chemistry* 1996; **122**: 186-194.
(227) Savitzky A, Golay M. Smoothing and Differentiation of Data by Simplified Leas Squares Procedures. *Analytical chemistry* 1964; **36**.
(228) Barnes RJ, Dhanoa MS, Lister SJ. Standard Normal Variate Transformation and De-trending of Near-Infrared Diffuse Reflectance Spectra. *Applied spectroscopy* 1989; **43**: 772-777.
(229) Naes T, Isaksson T, Fearn T, Davies T. *A User-Friendly Guide to Multivariate Calibration and Classification* Chichester: NIR Publications, 2002.
(230) Socrates G. *Infrared and Raman characteristic frequencies: tables and charts*, Third edn.: Wiley, 2004.
(231) Littleford RE, Matousek P, Towrie M, et al. Raman spectroscopy of street samples of cocaine obtained using Kerr gated fluorescence rejection. *Analyst* 2004; **129**: 505-506.
(232) Shreve AP, Cherepy NJ, Mathies RA. Effective Rejection of Fluorescence Interference in Raman-Spectroscopy Using a Shifted Excitation Difference Technique. *Applied spectroscopy* 1992; **46**: 707-711.
(233) Schulmerich MV, Finney WF, Fredricks RA, Morris MD. Subsurface Raman spectroscopy and mapping using a globally illuminated non-confocal fiber-optic array probe in the presence of Raman photon migration. *Applied spectroscopy* 2006; **60**: 109-114.
(234) Winblad B. Piracetam: a review of pharmacological properties and clinical uses. *CNS Drug Reviews* 2005; **11**: 169-182.
(235) Pavlova AW. Polymorphic Forms of Piracetam. *Pharmazie* 1979; **34**: 449-450.
(236) Croker DM, Hennigan MC, Maher A, Hu Y, Ryder AG, Hodnett BK. A comparative study of the use of powder X-ray diffraction, Raman and NIR spectroscopy for quantification of binary polymorphic mixtures of Piracetam. *Journal of pharmaceutical and biomedical analysis* 2012; **63**: 80-86.
(237) de Veij M, Vandenabeele P, De Beer T, Remon JP, Moens L. Reference database of Raman spectra of pharmaceutical excipients. *Journal of Raman Spectroscopy* 2009; **40**: 297-307.
(238) Johansson J, Sparén A, Svensson O, Folestad S, Claybourn M. Quantitative Transmission Raman Spectroscopy of Pharmaceutical Tablets and Capsules. *Appl Spectrosc* 2007; **61**: 1211-1218.
(239) Gualtieri F, Manetti D, Romanelli MN, Ghelardini C. Design and study of Piracetam-like Nootropics, controversial members of the problematic class of cognition-enhancing drugs. *Current Pharmaceutical Design* 2002; **8**: 125-138.
(240) Winbald B. Piracetam: a review of pharmacological properties and clinical uses. *CNS Drug Reviews* 2005; **11**: 169-182.
(241) Kuhnert-Brandstaetter M, Burger A, Voellenklee R. Stability behavior of piracetam polymorphs. *Scientifica Pharmaceutica* 1994; **62**: 307-316.

(242) Admiraal G, Eikelenboom JC, Vos A. Structures of the triclinic and monoclinic modifications of (2-oxo-1-pyrrolidinyl)acetamide. *Acta Crystallographica Section B* 1982; **38**: 2600-2605.
(243) Vishweshwar P, McMahon JA, Peterson ML, Hickey MB, Shattock TR, Zaworotko MJ. Crystal engineering of pharmaceutical co-crystals from polymorphic active pharmaceutical ingredients. *Chemical Communications* 2005: 4601-4603.
(244) Viertelhaus M, Hilfiker R, Blatter F, Neuburger M. Piracetam Co-Crystals with OH-Group Functionalized Carboxylic Acids. *Crystal Growth and Design* 2009; **9**: 2220-2228.
(245) Dematos LL, Williams AC, Booth SW, Petts CR, Taylor DJ, Blagden N. Solvent influences on metastable polymorph lifetimes: real-time interconversions using energy dispersive X-ray diffractometry. *Journal of pharmaceutical sciences* 2007; **96**: 1069-1078.
(246) Khamchukov YD, Shashkov SN, Lukomskii EV. Vibrational Spectra of 2-Oxo-Pyrrolidineacetamide. *Journal of Applied Spectroscopy* 1990; **53**: 1281-1286.
(247) Byrn SR, Pfeiffer RR, Stephenson G, Grant DJW, Gleason WB. Solid-State Pharmaceutical Chemistry. *Chemistry of Materials* 1994; **6**: 1148-1158.
(248) Haleblian J, McCrone W. Pharmaceutical applications of polymorphism. *Journal of Pharmaceutical Science* 1969; **58**: 911-929.
(249) Byrne HJ, Sockalingum GD, Stone N. Chapter 4 Raman Microscopy: Complement or Competitor?, *Biomedical Applications of Synchrotron Infrared Microspectroscopy*: The Royal Society of Chemistry, 2011: 105-143.
(250) Johansson J, Sparen A, Svensson O, Folestad S, Claybourn M. Quantitative transmission Raman spectroscopy of pharmaceutical tablets and capsules. *Applied spectroscopy* 2007; **61**: 1211-1218.
(251) Chen Z-P, Fevotte G, Caillet A, Littlejohn D, Morris J. Advanced Calibration Strategy for in Situ Quantitative Monitoring of Phase Transition Processes in Suspensions Using FT-Raman Spectroscopy. *Analytical chemistry* 2008; **80**: 6658-6665.
(252) Pavlova A, Konstantinova K, Daskalov H, Georgiev A. A study of crystalline forms of piracetam. *Pharmazie* 1983; **38**: 634-635.
(253) Ceolin R, Agafonov V, Louer D, Dzyabchenko VA, Toscani S, Cense JM. Phenomenology of polymorphism. III. The p,T diagram and stability of piracetam polymorphs. *Journal of Solid State Chemistry* 1996; **122**: 186-194.
(254) Maher A, Croker D, Rasmuson AC, Hodnett BK. Solubility of Form III Piracetam in a Range of Solvents. *Journal of Chemical and Engineering Data* 2010; **55**: 5314-5318.
(255) Pavlova AV. Kinetics of polymorphic transformation of piracetam crystal forms. *Pharmazie* 1984; **39**: 272-273.
(256) Weltscheva PA. Polymorphic forms of piracetam. *Pharmazie* 1979; **34**: 449-450.
(257) Kuhnert-Brandstaetter M, Burger A, Voellenklee R. Stability behavior of piracetam polymorphs. *Scientifica Pharmaceutica* 1994; **62**: 307-316.
(258) Bonnier F, Mehmood A, Knief P, et al. In vitro analysis of immersed human tissues by Raman microspectroscopy. *Journal of Raman Spectroscopy* 2011; **42**: 888-896.
(259) Saeed M, Probst L, Betz G. Assessment of Diffuse Transmission and Reflection Modes in Near-Infrared Quantification, Part 2: Diffuse Reflection

Information Depth. *Journal of pharmaceutical sciences* 2011; **100**: 1130-1141.

(260) Everall N, Priestnall I, Dallin P, et al. Measurement of Spatial Resolution and Sensitivity in Transmission and Backscattering Raman Spectroscopy of Opaque Samples: Impact on Pharmaceutical Quality Control and Raman Tomography. *Applied Spectrosopy* 2010; **64**: 476-484.

11 Publications and Presentations

Publications

Please find published manuscripts appended to back of thesis.

Quantitative polymorph contaminant analysis in tablets using Raman and near infra-red spectroscopies, M.C. Hennigan and A.G. Ryder, Journal of Pharmaceutical and Biomedical Analysis, 2013, 72, 163–171.

A comparative study of the use of powder X-ray diffraction, Raman and NIR spectroscopy for quantification of binary polymorphic mixtures of piracetam, D.M. Croker, M.C. Hennigan, A. Maher, Y. Hu, A.G. Ryder and B.K. Hodnett, Journal of Pharmaceutical and Biomedical Analysis, 2012, 63, 80–86.

Presentations

Hennigan, M.C. "Comparison of near infra-red, transmission and backscattering Raman spectroscopies for the analysis of polymorphs." Invited speaker, Advances in Raman spectroscopy in pharmaceutical analysis, JPAG symposium, Royal Society of Chemisty, Burlington House, London, May 2012.

Hennigan, M.C., Ryder, A.G. "Polymorph contaminant analysis in tablets using Raman and near infra-red spectroscopies." Conference proceeding SSPC Strand Meeting, Trinity College Dublin, 2012.

Hennigan, M.C., Ryder, A.G. "Raman and near infra-red spectroscopic analysis of a model pharmaceutical tablet system containing low levels of polymorphic contaminant." Conference proceeding FACSS, Reno, USA, 2011.

Hennigan, M.C., Ryder, A.G. "Raman and near infra-red spectroscopic analysis of a model pharmaceutical tablet system containing low levels of polymorphic contaminant." Poster presentation SAS poster session, FACSS, Reno, USA, 2011.

Hennigan, M.C., Ryder, A.G. “Spectroscopic analysis of a model pharmaceutical tablet system containing low levels of a polymorphic contaminant.” Poster presentation Analytical Research Forum, University of Manchester, UK, 2011.

Hennigan, M.C., Ryder, A.G. “Determining the efficacy of rapid spectroscopic techniques for in–situ characterisation of polymorph contamination.” Conference proceeding SSPC Strand Meeting, University of Limerick, 2011.

Hennigan, M.C., Ryder, A.G. “Determining the efficacy of rapid spectroscopic techniques for in–situ characterisation of polymorph contamination.” Conference proceeding SSPC Technical Meeting, NUI Galway, 2010.

Hennigan, M.C., Ryder, A.G. “Determining the efficacy of rapid spectroscopic techniques for in–situ characterisation of polymorph contamination.” Conference proceeding FACSS, Raleigh, USA, 2010.